Shipboard Applications of Non-Intrusive Load Monitoring

by

Jack S. Ramsey Jr.

B.A. Physics
Florida State University, 1993

Submitted to the Department of Ocean Engineering and the Department of Electrical Engineering and Computer Science in Partial Fulfillment of the Requirements for the Degrees of

Naval Engineer

and

Master of Science in Electrical Engineering and Computer Science

at the
Massachusetts Institute of Technology
June 2004

Signature of Author .....
Department of Ocean Engineering
May 7, 2004

Certified by .....
Steven B. Leeb
Associate Professor of Electrical Engineering and Computer Science
Thesis Supervisor

Certified by .....
Timothy J. McCoy
Associate Professor of Naval Construction and Engineering
Thesis Reader

Accepted by .....
Arthur C. Smith
Chairman, Committe on Graduate Students
Department of Electrical Engineering and Computer Science

Accepted by .....
Michael S. Triantafyllou
Chairman, Committe on Graduate Students
Department of Ocean Engineering

Shipboard Applications of Non-Intrusive Load Monitoring

by

Jack S. Ramsey Jr.

B.A. Physics
Florida State University, 1993

Submitted to the Department of Ocean Engineering and the Department of Electrical Engineering and Computer Science in Partial Fulfillment of the Requirements for the Degrees of

Naval Engineer

and

Master of Science in Electrical Engineering and Computer Science

at the
Massachusetts Institute of Technology
June 2004

Signature of Author .....
Department of Ocean Engineering
May 7, 2004

Certified by .....
Steven B. Leeb
Associate Professor of Electrical Engineering and Computer Science
Thesis Supervisor

Certified by .....
Timothy J. McCoy
Associate Professor of Naval Construction and Engineering
Thesis Reader

Accepted by .....
Michael S. Triantafyllou
Chairman, Committe on Graduate Students
Department of Ocean Engineering

Accepted by .....
Arthur C. Smith
Chairman, Committe on Graduate Students
Department of Electrical Engineering and Computer Science

THIS PAGE INTENTIONALLY BLANK

Shipboard Applications of Non-Intrusive Load Monitoring

by

Jack S. Ramsey Jr.

Submitted to the Department of Ocean Engineering and
the Department of Electrical Engineering and Computer Science
on May 7, 2004 in Partial Fulfillment of
the Requirements for the Degrees of Naval Engineer and
Master of Science in Electrical
Engineering and Computer Science

ABSTRACT

The Non-Intrusive Load Monitor (NILM) provides a method of measuring component performance and source power quality through a single point of entry in the power distribution system. A study was performed utilizing the NILM onboard three different ships (along with experimentation in the laboratory) to determine its effectiveness in determining the state of mechanical systems through analysis of electrical power data.

Data collected from the Auxiliary Seawater System onboard the USCGC SENECA indicate that the NILM is able to predict several faults (clogged pump inlet strainers, faulty motor/pump coupling, fouled heat exchangers) as well as provide a backup indication of flow levels to heat loads. Data collected from the Sewage System of the SENECA indicate several metrics which can be applied to cycling systems in general to differentiate between periods of heavy usage and fault conditions. Finally, data collected from the Steering System of the SENECA as well as a yard patrol boat operated by the Office of Naval Research shows the potential of the NILM to be used as a control system without the need for separate mechanical transducers.

Thesis Supervisor: Steven B. Leeb
Title: Associate Professor of Electrical Engineering and Computer Science

THIS PAGE INTENTIONALLY BLANK

Acknowledgments

The author would like to acknowledge the following organizations and individuals for their assistance. Without them this thesis would not have been possible.

- The Office of Naval Research's Electric Ship Integration Initiative and Control Challenge, The Grainger Foundation, Tektronix, and Hewlett Packard, all of whom provided funding.
- Joe Mearman and Brian Lounsberry of Anteon for their support with the ONR YP.
- "Dutch" and "Moose" of Woods Hole for their support with the *Oceanus*.
- LT Mike Obar, EM1 Henrichs, and MK1 Kiley for their support on the USCGC SENECA.
- CDR Tim McCoy for doing a great job as my reader.
- Finally, Professor Steve Leeb for reminding me what academia was all about.

THIS PAGE INTENTIONALLY BLANK

Contents

THIS PAGE INTENTIONALLY BLANK

List of Figures

List of Tables

THIS PAGE INTENTIONALLY BLANK

Chapter 1

Introduction

1.1 Motivation for Research

The U.S. Navy has a growing dependence on technology to perform its mission, making ships ever more complex. As a result of the number and complexity of shipboard systems, it becomes more important to monitor them constantly. The research presented in this thesis is the first step towards developing an automated electrical load monitoring system for shipboard use.

1.1.1 The Electric Ship

There is a growing trend of "electrification" in U.S. Navy ships, most notably in the development of the integrated power system. In the integrated power system, ships no longer have separate main engines to provide power for propulsion and generators to provide electricity. The ship that uses an integrated power system would have only generators which supply electrical power for ship service power, combat system power, and propulsion power (via an electric drive system). This setup allows the generators to be loaded closer to their rated power output in order to operate the prime mover for these generators at higher efficiency (and therefore lower specific fuel consumption).

Another way that the electrical loading on naval ships is increasing is through transition from mechanical systems to electrical systems. Advances in computing and power electronics have made possible electrical equipment applications which have traditionally been mechanical, hydraulic, or pneumatic. For example, steam catapults have traditionally been used to launch aircraft from aircraft carriers. The electromagnetic aircraft launch system (EMALS), which uses a linear induction motor, will replace the traditional steam catapults on the next generation of aircraft carrier.

The final way that the electrical loading on naval ships is increasing is through the increased computing power required on ships. This is due not only to the increasing abilities of the combat system suite, but also because of the more extensive use of information technology.

The importance of electrical monitoring grows as the number of electrical loads onboard warships increases. As the shipboard distribution systems get more complicated, it will be more difficult to keep track of the loading and usage of all electrical loads; hence the need for an electrical load monitoring system.

1.1.2 A Growing Need for Information

Along with the increased use of electrical equipment on ships, there is a trend to make ships more automated. This would not only allow for reduced manning (and therefore reduce operating cost) but would also make ship systems more reliable. Automation of equipment has two fundamental aspects, control and monitoring. Since it is impossible for an automated system to know what control signals to send unless it knows the current state of the system being controlled, monitoring the state of the system becomes a crucial part of automation.

In addition to monitoring systems as part of automation, there is also an increasing need to collect information for the purpose of condition-based maintenance. The preventive maintenance system traditionally used by the U.S. Navy follows the idea that equipment should be serviced at a regular (and conservative) interval in order to prevent failures from occurring. The drawback of this philosophy is that equipment which has a low level of usage can be serviced more often than is necessary while equipment which is heavily used may not be serviced before failure. As a cost-saving measure, there is a growing emphasis on condition-based maintenance in which equipment is serviced based on its actual condition. Of course, the condition of equipment can only be known if that equipment is continuously monitored.

1.2 Previous Shipboard Monitoring

It would be useful at this point to briefly review some of the past efforts in monitoring ship systems.

1.2.1 Mechanical Monitoring of Mechanical Equipment

This kind of monitoring is the simplest and has been going on for the longest period of time. With the transition from sail to steam, it became necessary to monitor the parameters of the steam plant. This monitoring continues on mechanical systems today, with a watchstander walking around looking at pressure and temperature indications and writing down the readings into a log once per hour. In some cases these indications are purely mechanical, such as a Pitot tube (as described in [1]) used to measure total pressure in a fluid system. In some cases the indication involves a transducer to convert from one form of energy to another, as in a thermocouple used to measure temperature. Whether a direct mechanical indication or a transducer, the information recorded is always mechanical in nature.

There has been a recent increase in automated log taking for mechanical systems in which a central processor collects information from transducers and automatically records it. An example of this is a system onboard the USCGC SENECA that records any changes in main engine rpm. Although this alleviates some of the burden on the watchstanders, it does not provide any analysis or control functions. Watchstanders are still required to analyze trends in data and take the appropriate actions.

1.2.2 Electrical Monitoring of Electrical Equipment

In addition to monitoring the electrical parameters of the generating equipment, many other parameters are now being monitored onboard ships as described below.

With the push towards electric drive systems, it has become necessary to develop control and monitoring systems for extremely large electric motors. The system presented in [2] uses "search

coils" to monitor the amount of flux in a large electric motor as an indicator of motor condition. Flux information is collected by the system and compared to baseline flux levels in an effort to detect faults in the motor's rotor. For example, the partial demagnetisation of a single magnet (from a total of 38 pole-piece pairs mounted on the rotor) can be detected as a change in the flux amplitude over a single rotation of the rotor.

The arc-fault detection system described in [3] is a way of detecting the existence of arc faults in electrical switchboards. As described by the paper, arc faults were becoming an increasing problem as the source for fires in submarine switchboards in the 1970's. The faults occur because of faulty connections due to corrosion, faulty fastenings, and vibration as well as contamination and foreign objects. The circuit breakers installed in switchboards do not open for an arc because the arcs often draw much less current than the currents already present in the switchboard. As a result, the arc fault detection system that was developed uses photo and pressure detectors to sense the presence of an arc. At the time that [3] was written, the system has accumulated 500 ship-years of operation without a single erroneous operation.

1.2.3 The ICAS system

Most of the information in this section is taken directly from [4]

The Integrated Condition Assessment System (ICAS) is a Commercial Off the Shelf (COTS) software product designed to provide a computerized engineering tool to eliminate paper logs, implement Condition Based Maintenance (CBM) via expert analysis and improve availability and reliability. The ICAS is a Microsoft Windows NT based system running on state-of-the-art ruggedized commercial workstations. It continuously assesses machinery performance conditions and transmits the information over a fiber optic network for shipboard or shore side expert review action and planning. Thus ICAS provides maintenance personnel with real-time data display at these consoles, continuous performance assessment and trends, alarms, equipment vibration information, continuous expert analysis and diagnostics. The ICAS shell is loaded with a hull specific Configuration Data Set (CDS) outlining the failure and maintenance modes of the main propulsion, electrical, auxiliary and combat systems equipment. These failure and maintenance modes are defined by Navy subject matter experts including ship's force, in-service engineering agents and fleet technical support personnel. Inputs to ICAS consist of both manually collected data and on-line sensors (including those parameters collected by MCS and shared over the common LAN).

Although ICAS seems very capable, it actually has several severe limitations. The biggest drawback is that ICAS is software for analyzing and trending data, not a data collection system. The Portable Data Terminal (PDT) and Portable Diagnostic Aid (PDA) are hand held units utilized to collect manual data and upload to the ICAS workstation where it can be analyzed, trended, and logged. The PDT is used to enter log sheet data into the ICAS system. Sensors are typically grouped to represent a paper log sheet. The operator punches data in on the PDT's alphanumeric keypad and then downloads the data into the ICAS system via the Data Transfer Cable. The PDA is used for acquiring and analyzing vibration data on rotating machinery. It is manufactured by Dynamic Instruments and has an OEM model # of DI-306. The unit is capable of acquiring both broadband and narrowband vibration signatures. The data is acquired via the PDA and downloaded into the ICAS system for analysis and trending. The only data which is automatically collected by ICAS is from the Machinery Control System (MCS). The data collected by ICAS from MCS is not related to the status of the equipment, it is only a record of control signals sent to the equipment.

1.3 Non-Intrusive Load Monitoring

Non-Intrusive Load Monitoring research has been in progress at the Massachusetts Institute of Technology's Laboratory for Electromagnetic and Electronic Systems (LEES) for the last twenty years. The Non-Intrusive Load Monitor (NILM) provides a method of measuring component performance and source power quality through a single point of entry in the power distribution system using only one voltage and one current transducer. The NILM can be used in single or three-phase systems over a wide range of both voltage and current. The NILM has the ability to measure multiple loads simultaneously by employing a Pentium based personal computer running a modified version of the Linux operating system. The NILM is relatively easy to build, install, and run (see Chapters 2 and 3 for more information).

It has been determined that since the NILM has a high data collection rate (8 kHz for voltage and current, 120 Hz for power envelopes), it can detect very short duration transients. It has also been determined through experimentation that if the electrical load in question is tied to a mechanical system (e.g. a pump, fan, etc.), then changes in the mechanical system can have quantifiable impacts on the electrical signature of that load. Best summarized in [5], the application of the NILM to date has been primarilay in HVAC systems.

1.4 Putting it all Together: The NILM on Ships

The following observations are made from the preceding sections:

- Monitoring of mechanical parameters onboard ship requires crewmembers to read unsophisticated instruments which are not accurate or prone to failure. In the case where mechanical parameters are monitored electronically, a dedicated transducer is required for each parameter. This transducer is subjected to the actual environment that it is monitoring.
- Monitoring of electrical parameters onboard ship has to date been conducted at the generation or distribution level with the purpose of protecting the electrical system from electrical faults.
- The ICAS system has the ability to analyze and trend equipment loading, but does not automatically collect data.

Clearly a better system is needed onboard U.S. Navy warships to monitor the electrical loads as called for in [6]. Such a system should have the following attributes:

- Fault Detection. Data collected would continuously be compared to a library of normal and abnormal conditions to report the existence of a fault condition to an operator. The operator "...must be presented with information in a manner which assists quick decision making and error-free command inputs." [7]
- Automatic Corrective Action. Should a fault condition be severe, the system would be able to shift over to a redundant piece of equipment before catastrophic failure of the faulted equipment occurred.
- Fault Correction. Should a catastrophic failure occur, data collected by the system would be stored in a robust format to be used later to determine the cause of the fault.

- Usage Trending. Tracking of equipment usage would be used to ensure equal run time for systems with redundant electrical loads.

The NILM would be a perfect starting point for such a system for many reasons:

- It can gather mechanical information about a system from electrical information without the need for dedicated mechanical transducers. The electrical sensors used are solid-state and are therefore very reliable.
- Since the sensors used are located inside an electrical panel or controller, they are not subjected to the harsh conditions present in most mechanical systems.
- Electrical monitoring is accomplished using existing power cabling so backfitting the system on older ships would not require running an excessive amount of cabling. It would also not require creating penetrations into mechanical systems.
- All NILM installations used to date are COTS and so are very cost effective.

1.5 Objectives and Outline of Thesis

The research in this thesis represents the first step in developing the monitoring system mentioned above. Since electrical load monitoring of this kind has never been attempted on a ship (to the author's knowledge), the scope was very large. The goal was to find as many ships as possible with complex electromechanical systems and install NILMs on those systems. The data would be analyzed to determine which systems the NILM was best suited to monitor. A total of 12 systems were monitored on 3 different ships with almost 200 gigabytes of data collected. As to be expected with research of this kind, some systems are more amenable to non-intrusive monitoring than others. Analysis of some data has been deferred to the future.

Chapters 2 and 3 discuss brief theory and construction of the NILM. Chapters 4, 5, and 6 discuss results for data taken onboard the USCGC SENECA for the sewage system, auxiliary seawater system, and steering system, respectively. Chapter 6 also discusses results for the steering system onboard a yard patrol craft operated by the Office of Naval Research. Chapter 7 presents an outline of future work that will be conducted in upcoming years.

THIS PAGE INTENTIONALLY BLANK

Chapter 2

Background

2.1 Measuring Real and Reactive Power

The NILM uses measurements of voltage and current to produce estimates of real and reactive power consumption (henceforth referred to as P and Q, respectively). For a single phase system, the NILM is supplied with the voltage from line to neutral and the current flowing to any loads downstream of the monitoring point. Real power (P) is produced by current which is in-phase with voltage and reactive power (Q) is produced by current which is 90 degrees out of phase with voltage. It also estimates the higher harmonic content of current to produce the first three odd harmonics of real and reactive power (referred to as P_k and Q_k for the k^{th} harmonic of P and Q, respectively).

If the same sinusoidal voltage is applied to a resistor, capacitor, and inductor, the NILM would produce positive P with zero Q for the resistor, Positive Q with zero P for the inductor, and negative Q with zero P for the capacitor in accordance with the convention proposed in [8]. The convention of using a power angle measured in the clockwise direction from the real axis is employed, so that the power angle for an inductor is +90 degrees while the power angle for a capacitor is -90 degrees. The summary of phase relationships between voltage and current for the three components is shown in Figure 2.1.

For a more in-depth description of the NILM calculations used to determine P and Q, see [9].

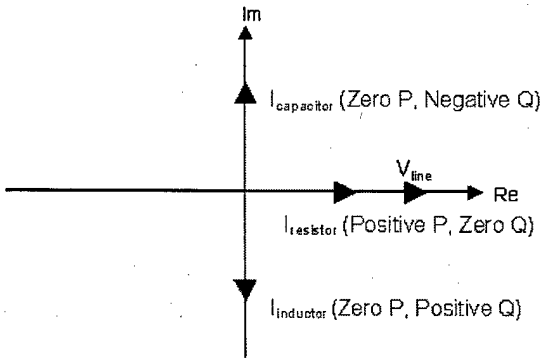

Figure 2.1: Voltage and Current Phase Relationships for 3 Components

2.2 Adaptation to a 3-Phase Ungrounded Power System

For a three-phase ungrounded power system, as one would find on a ship, things become more complex. Since there are three different AC voltages (each out of phase by $\pm$ 120 degrees with respect to the other two) and no neutral wire, the voltage supplied to the NILM must be line-to-line (between phases). Figure 2.2 represents a 3-phase generation scheme showing phase and line-to-line voltages [10].

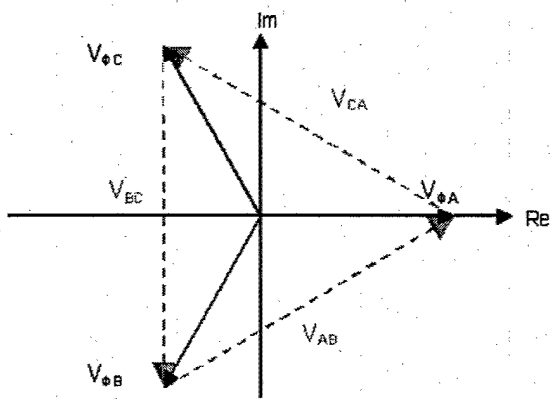

Figure 2.2: 3-Phase Voltage Generation Scheme

For a purely resistive load in a 3-phase power system, Figures 2.3 and 2.4 apply. The 3-phase voltage source is shown in a "wye" configuration, while the resistive load is shown in a"delta" configuration as is typical onboard a ship[1] [11]. In Figure 2.4, line-to-line voltages are shown (although differ from the previous figure in that they have been moved to the origin) along with line currents that would be flowing from the source [10]. Note that line currents are in phase with phase voltages (scaled by Ohm's Law).

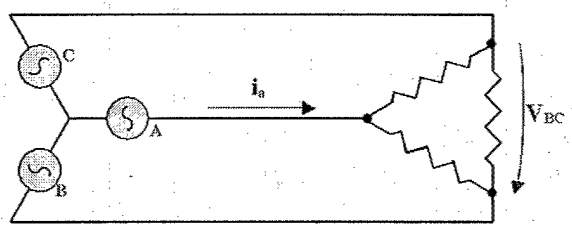

Figure 2.3: Wye-Delta Configuration of Resistive Load

It is noted from Figure 2.4, there are now three voltage-current pairs that show a 90 degree phase shift, (V_{BC}, I_A), (V_{CA}, I_B), and (V_{AB}, I_C). From the previous discussion of a single phase system, if any one of these voltage-current pairs was provided as input, the NILM would output

[1]The difference between wye and delta configurations is only in their voltage and current amplitudes, not their phase relationships for an ungrounded system.

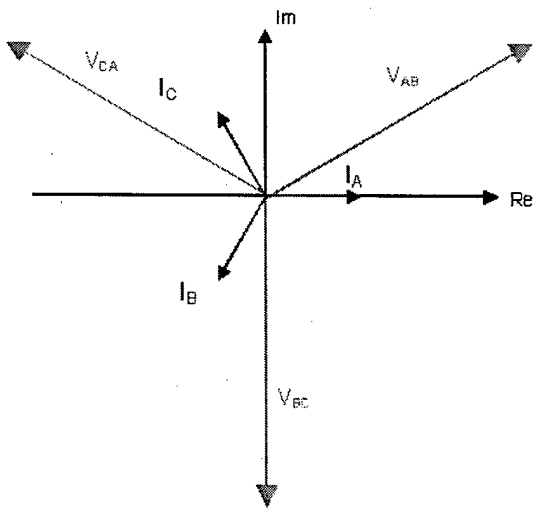

Figure 2.4: Wye-Delta Resistive Load Phasor Diagram

negative Q and zero P. Since the load in question is purely resistive, power *must* be positive P and zero Q. Fortunately, since the NILM outputs power data in table form, the only adjustment that needs to be made is one of interpretation. The column that represented P for the single-phase system now represents Q in the three-phase system and the column that represented Q in the single-phase system represents -P in the three-phase system. The relationship between line-to-line voltages and line currents is exploited by other commercially available products (such as the Fluke 39 powermeter which is used to calibrate the NILM power measurements [12]). The connection of the Fluke powermeter is shown in Figure 2.5.

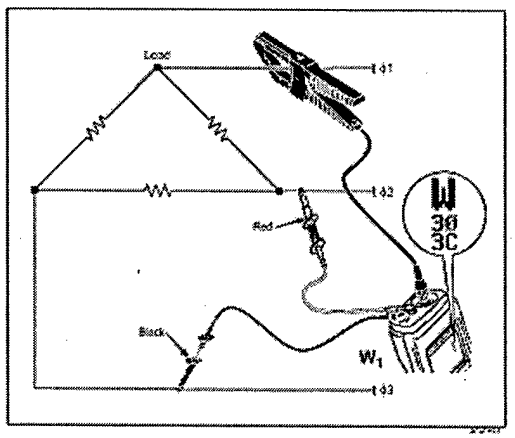

Figure 2.5: Fluke 39 Powermeter 3-Phase Power Measurement

There is a drawback to this method of three-phase data collection in that it applies only to a balanced system. Stating that power measurements taken from these orthogonal voltage-current pairs is proportional to the total power consumed by a load assumes that each phase is drawing

the same amount of power. In practice this is generally and approximately true, but if a load is unbalanced, important dynamic information could be lost due to a poor choice of the monitored voltage-current pair. The current hardware configuration of the NILM does not allow for summing of individual phase loading. An example of currents in a three-phase load onboard the research vessel *Oceanus* is shown in Figure 2.6. Note that the three phases of the motor are slightly out of balance as indicated by the oscillation of the current sum around zero.

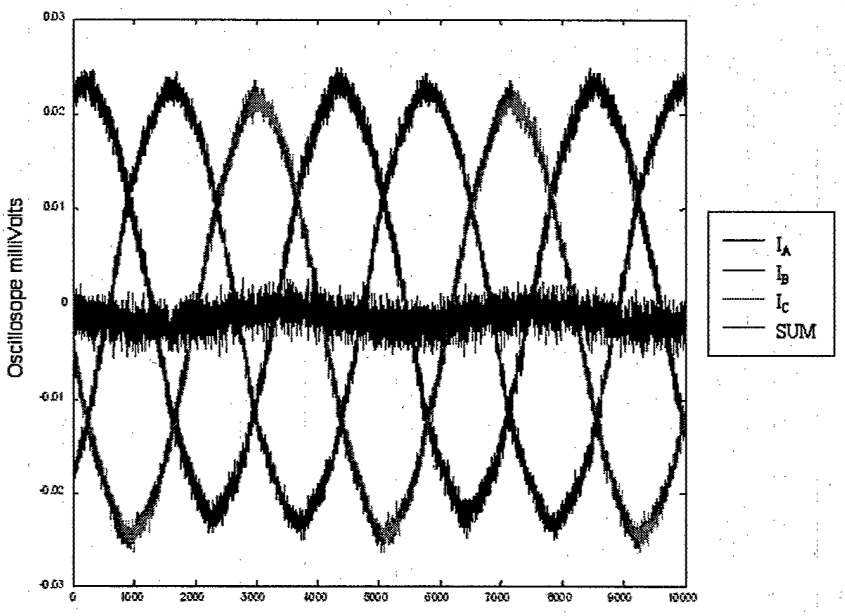

Figure 2.6: Example of 3-Phase Induction Motor Currents

Chapter 3

Hardware and Software for a Typical Installation

3.1 Introduction

A complete NILM setup is comprised of commercially available hardware that is relatively easy to acquire, assemble, and install. Commercially available hardware was chosen because of its wide availability and low cost. A setup consists of a NEMA-type enclosure to house the measuring transducers and their associated power supply, a personal computer (PC) with keyboard and monitor, and an uninterruptible power supply. A block diagram for a NILM setup is shown in Figure 3.1 while a photograph of a typical installation is shown in Figure 3.2

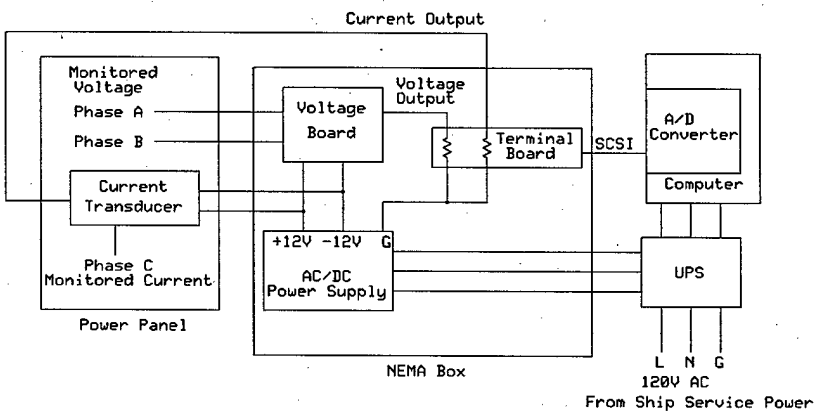

Figure 3.1: Block Diagram of Complete NILM Setup

The personal computer used in NILM setups runs the Linux operating system. Since the source code for Linux is freely available, custom software to be used in conjunction with the NILM can be easily developed at low cost. Linux is also a very reliable system, which is especially important if long periods of automatic data collection are anticipated.

Installation of a NILM setup can be accomplished using readily available hardware and tools. For the shipboard installations discussed in this thesis, the hardware was attached to panels, bulkheads, or mounting plates with nuts and bolts. Cables were strung in exising cableways.

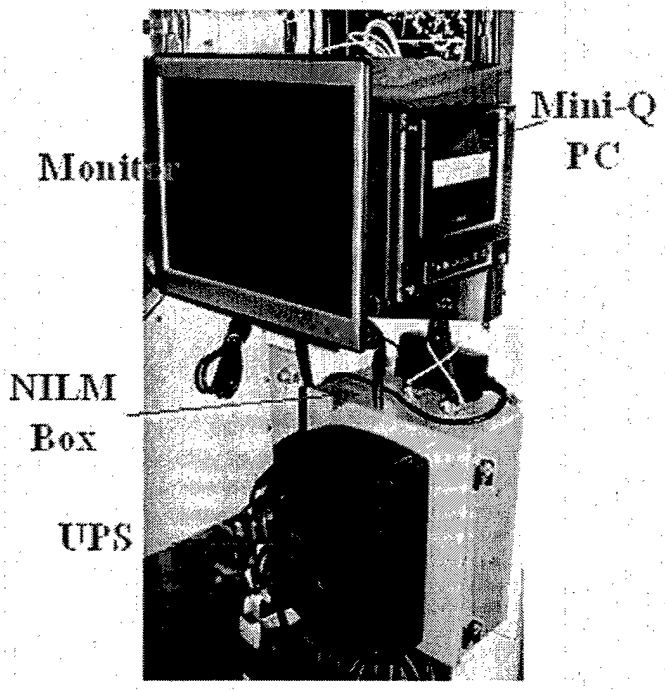

Figure 3.2: Typical NILM Setup

3.2 Measuring Hardware

Voltage and current inputs to the PC are generated by two transducers. Each of the transducers employs the Hall-effect to produce output current proportional to input voltage or current. In each case, the transducers are powered across two of their terminals by $\pm 12V$ in parallel with capacitors[1]. The specific transducers used for this research were the LEM LV 25-P to measure voltage and either the LEM LA 55-P, LA 205-S, or LA 305-S to measure current. Specifications for these transducers are listed in Appendix A.

In the case of the voltage transducer, pins are also provided for input voltage (line and neutral) and output current. The transducers are mounted on a board in series with resistors that are selected based on input voltage to prevent exceeding the transducer's maximum current rating of 10 mA. A schematic and photograph of the voltage board is shown in Figures 3.3 and 3.4. The voltage board was originally designed to measure three phases independently, but only one line-to-line voltage measurement was used for all shipboard installations.

The current transducer is placed directly in the panel of the load(s) being measured. An insulated three-wire cable is routed to the transducer to provide DC voltage and carry the output signal back to the NILM. A current transducer is shown in Figure 3.5 inside of a pump controller (voltage leads are also shown connected to the other two phases).

[1]To account for any "noise" in the power supplies

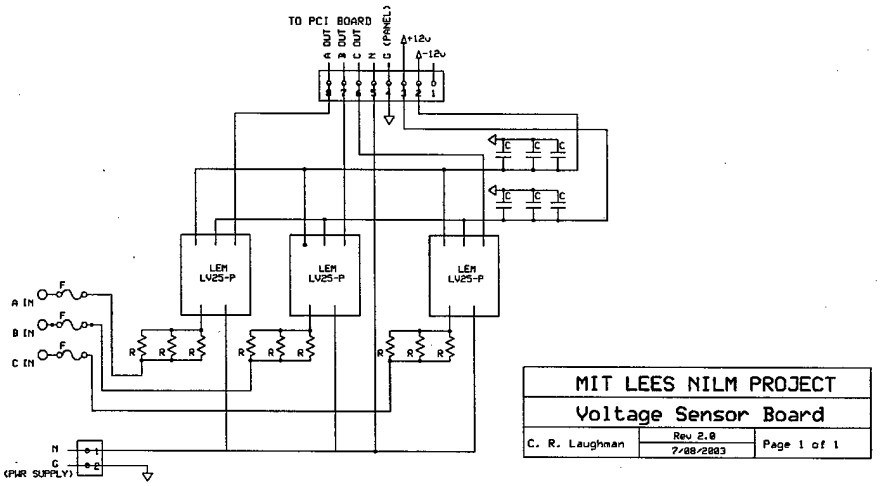

Figure 3.3: Voltage Sensing Schematic

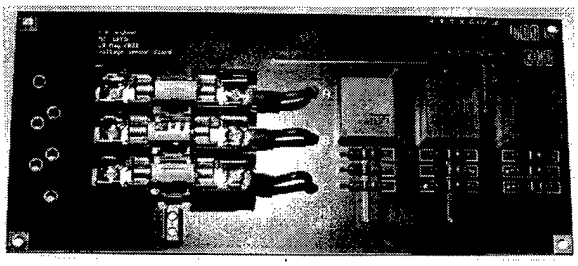

Figure 3.4: Assembled Voltage Sensing Board

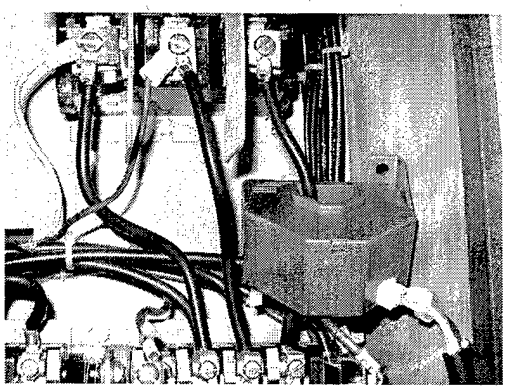

Figure 3.5: Installed Current Transducer

3.3 Setup/Installation

The setup of the NILM involves using the voltage board and current transducer together with a power supply and wiring terminal board inside a NEMA enclosure. The line and neutral portions

of a grounded 120V AC power cord are attached to the power supply while the ground is attached to the voltage board. The DC voltages output from the power supply are connected to the voltage board and a terminal strip to supply the current transducer. The power supply ground is connected to the wiring terminal board.

Outputs from the voltage board and current transducer are connected to the wiring terminal board. Voltage drops across the terminal board are produced by placing resistors across the terminals for the transducer outputs and the power supply ground. The resistors must be chosen carefully based on the output of the transducers to produce a voltage drop within the range required by the data collection card inside the computer. Reference resistors must also be placed between the power supply ground and pin 27 of the wiring terminal board. The PCI 1710 analog-to-digital data card used converts an analog signal in the range of -5 V to +5V to digital "counts" in the range of 0 to 4096 counts. Table 3.1 specifies the electrical connections required for a NILM setup.

Table 3.1: Electrical Connection Scheme Required for NILM Setup

Component	**Terminal**
Power Supply +12V	Voltage board +12V and junction strip terminal 1
Power Supply -12V	Voltage board -12V and junction strip terminal 3
Power Supply Ground	SCSI-II terminals 33, 34
Current Transducer +12V	Junction strip terminal 1
Current Transducer -12V	Junction strip terminal 3
Current Output	SCSI-II terminal 67
Voltage Output	SCSI-II terminal 68
Measurement Resistors	SCSI-II terminals 68 and 34 SCSI-II terminals 67 and 33
Reference Resistors	SCSI-II terminals 34 and 27 SCSI-II terminals 33 and 27

3.3.1 Resistor Selection

The following example illustrates proper selection of resistors and a current transducer for use with a load that draws 6.5 A in steady state with 450 V (rms line-to-line) applied:

1. The voltage board should contain three resistors in parallel at the input of the voltage transducer. A good rule of thumb for sizing each of the resistors in the voltage board is to use resistances approximately equal (in $k\Omega$) to the RMS voltage being measured. For example, to measure 450 V rms line-to-line voltages on ships, three 470 $k\Omega$ resistors were soldered into the voltage boards used. If the three parallel resistors used are each 470 $k\Omega$ (equivalent resistance = 156.67$k\Omega$), then the rms current through the transducer would be 2.87 mA (450V/156.67$k\Omega$).

2. The rms output current of 7.18 mA is determined from the conversion factor of 2500:1000 as specified in Appendix A.

3. To size the resistor across pins 34 and 68 of the wiring terminal board, the peak voltage across the resistor can not exceed 5 V. The peak current from the rms value is 10.15 mA ($\sqrt{2}I_{rms}$), so the largest resistance that could be used is 493Ω (5V/10.15mA). The maximum allowed measuring resistance allowed by the specification sheet however, is 190Ω, so that resistance is the largest that can be used.

4. For sizing the current transducer, a conservative estimate of peak current draw at startup is 10 times the steady state value of current. The LA 55-P should be used because of its ability to measure up to 70 A.

5. For sizing the resistor across pins 33 and 67 of the wiring terminal board, the same procedure as before is used with a current conversion factor of 1:1000. The 5 V maximum allowed across the resistor is divided by the peak output current of 70 mA to obtain a value of 71.4Ω. This is less than the maximum allowed measuring resistance specified in Appendix A.

The voltages across the wiring terminal board are provided to the data collection card in the computer via a SCSI cable. The interior view of a NEMA enclosure containing the voltage board, power supply, and wiring terminal board is shown in Figure 3.6

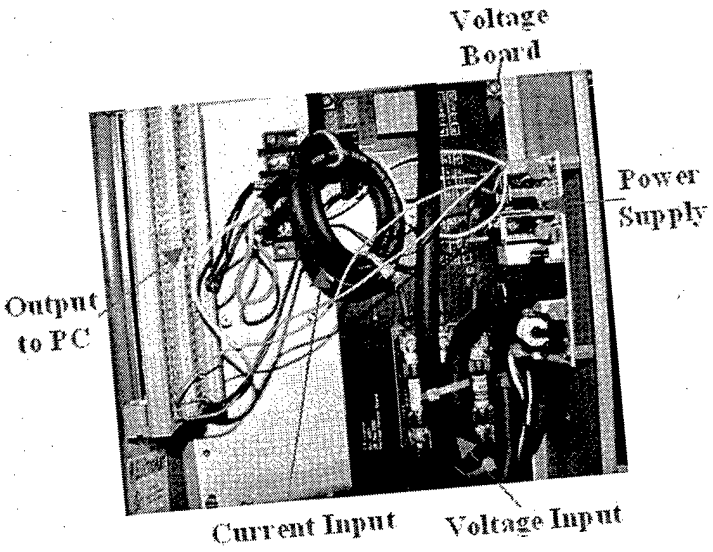

Figure 3.6: NEMA Box Containing NILM Hardware

3.4 Obtaining Data

Obtaining data is relatively simple using the NILM menu shown in Figure 3.7[2]. The menu allows the user to collect compressed power data into one-hour "snapshots" and later write the data to

[2]Italicized text indicates variable information while normal text indicates information which does not change.

a CD. The menu screen provides the current date and time along with the amount of data that has not yet been written to a CD and the number of CDs needed to do so. Should the amount of storage space on the hard drive run out, the application will begin erasing snapshots starting with the oldest to write newer data. Once snapshot data has been written to a CD, it is erased from the hard drive.

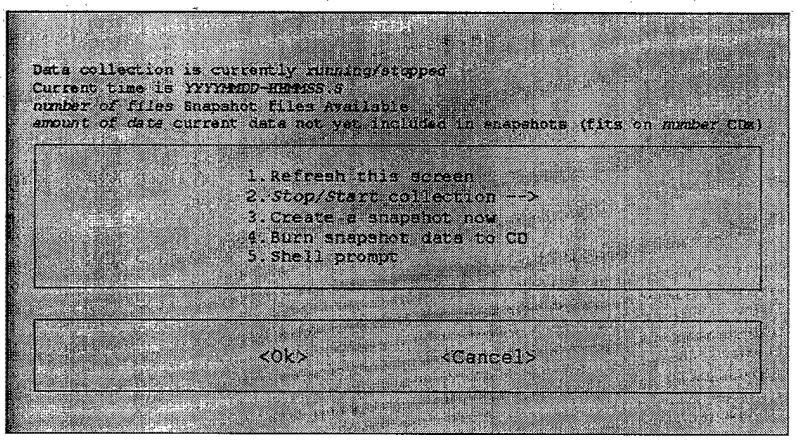

Figure 3.7: NILM Menu Screen

Manual collection of data is also possible by first exiting the menu system by going to the option labeled "Shell prompt". This places the user in the `nilmdata` directory. To create a new directory in which to place the test data, type `mkdir` *`directory name`* and then change to that directory by typing `cd` *`directory name`*. To collect raw voltage and current data in ASCI2 format, type `dd if=/dev/pci1710 | pci2asc >` *`voltage/current textfile`*. This will result in voltage and current being recorded as two columns of text in the file called *`voltage/current textfile`*.

To collect preprocessed power data, type `prep-flush /dev/pci1710 >` *`power file`*. This will result in the fundamental and first three odd harmonics of real and reactive power being recorded as eight columns of text in the file called *`power file`*.

It is also possible to perform both of the preceding operations simultaneously by using the `tee` command. To collect both voltage and current data along with preprocessed power data, type `dd if=/dev/pci1710 | tee` *`voltage/current binaryfile`* `| prep-flush -stdin -p >` *`power file`*. Unfortunately this provides the voltage and current data in a binary format, so to convert to a more useful text file type `more` *`voltage/current binaryfile`* `| pci2asc >` *`voltage/current textfile`*.

In order to be able to plot the data in a program like MATLAB or Octave, open *`voltage/current textfile`* in a text editor and delete any non-numerical information which may occur at the top or bottom of the data.

To manually write data to a CD, change back to the `nilmdata` directory by typing `cd ..` and then creating an iso file of the directory by typing `mkisofs -o` *`directory name.iso`* `-r -J` *`directory name`*. Once the iso file is created, write to the CD by placing a blank CD in the drive and typing `cdrecord -v -eject dev=0,0,0 speed=12` *`directory name.iso`*.

Chapter 4

Cycling System Results

4.1 Sewage System Onboard USCGC SENECA

The sewage system onboard the USCGC SENECA was monitored because is represents an opportunity to perform trending analysis on a cycling system. This cycling system is especially intriguing because its operation is affected not only by physical parameters (e.g., the rate at which the system's two vacuum pumps raise vacuum) but also by human behavior. Monitoring the system's electrical loads and trending their power usage could provide insight into the system's integrity or provide an early indicator of changes in the crew's health.

The system consists of commodes, urinals, and drains which discharge into a vacuum collection tank. Vacuum is maintained in this tank by two pumps which alternately cycle to maintain vacuum between approximately 15 and 10 inches of mercury (in. Hg). Two transfer pumps cycle on and off to occasionally move waste from the vacuum collection tank to a larger sanitary tank. Figure 4.1 shows the system's vacuum pumps with the vacuum collection tank in the background.

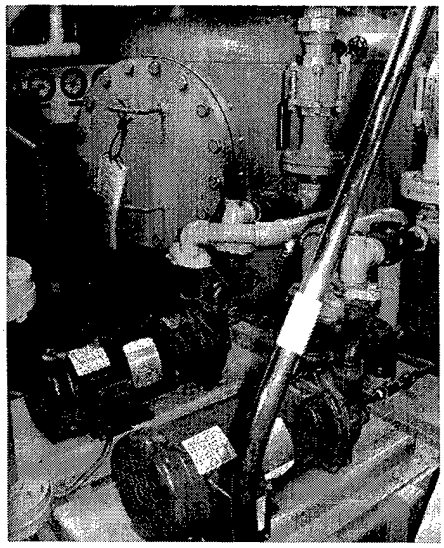

Figure 4.1: Sewage System Vacuum Pumps

4.2 Method of Data Collection and Processing

There is a complete NILM system (as discussed in Chapter 3) monitoring the two vacuum pumps and two transfer pumps that comprise the electrical loads of the SENECA's sewage sytem. One LA 205-S current transducer is monitoring all four electrical loads. The resistors used for the voltage measurement, current measurement, and references are 130 Ω, 66.5 Ω, and 56.2 Ω, respectively. Upon initial system installation, the system was calibrated by collecting balanced three-phase power data with a Fluke 39 Powermeter and comparing it to the power counts obtained with the NILM. The resultant scaling factor between the measured power (1.42 kW) and counts (-2287.2) was -0.61946 $\frac{Watts}{count}$.

Data was collected in one hour "snapshots" in order to trend the cycling of electrical loads (primarily the vacuum pumps). A typical hour of power data is shown in Figure 4.2. An expanded view of the first pump run in this typical hour is shown in Figure 4.3. Figure 4.2 shows that the electrical power drawn by each pump is approximately equal.

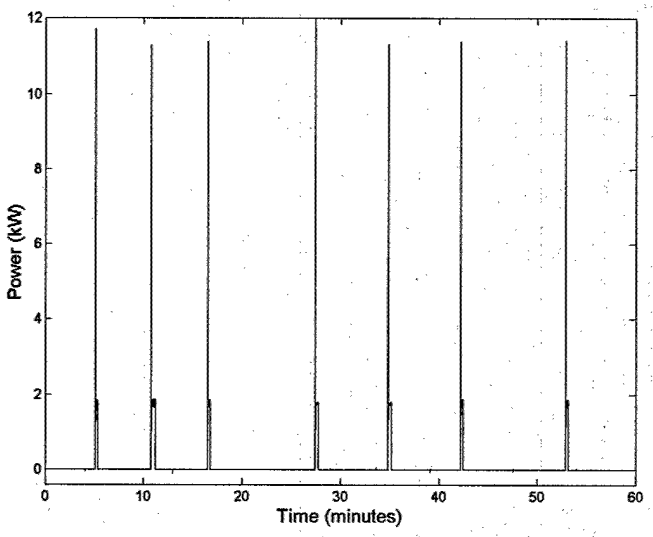

Figure 4.2: Vacuum Pump Transients for One Hour of Weekend Use

Because of the relatively large power transient associated with startup and the subsequent variations in steady state power, pump runs like those shown in Figure 4.3 are difficult to trend with respect to time. For this reason, a MATLAB script entitled pumprun was written to accept an hour of sewage system "snapshot" data as input and provide the number of pump runs and average run time per pump run as outputs. The characteristics of this script are as follows (see Appendix C for the script itself):

- Unscaled power data (i.e. in terms of counts, not W or kW) is processed into binary form by assigning a value of "1" to data points of greater than 500 counts and a value of "0" to data points of less than or equal to 500 counts. The binary version of Figure 4.2 is shown in Figure 4.4.
- The binary power data is examined for any changes from the off (0) state to the on (1) state. Anytime in the binary data that a 0 is followed by a 1, the run counter is increased

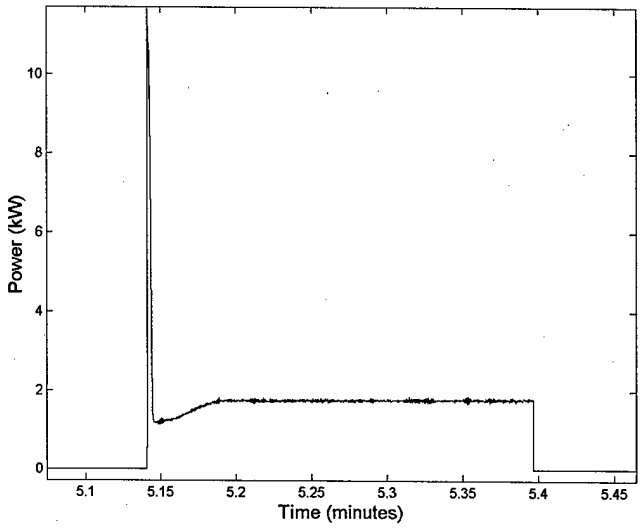

Figure 4.3: Vacuum Pump Start

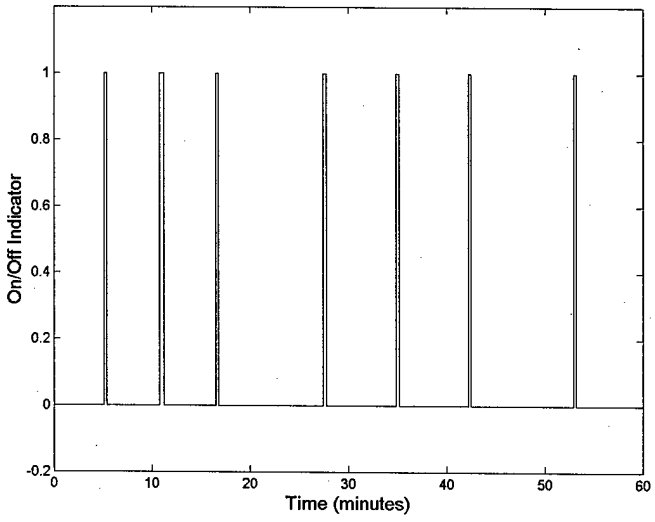

Figure 4.4: Binary Form of Vacuum Pump Transients

by 1. If the first element of the binary power data is a 1, then the run counter starts with a value of 1 instead of 0 since a pump was already running when data collection commenced.

- The binary power is summed and then divided by 120 (the sampling frequency in Hz for the original power data) and the number of pump runs to obtain the average run time per pump run in seconds.

4.3 Sewage System Simulation

The fundamental problem with performing controlled tests on a system like the sewage system onboard the SENECA is control of the human element. Although it is possible to insert vacuum leaks of various quantifiable sizes into the system and then trend the resulting system cycles, it is not possible to control the main factor which effects the amount of system run time, the amount of usage by the ship's crew. In order to determine effects of vacuum leaks and crew usage on system run times independently, the MATLAB script `flushsim` was written to simulate the system behavior. The simulation accepts as input the average time between system usage events and vacuum leak rate (in inches of Hg per minute) and provides the number of pump runs and average run time per pump run as outputs. The characteristics of the simulation, which can be found in Appendix C, are as follows:

- Although not an explicit input, the number of minutes for which the simulation runs along with the number of calculations used per minutes can be varied by changing the parameters "n" and "k", respectively.
- The simulation is written from the standpoint of pressure, with pressure maintained between 15 and 10 inches (Hg) of vacuum. Whenever vacuum falls to less that 10 in., a pump run indicator is switched to the "on" state. When vacuum exceeds 15 in., the pump run indicator switches back to the "off" state. If vacuum should fall to less than 7.5 in. due to a large leak rate or heavy system usage, both pumps are turned on (or in the case of a pump already running, the other pump is turned on).
- To increase realism, the two pumps in the simulation have different vacuum drawing rates (19 and 17 in. per minute).
- A system usage event, henceforth referred to as a "flush", is modelled as a discrete vacuum drop of 1 in. The probability of a flush is calculated using the triangular probability density function (pdf) shown in Figure 4.5. A triangular probability distribution was chosen because it was deemed complex enough to add realism to the simulation while being simple enough to allow for speed of calculation. This pdf is based on the average time between flushes entered as input (t_{mean}) and assumes that if the probability of a flush occurring within t_{mean} is 0.5, then the probability of a system usage event occurring within $2t_{mean}$ is one. At each point in the simulation, the probability of a flush occurring is calculated (based on the amount of time which has elapsed since the last flush) from the assumed pdf and compared to a randomly generated number. If the random number is less than the probability a flush occurs, vacuum drops by 1 in., and the flush counter is reset. If the random number is greater than or equal to the probability no vacuum drop occurs and the probability of a flush will be slightly higher.
- The number of pump runs and average run time per run is calculated from the pump run indicator vector in the same manner as for real data.

A sewage system simulation run showing vacuum information and the pump status indicator are shown versus time in Figure 4.6. The simulation was run for an average of four minutes between flushes with no vacuum leak.

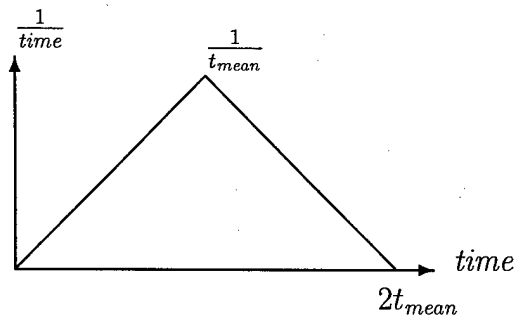

Figure 4.5: Vacuum System Usage Probability Density Function

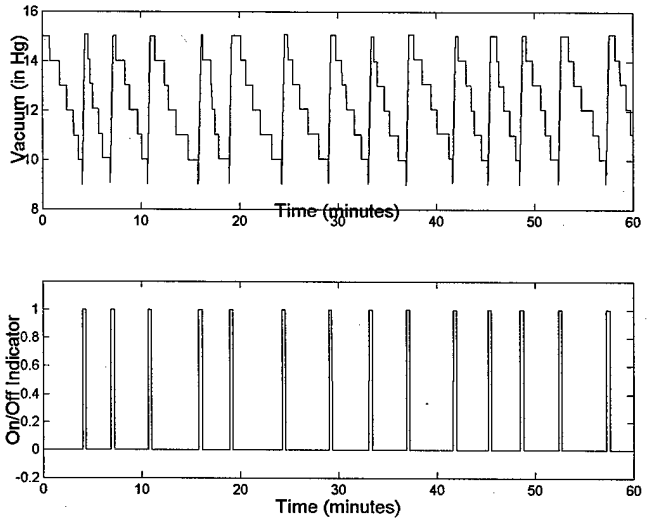

Figure 4.6: One Hour of Simulated Vacuum and Vacuum Pump Cycling

4.4 Trending of System Cycling for Various Vacuum Leaks

In order to trend the cycling of the vacuum pumps with a fault in the sewage system, vacuum leaks of varying sizes were inserted into the sewage system onboard the SENECA. The vacuum leak was controlled (and quantified) by a flowmeter attached to a gauge line connection just off the vacuum collection tank. The flowmeter is shown in Figure 4.7.

The throttle valve on the flowmeter was adjusted to achieve the desired flow rate and NILM snapshot data was collected. The flowmeter contains two different balls, one made of stainless steel and one made of plastic. For consistency, leak rates specified throughout this chapter are the leak rates read off of the plastic ball immediately after adjusting the flowmeter to a new leak rate. Leak data is contained in Appendix D. A snapshot of leak data is shown in Figure 4.8.

There are two differences between Figure 4.8 and Figure 4.2 shown before, Figure 4.8 shows cycling of vacuum pumps on a weekday with a leak of 62.5 standard cubic feet per hour (SCFH) present while Figure 4.2 shows cycling of vacuum pumps on a weekend day with no vacuum leak

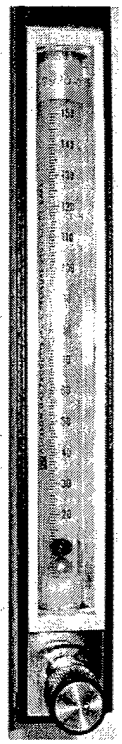

Figure 4.7: Flowmeter Used to Insert and Quantify Vacuum Leaks

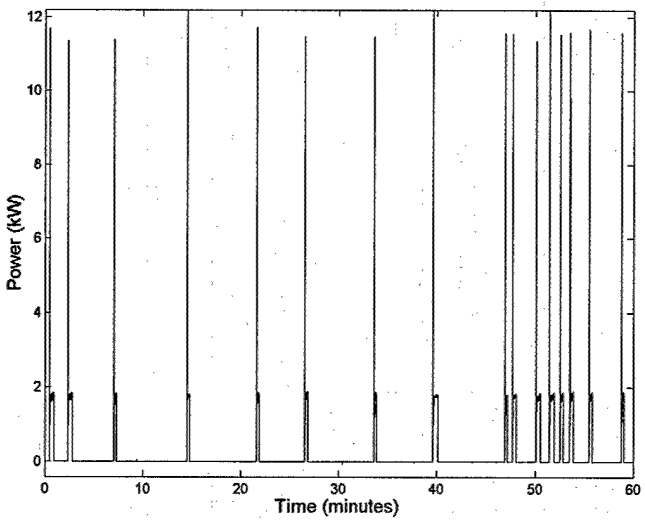

Figure 4.8: Vacuum Pump Transients for One Hour of Leaking Weekday Use

present. The two hours represented by Figures 4.2 and 4.8 are summarized in Table 4.1.

Table 4.1: Comparison of Two Different Hours of Data from SENECA

Leak Rate (SCFH)	0 (Weekend)	62.5 (Weekday)
Vacuum Pump Runs	7	16
Average Run Time per Run (seconds)	17.89	20.77
Total Run Time (seconds)	125.23	332.32

It can be seen from Table 4.1 that the total run time for the weekday is higher than for the weekend day. But is the higher total run time due to heavier usage or the presence of a vacuum leak? Secondly, and perhaps of equal importance, does the increased total run time manifest itself as an increase in the number of pump runs per hour, the average run time per pump run, or a combination of the two?

4.4.1 Dependence of Total Run Time

In order to determine the variation of total run time on different factors, the sewage system simulation was used to create a large amount of data. The simulation (as discussed previously) was run for combinations of 13 different average flush times and 11 different leak rates. Each one of these combinations was run 24 times and averaged. The result of these simulation runs was three different 13 by 11 arrays. Each element of the arrays represents total run time, number of pump runs, or average run time per run for one hour of vacuum pump cycling.

Since the ultimate goal of trending the sewage system data is to be able to detect a vacuum leak in the presence of system usage variations, scattergrams were produced which plotted total run time vs. either number of runs or average run time per run for different levels of usage with a constant leak rate. The scattergrams are shown in Figures 4.9 and 4.10.

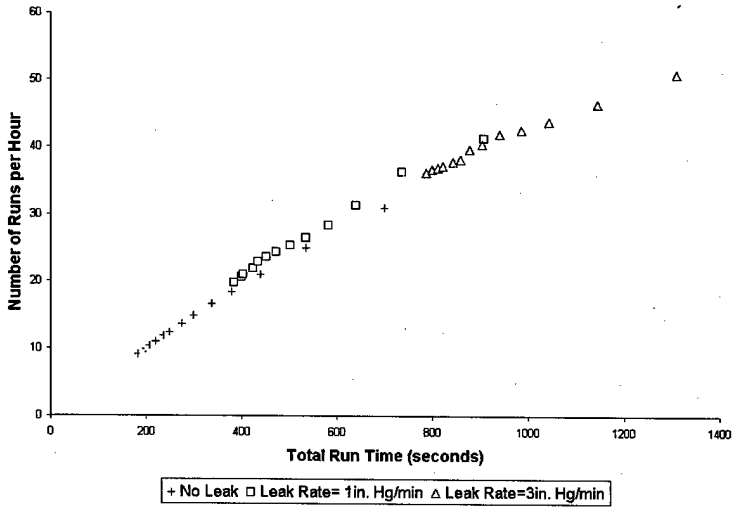

Figure 4.9: Scattergram of Total Runtime vs. Number of Runs for Three Simulated Leak Conditions

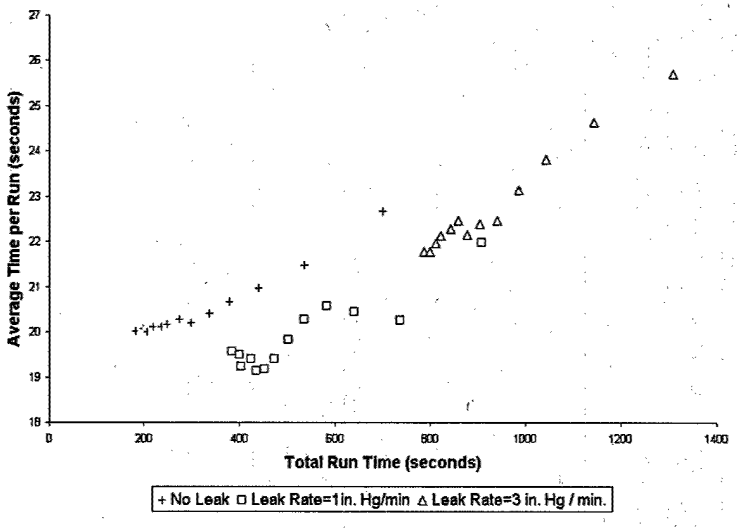

Figure 4.10: Scattergram of Total Runtime vs. Average Run Time per Run for Three Simulated Leak Conditions

Figure 4.9 indicates that total run time seems to be related to number of pump runs in a more linear fashion than the average run time per run. For higher leak rates, the total run time appears to only shift along the same line to higher values. It is for these reasons that the number of pump runs was focused on in the analysis of real leak data.

4.4.2 Development of the Leak Indicator

The following steps (which will be discussed in more depth below) summarize the development of the leak indicator:

1. Snapshot data for several hours of data is uncompressed and run through the `pumprun` Matlab script discussed previously to determine the number of pump runs and total run time for that hour of data. This effectively distills an hour of power data into only two numbers.
2. The number of pump runs and total run time is tabulated for all hours of data collected.
3. The average number of runs per hour and standard deviation in number of runs per hour is calculated. The average used was the arithmetic mean.
4. A linear regression is performed on total run time vs. number of pump runs for the tabulated hourly data.
5. The leak "indicator" is the standard deviation in pump runs and the y-intercept from the linear regression subtracted from the average number of runs per hour.

The leak indicator starts with the average number of pump runs per hour and standard deviation in number of pump runs as calculatated with equations 4.1 and 4.2. $\overline{Runs}$ is the average number of pump runs, n is the number of hours under consideration, $Runs_i$ is the number of runs for the i^{th} hour, and s_{Runs} is the standard deviation in number of pump runs.

$$\overline{Runs} = \frac{\sum_{i=1}^{n} Runs_i}{n} \tag{4.1}$$

$$s_{Runs} = \sqrt{\frac{\sum_{i=1}^{n} \left(Runs_i - \overline{Runs}\right)^2}{n-1}} \tag{4.2}$$

Since it has already been shown that the amount of pump run time is directly related to number of pump runs, it was felt that the average number of pump runs was a logical starting point for analysis. After calculating the statistics ($\overline{Runs}$ and s_{Runs}) for the number of pump runs, it became clear that the average number of pump runs could not be used alone as an indicator of a vacuum leak. The statistics for the number of pump runs are summarized in Table 4.2.

Table 4.2: SENECA Vacuum Leak Statistics

Leak Rate (SCFH)	$\overline{Runs}$	s_{Runs}
132.5	21.57142857	4.878749615
102.5	11.34782609	2.207604536
62.5	14.52173913	4.429955522
51	14.2173913	5.767909041
42	12.40909091	5.160833182
0	9.136363636	2.623981971

As seen in Table 4.2, the average number of runs for the leak rate of 102.5 SCFH does not follow the trend evident in the rest of the table. It should also be noted however, that the standard deviation in the number of pump runs for the 0 and 102.5 SCFH leak rates is much lower than the other leak rates. The previous observations are shown in Figure 4.11 with the pump run statistics used to plot normal distributions (see [13]) in accordance with equation 4.3. It should be noted that plotting the pump run statistics as a normal distribution is for illustrative purposes only since there were no tests to determine if the pump run data actually followed a normal distribution.

$$f(x) = \frac{1}{\sqrt{2\pi}s_{Runs}} e^{\left[-\frac{\left(x-\overline{Runs}\right)^2}{2s_{Runs}^2}\right]} \tag{4.3}$$

The difference in both the average number of pump runs and standard deviation in pump runs is due to the day of the week that the data was taken.

Since the ultimate goal of trending the leak data was to develop a parameter which detected the presence of a vacuum leak regardless of the amount or variance in system usage by the crew, the standard deviation was subtracted from the average number of pump runs to negate the difference between weekend days and weekdays. Since a vacuum leak is a continuous drain on the system and therefore does not affect the system differently from one hour to the next, performing this subtraction removes a value which is only affected by crew usage. The standard deviation in number of pump runs subtracted from the average number of pump runs is dubbed the "pump run lower bound".

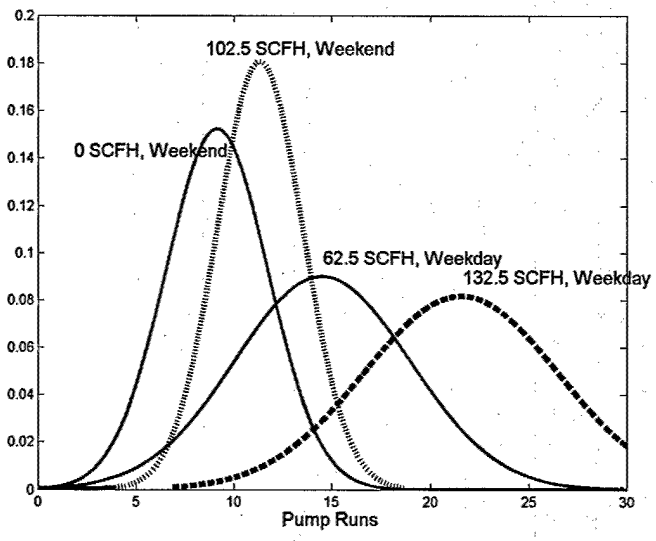

Figure 4.11: Normal Distributions for Number of Pump Runs at Different Leak Rates

The next step of developing a leak indicator was to plot the total run time vs. number of pump runs as shown in Figure 4.12.

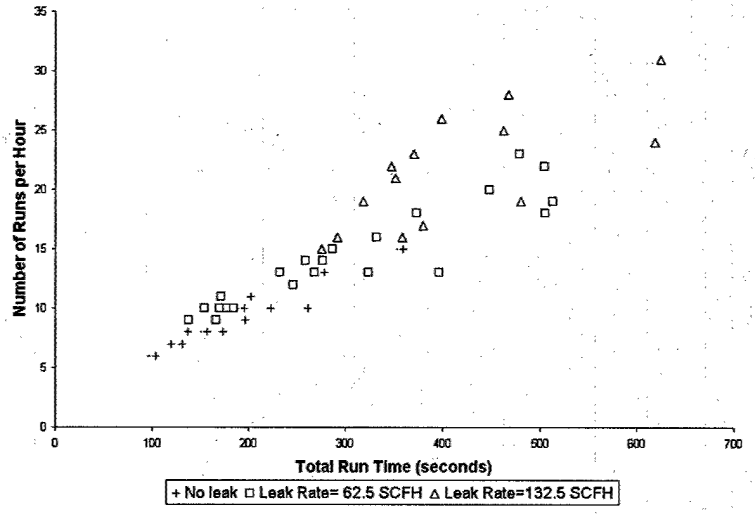

Figure 4.12: Scattergram of Total Runtime vs. Number of Runs for Three Real Leak Conditions

Even though the data shows more scatter than in the simulated case[1], it still shows a generally linear trend. A least squares linear regression was therefore performed in accordance with [13] for

[1]This could be a result of the simulation being too simplistic or unable to account for all of the complexities of the real system

total run time vs. number of runs to determine how the slope and y-intercept varied with leak rate.

The following is an outline of the linear regression process:

1. It is desired to fit the data to an equation of the form

$$y = \hat{\beta}_1 x + \hat{\beta}_0 \tag{4.4}$$

So that the total amount of deviation between the regression line and the observed points as given in equation 4.5 is minimized.

$$S(\beta_0, \beta_1) = \sum_{i=1}^{n} [y_i - (\beta_0 + \beta_1 x_i)]^2 \tag{4.5}$$

2. To minimize the value of S with respect to both β_0 and β_1, the partial derivative of S with respect to β_0 and β_1 is set to zero.

$$\frac{\partial S(\beta_0, \beta_1)}{\partial \beta_0} = 2 \sum_{i=1}^{n} [y_i - (\beta_0 + \beta_1 x_i)] (-1) = 0 \tag{4.6}$$

$$\frac{\partial S(\beta_0, \beta_1)}{\partial \beta_1} = 2 \sum_{i=1}^{n} [y_i - (\beta_0 + \beta_1 x_i)] (-x_i) = 0 \tag{4.7}$$

3. Rearranging results in two equations in terms of $\hat{\beta}_0$ and $\hat{\beta}_1$.

$$\hat{\beta}_0 n + \hat{\beta}_1 \sum_{i=1}^{n} x_i = \sum_{i=1}^{n} y_i \tag{4.8}$$

$$\hat{\beta}_0 \sum_{i=1}^{n} x_i + \hat{\beta}_1 \sum_{i=1}^{n} x_i^2 = \sum_{i=1}^{n} x_i y_i \tag{4.9}$$

4. This results in the following expressions for $\hat{\beta}_0$ and $\hat{\beta}_1$.

$$\hat{\beta}_1 = \frac{\sum_{i=1}^{n} (x_i - \overline{x}) y_i}{\sum_{i=1}^{n} (x_i - \overline{x})^2} \tag{4.10}$$

$$\hat{\beta}_0 = \overline{y} - \hat{\beta}_1 \overline{x} \tag{4.11}$$

The results of these linear regressions are shown in Table 4.3.

Table 4.3: Leak Data Linear Regressions of Total Run Time (x) vs. Number of Pump Runs (y)

Leak Rate (SCFH)	$100\hat{\beta}_1$	$\hat{\beta}_0$
132.5	3.255679235	8.198074977
102.5	3.369926448	3.770605077
62.5	3.14937023	4.785337827
51	3.314663182	3.668129851
42	3.65228987	2.817812481
0	3.40888463	2.852549669

Table 4.3 shows intercepts that are all non-zero. Since the y-axis in the linear regression is number of pump runs, the interpretation of non-zero intercepts is that for zero total run time, there will be more than zero pump runs. There are two possible explanations for this phenomenon. Either there is a leak in the system other than the one placed in it for testing or the behavior of the system for low total run times is non-linear.

Since in reality there would be zero pump runs for zero total run time, the y-axis should be shifted upwards by a correction factor equal to the y-intercept for each of the data sets considered. So the final leak indicator is the pump run lower bound discussed above minus the y-intercept from the linear regression of total run time vs. number of pump runs as shown in equation 4.12.

$$Leak\ Indicator = \overline{Runs} - s_{Runs} - \hat{\beta}_0 \tag{4.12}$$

This final number is an indicator of amount of vacuum pump cycling above the no-cycling level. The leak indicator is plotted vs. leak rate in Figure 4.13 for the leak data taken aboard the SENECA.

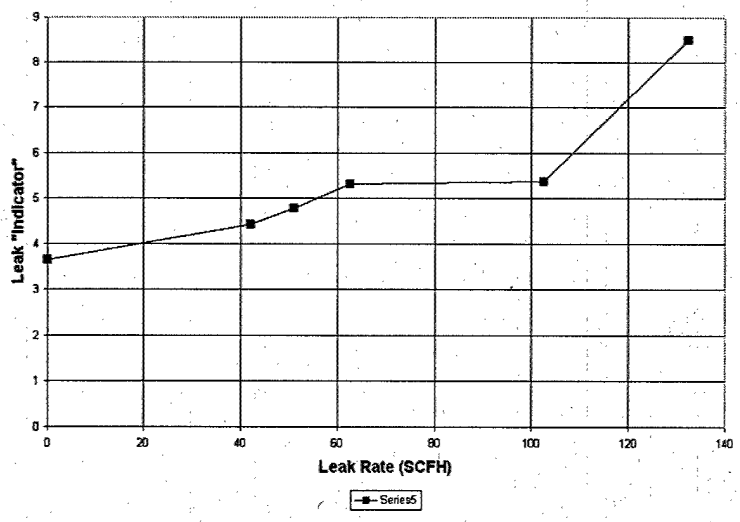

Figure 4.13: Leak Rate vs. Leak "Indicator"

4.4.3 Validation of the Leak Indicator

In order to verify the ability of the the leak indicator to show the presence of a leak regardless of the amount of system usage, more simulation data were created. Weekend and weekday data were simulated for 24 hours for several different leak rates and the leak indicator calculated. The weekday simulations had a lower average time between flushes with a higher variation in time between flushes while the weekend simulations had a higher average time between flushes with a lower variation in time between flushes (see Appendix D). The weekday and weekend results are shown in Table 4.4 and Figure 4.14.

Table 4.4: Leak Indicator Summary

Leak Rate (in. Hg/min.)	Weekday Leak "Indicator"	Weekend Leak "Indicator"
0	6.296625689	5.903347459
0.5	9.973276855	11.47976765
1	14.21729058	17.16598438
1.5	17.33927728	18.96290688
2	17.48596088	17.69171294
2.5	19.17635935	18.64716683

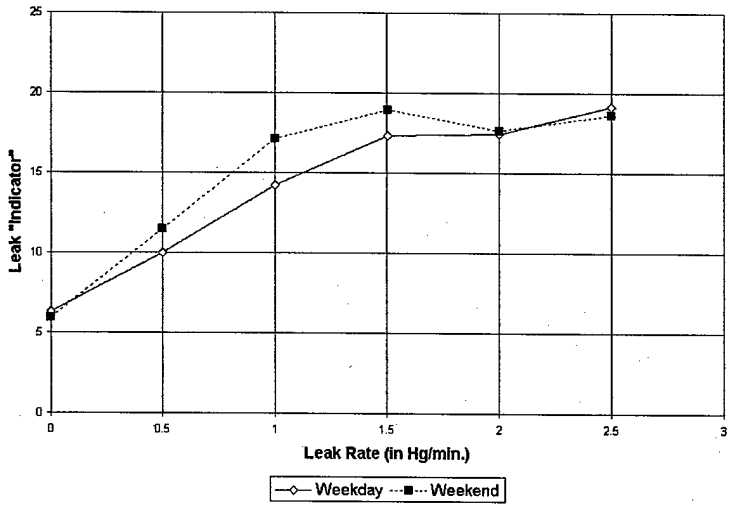

Figure 4.14: Leak Rate vs. Leak "Indicator" for Simulation Data

It is encouraging to note from Figure 4.14 that as with the leak indicators developed for the actual shipboard data, there is a fairly linear relationship between leak indicator and leak rate independent of system usage. It is also important to note that the leak indicators for the weekend and weekday cases are very similar for the two no leak cases.

4.5 Chapter Summary

The results presented previously in this chapter show the existence of a leak indicator for cycling systems that can be used to detect a fault in the system. This leak indicator uses the statistics of pump runs to arrive at a figure of merit which does not depend on the amount or variation in system usage.

The leak indicator was developed from a purely empirical standpoint based on observations made from collected data and physical reasoning. The best way of determining its ability to detect faults is to take data on others system that involve cycling components

Chapter 5

Fluid System Results

5.1 ASW System Onboard USCGC SENECA

The auxiliary seawater (ASW) system onboard the USCGC SENECA provides cooling for all heat loads onboard the ship other than those associated with the main engines. Heat loads cooled include the HVAC units, refrigerators and freezers, diesel generator air coolers, and diesel generator lube oil coolers. Suction to the two ASW pumps is taken through two supply lines from the bottom of the ship through suction screens, isolation globe valves, suction strainers, and butterfly valves. The isolation globe valves determine which suction is providing ASW cooling while the butterfly valves allow isolation of the strainers for cleaning. A butterfly valve across the inlets also allows cross-connecting the system to provide redundancy. Changing the flow rate is accomplished by throttling two butterfly valves at the outlets of the two pumps: a pump is started with the overboard throttle valve completely open and the heat load throttle valve shut, then the heat load throttling valve is opened and the overboard throttle valve is partially shut. The overboard valve is throttled until a pressure gauge in the supply line for the heat loads shows a pressure of approximately 35 psig. Figure 5.1 shows a one-line diagram of the system while Figure 5.2 shows some of the components at the inlets to the pumps.

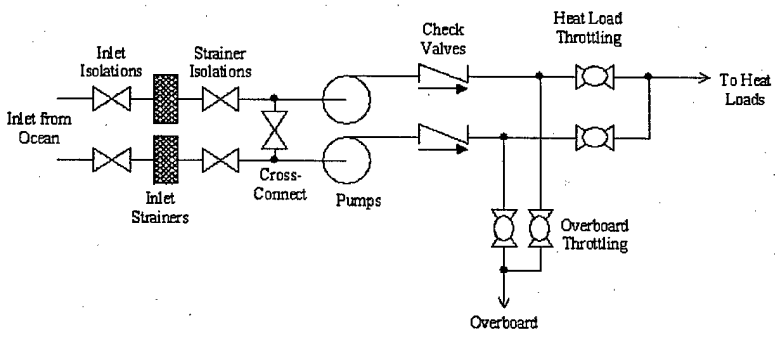

Figure 5.1: ASW System Schematic

Since seawater cooling systems are common across a wide range of ships, monitoring the seawater cooling system on a ship with many heat loads was seen as an opportunity to examine how the power usage of the pumps that maintain flow in the system varies with changes in the flow

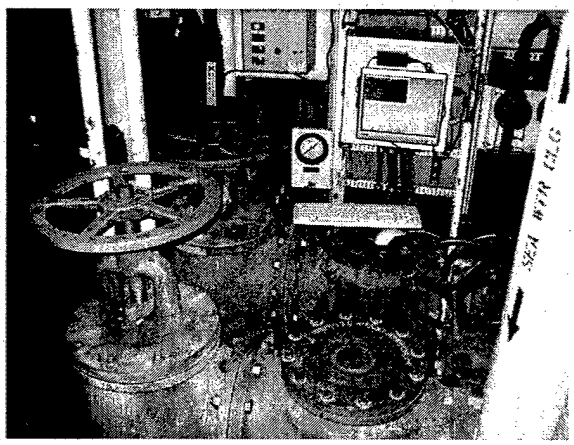

Figure 5.2: ASW Inlet Isolation Valves and Strainers

characteristics upstream and downstream of the pumps. Specifically, it was desired to know how pump power would change for differing amounts of flow that was sent to heat loads, clogging in the inlet strainers, sudden rapid failure of the coupling beween motor and pump, and flow blockage that might occur in any of the heat loads. The last item was especially important because several crewmembers of the USCGC SENECA had made reference to mussels growing inside the endbells of tube-and-shell heat exchangers in the diesel generators and the HVAC units. It was therefore deemed especially important to focus attention on this problem to provide a possible prediction of heat exchanger fouling well in advance of a rise in temperature.

The NILM installation for the ASW system uses one voltage transducer and two current transducers to monitor the two seawater pumps that pressurize the supply header. Since there is no one panel that supplies both of the pumps (for reliability), one LA 305-S current transducer had to be placed in each pump controller and the output combined at the NILM box. The resistors used for the voltage measurement, current measurement, and references are 130 Ω, 7.5 Ω, and 56.2 Ω, respectively. Upon initial system installation, the system was calibrated by collecting balanced three-phase power data with a Fluke 39 Powermeter and comparing it to the power counts obtained with the NILM. The resultant scaling factor between real power (29.5 kW) and counts (4150.8) was 7.11 $\frac{Watts}{count}$.

5.2 Fluid Test System

The ASW system onboard the SENECA is very promising as a system on which to conduct research into the relationships between fluid dynamics and electrical power usage, but there are a few drawbacks:

- Availability. The SENECA is only available for short periods of time while in port. This coupled with the very aggressive maintenance and repair schedule while in port means that crewmembers have very little time in their busy schedule to assist with data collection.
- Complexity. Since the ASW system is sized to cool many different heat loads all around the ship, the system contains a large number of components as well as a large amount of piping. As a result, there are complex interactions in the system which can be difficult to

model or predict. Also, the effect of a small change in one of the many components may not be significant enough to be noticed in the power signature of the pumps.

- Controllability. In order to predict the response of the ASW system to specific faults, it would be necessary to take test data with those faults inserted into the system. For example, to see how mussels growing inside of a diesel generator lube oil cooler effects the power signature of the two pumps, it would be necessary to clog tubes in the heat exchanger. Since this is impractical, the clog can only be simulated by throttling the inlet valve to the heat exchanger. Although it might be possible to create the same pressure drop across the heat exchanger by doing this, it is does not necessarily reproduce the more complicated hydrodynamic phenomena (or the *same* phenomena) that occur when tubes are actually blocked.

Because of the limitations stated above, a fluid test system was constructed to collect data in the laboratory. Such a system has unlimited availability, a relatively low number of components, and a much higher level of controllability (in the sense that it is easier to change the fundamental characteristics of the components that comprise it).

The fluid test system that was constructed consists of a three-phase 0.5 hp pump that takes a suction on a large water reservoir, pumps the water through some combination of three parallel flow paths, then returns the water to the water reservoir. A one-line diagram of the fluid test system is shown in Figure 5.3 while Figure 5.4 provides a front view.

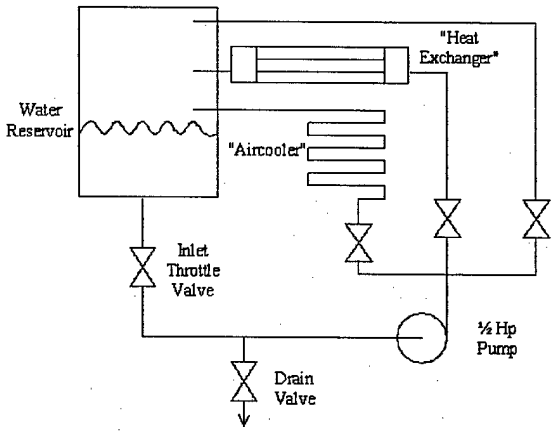

Figure 5.3: Fluid Test System Schematic

The pump suction run consists of a 0.75 in. globe valve attached to 1 in. PVC piping. A small ball valve and plastic tubing are provided to easily drain the system when not in use. The pump outlet piping consists of three different branches, each consisting of .75 in. copper tubing with a .75 in. globe to provide isolation and throttling.

Two of the branches contain "heat loads" while the third branch returns directly to the water reservoir. One of the two "heat load" branches is a section of pipe which makes seven 180 degree turns to mimic the construction of a water-to-air heat exchanger as one might find in the generator section of a diesel generator.

The other "heat load" branch is constructed as a tube-and-shell heat exchanger, as one might use to cool lubricating oil in a diesel engine or refrigerant in an HVAC plant. The heat exchanger

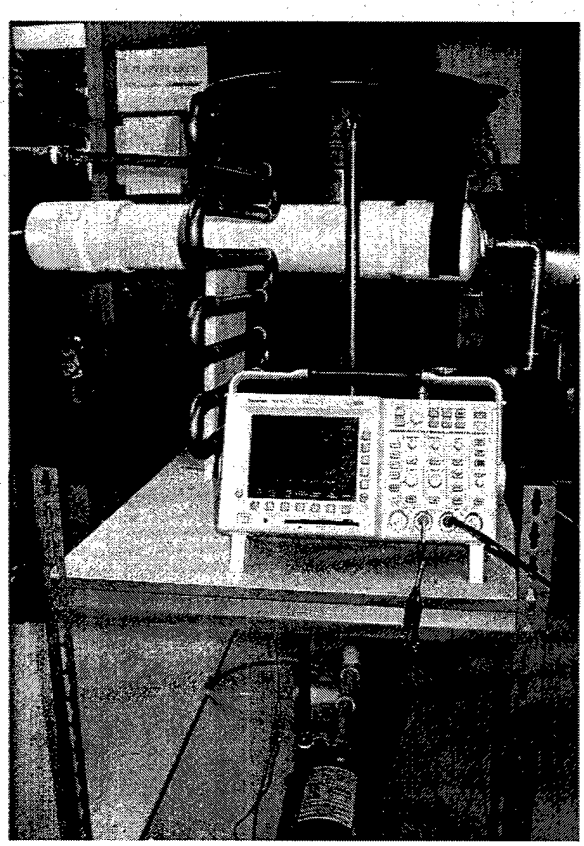

Figure 5.4: Fluid Test System Front View

(henceforth abbreviated HX) consists of seven 0.5 in. PVC tubes attached to tubesheets at both ends, mounted inside of a 4 in. PVC tube. Figure 5.5 shows the HX prior to assembly.

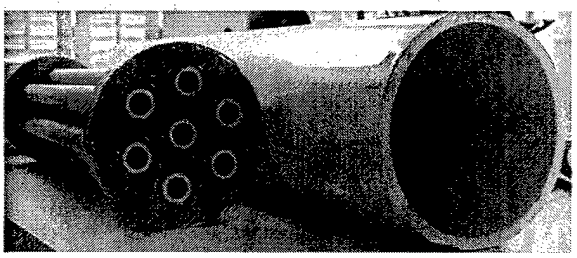

Figure 5.5: Fluid Test System HX Prior to Assembly

Water in the test system flows through .75 in. copper piping, into the 4 in. inlet HX endbell, through the inside of seeven 0.5 in. PVC tubes, into the 4 inch outlet HX endbell, and finally through a run of .75 in. copper piping back to the water reservoir. This flowpath represents the flow of the cooling medium (such as seawater) through the HX. Since the phenomena of interest are hydrodynamic and not thermodynamic, the HX was not designed to actually transfer any heat. If it had been designed to do so, there would be a second flowpath in which the fluid being cooled would flow around the outside of the small tubes, which would be made of copper (or some

other metal to provide a high coefficient of heat transfer) and not PVC.

Electrically, the pump power and NILM monitoring are combined in a single NEMA enclosure. The enclosure contains the components for a NILM box discussed in Chapter 3 as well as a three-phase switch and an LA 55-P current transducer. The resistors used for the voltage measurement, current measurement, and references are 130 Ω, 66.5 Ω, and 56.2 Ω, respectively. Upon initial system construction, the system was calibrated by collecting balanced 3-phase power data with a Fluke 39 Powermeter and comparing it to the power counts obtained with the NILM. The resultant scaling factor between real power (152 W) and counts (-440.58) was -0.345 $\frac{Watts}{count}$.

5.3 Building a Centrifugal Pump Simulation

A simulation of a centrifugal pump startup was developed for the following reasons:

- Simulations based on physical principles offer a means of validating understanding of the system upon which they are based.
- They offer the ability to quickly collect large amounts of simulated data while varying many different parameters, often in an automated fashion.
- They provide an approximation of system behavior for situations which are not possible or feasible to reproduce in the laboratory (especially catastrophic failures).

The simulation that was constructed takes known parameters for an induction motor and couples them to a fictitious pump impeller which is geometrically similar to the pumps onboard the SENECA. The motor model from [15] is a fifth-order model of an induction motor with a rated power of 3 hp. Since pump curves for the ASW pumps onboard the SENECA were available in [16], it was possible to scale the pump impeller to the much smaller motor. The pumps onboard the SENECA are powered by 40 hp induction motors, but the operating point specified in [16] corresponds to a brake horsepower (BHP) of only 31 hp. Using the same ratio of motor power to pump BHP, it was decided that the scaled pump head would therefore have a brake horsepower of 2.25 hp. The ASW pump motors also have two poles versus the simulation motor's four, so the simulation pump was assigned an operating speed of 1775 revolutions per minute (rpm) versus the ASW pump's 3550 rpm.

5.3.1 Inertial Considerations

The first consideration when adding a pump impeller to an electric motor is the additional moment of inertia added by the pump impeller itself as well as the moment of inertia added by the water being pumped. The first step in estimating these two moments of inertia was to determine the pump impeller diameter through geometrical scaling. The diameter of the pump impeller was scaled using the power coefficient given in [1] by equation 5.1.

$$C_P = \frac{P}{\rho \omega^3 D^5} \tag{5.1}$$

Maintaining this coefficient constant for the same pumped fluid leads to an expression for the diameter of the scaled pump impeller as shown in equation 5.2. The calculated value of the simulated pump diameter was 5.30 in.

$$D_2 = D_1 \sqrt[5]{\frac{P_2 \omega_1^3}{P_1 \omega_2^3}} \tag{5.2}$$

Given the diameter of the pump impeller, a three-dimensional model was created in Rhino 3D© software[1]. This program was used because its built in analysis functions allowed easy calculation of the impeller's moment of inertia. The pump impeller from the fluid test system described earlier was used as a model for the geometry of the simulated impeller. The only difference was that the simulated pump impeller is designed with an additional plate on the inlet side of the rotor to make it a "closed rotor" design instead of the "open rotor" design used in the fluid test system. It was felt that this was much closer to the style of impeller used on larger pumps like those found in the ASW system of the SENECA. In addition to having the scaled diameter determined previously, the front and back plates are .25 in. thick with vanes .5 in. thick. There is a .5 in. diameter hole in the back plate for the motor shaft and a 1 in. diameter hole in the front plate as an inlet into the center of the impeller. The fluid test system impeller and simulation impeller are shown in Figures 5.6 and 5.7, respectively. The simulated pump impeller is shown with the inlet-side plate removed.

Figure 5.6: Fluid Test System Pump Impeller

As stated before, moments of inertia were calculated from the rendering program. A solid disk encompassing the entire pump rotor was first created and its second moment of volume calculated. The second moment of volume for the pump impeller was separately calculated and subtracted from the total disk moment to arrive at a second moment of volume for the entrained water. These second moments of volume are purely geometric quantities, so had to be multiplied by material densities to arrive at moments of inertia. Densities of 1 $\frac{g}{cm^3}$ and 7.85 $\frac{g}{cm^3}$ were used to arrive at moments of inertia of 0.000366 $kg-m^2$ and 0.00364 $kg-m^2$ for the water and impeller, respectively. The value of density for the pump impeller assumes that it is made of stainless steel.

An alternate method of determining the moment of inertia for the pump impeller and entrained water from [17] is showin in equation 5.3. P in the equation is the shaft power in kW and N is the rotational speed in rpm.

$$I = 1.5 \cdot 10^7 \left(\frac{P}{N^3}\right)^{0.9556} \tag{5.3}$$

[1]Rhino-CAD is a product of Robert McNeel and associates

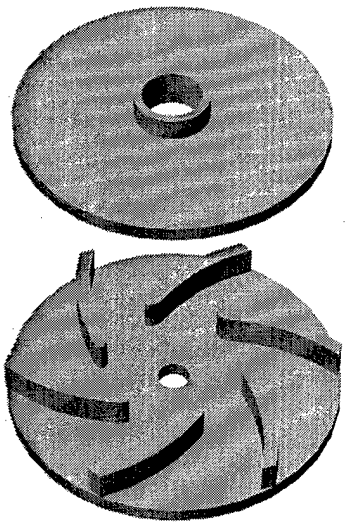

Figure 5.7: Simulated Pump Impeller

According to [17], the formula was developed from a linear regression of "...248 data points from 5 different pump manufacturers". Using a shaft power or 1.679 kW (2.25 hp as stated earlier) and a rotational speed of 1775 rpm yields a moment of inertia of 0.0119 $kg - m^2$. This value is over 2.5 times larger than the value calculated before. This formula was not used since there is not enough known about the type of pumps considered in the development of the empirical relationship. Specifically, there is not description of the type of pump impellers used and it was not known if pumps of low power (less than 5 hp) were included.

5.3.2 Hydrodynamic Considerations

To determine the amount of torque on the pump impeller as a function of speed, the power coefficient of equation 5.1 was again employed. In this case, it is not maintained constant for two pump impellers which are geometrically similar but for a pump impeller rotating at different speeds. Since the density of the fluid and pump impeller diameter do not change with speed, equation 5.1 reduces to equation 5.4.

$$\frac{P}{\omega^3} = \frac{P_0}{\omega_0^3} \tag{5.4}$$

Since mechanical power is just the torque placed on the rotor times its angular speed, this further reduces to equation 5.5.

$$T\omega = P_0 \frac{\omega^3}{\omega_0^3} \tag{5.5}$$

Dividing through by the angular speed gives an expression for torque in terms of angular speed as in equation 5.6.

$$T = P_0 \frac{\omega^2}{\omega_0^3} \tag{5.6}$$

Finally, since it was decided that the pump would draw 2.25 hp at 1775 rpm (185.88 $\frac{rads}{s}$), the final expression for torque is developed in equation 5.7. It should be noted that this development of torque vs. angular speed is inherently quasi-steady. Applying this relationship to determine the hydrodynamic torque assumes that the stator is stepping through a series of steady states as it speeds up without any consideration of more complicated hydrodynamics such as transitions from laminar to turbulent flow. This is adequate however, because the simulation was used to explore changes in steady state power levels, not changes in the start up transient for the pump.

$$T = 0.0002614\omega^2 \tag{5.7}$$

The scripts used to implement the centrifugal pump simulation are contained in Appendix E.

5.4 Steady State Power Level as an Indicator of Pump Performance

There are fundamentally three "bands" of pump power discussed in this section. The first is the band that corresponds to operation with the overboard valve throttled to various levels. This normal operation band can be used to predict the total amount of flow from the pump. The second band corresponds to a problem on the inlet side of the pump, such as a clogged inlet strainer, resulting in a lower steady state power. The last band is below the second power level and corresponds to a problem with the coupling between the pump motor and the pump impeller. For this last case, power levels during an uncoupling even drop below zero.

5.4.1 The NILM as an Indicator of Flow

Test Data

One of the first goals of placing the NILM on the ASW system of the SENECA was to see if steady state values of power could be used as an indicator of flow through the system. To that end, the system was run with the overboard valve throttled to various degrees and power data collected. An HVAC unit and two diesel generators were aligned to the system as heat loads. As previously discussed, the overboard valve is throttled to control the amount of flow to the heat loads in the system. If the overboard valve is throttled down, there is less water flowing directly over the side and therefore more water flowing to the heat loads (see Figure 5.1).

The overboard throttling valve is a butterfly valve that has discrete settings from notches cut in the operating handle. A valve of this type (but not the actual valve in question) is shown in Figure 5.8.

For each setting of the overboard throttling valve, the pump discharge pressure, heat load pressure (pressure downstream of the heat load throttling valve), and pump power were collected. The values of the pressure gauge zeroes were 3.0 psig, 1.5 psig, and 6.0 psig for pump one discharge pressure, pump two discharge pressure, and heat load pressure, respectively. These zeroes were subtracted from the readings taken from the gauges to remove hydrostatic pressures from the readings (as well as account for errors in the gauge zeroes). Table 5.1 summarizes data recorded for ASW pump one.

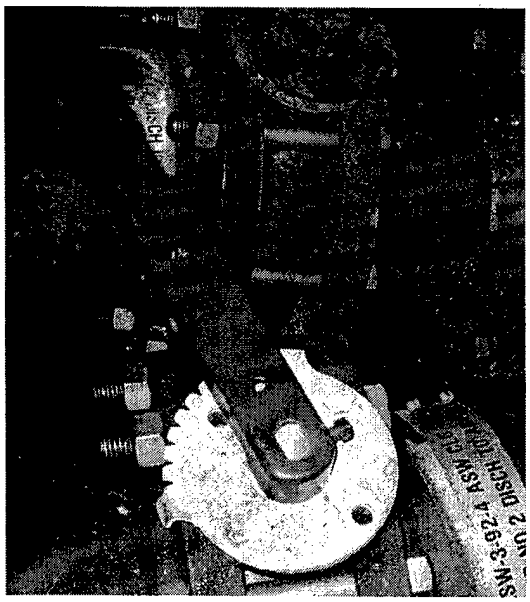

Figure 5.8: ASW System Throttling Valve

Table 5.1: Pressure and Power Data for Throttling of Overboard Valve

Notches Throttled	Pump Outlet Pressure (psig)	Heat Load Pressure (psig)	Pump Power (kW)
1	32	7.75	28.43
2	32.5	8	28.21
3	32.5	8.2	28.18
4	33	9.5	28.01
5	34	12.5	27.87
6	35.5	17.5	27.17
7	41.5	30.5	26.68

Use of Pump Curves to Determine Flow

Pump data was available for the ASW pumps in [16], so the pressure information in Table 5.1 was converted into flow rates. Among the "pump curves" plotted in [16] is the total discharge pressure of the pumps plotted vs. flow rate. Points on this curve were fit to a third-order polynomial in MATLAB to arrive at equation 5.8. In the equation, TDH is total discharge head (the terms "head" and pressure will henceforth be used interchangeably) in feet of water while Q is volumetric flow rate in gpm.

$$TDH = -3.3508 \cdot 10^{-8}Q^3 + 9.9359 \cdot 10^{-6}Q^2 - 4.7494 \cdot 10^{-3}Q + 110.16 \tag{5.8}$$

For each value of discharge head collected onboard the SENECA, the value of flow rate was calculated by solving for the flow rate that would lead to that TDH in equation 5.8. This flow rate however, represents the total flow rate coming out of the pump, not the amount of flow going to the heat loads.

Unfortunately, there are too many variables to calculate the amount of flow going to the heat load branch from only two pressure readings. In order to calculate the amount of flow going to that branch, it would be necessary to know the loss coefficients for each of the three sections of pipe involved (pump outlet to split, split to overboard, and split to heat loads).

The flow rates calculated using equation 5.8 from the collected data is shown in Table 5.2 and Figure 5.9.

Table 5.2: Power and Flow Data for Throttling of Overboard Valve

Notches Throttled	**Pump Power (kW)**	**Total Flow Rate (gpm)**
1	28.43	1167
2	28.21	1157
3	28.18	1157
4	28.01	1147
5	27.87	1127
6	27.17	1096
7	26.68	946

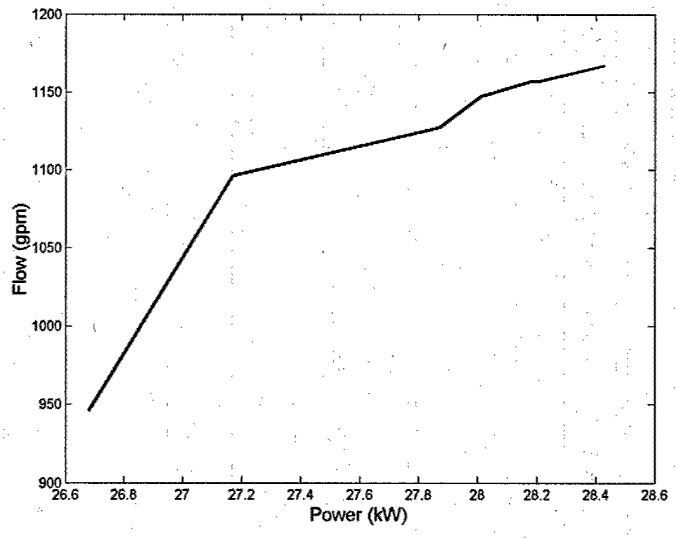

Figure 5.9: Flow vs. Power for ASW Pumps

All of the previous data and discussion were from tests run on pump one. The testing of pump

one followed the expected trend of pressure (at the pump discharge and in the heat load line) increasing as the overboard valve was throttled shut. The data also showed an expected decrease in required power for a decrease in flow rate. The data collected for pump two however, did not follow these trends. An error in testing may be the culprit, although crewmembers onboard the SENECA also expressed very little confidence in the accuracy of pressure gauges in the system. Performing these tests again should be a high priority in future ASW system tests to validate the data collected for pump one.

Verification of Results using the Fluid Test System

A similar set of tests was conducted for the fluid test system. The system was operated with water flowing through the "aircooler" and straight branches while power data was collected. As on the SENECA, the straight branch that returns water directly to the water reservoir was throttled to various levels. Unlike the ASW system onboard the SENECA, the valves involved are globe valves, so a restriction of fluid flow only occurs when the valves are nearly shut (there are 9 turns from fully open to fully shut). Unfortunately, there are no pressure gauges in the system, so a determination of flow could not be made. Table 5.3 shows the results of these tests.

Table 5.3: Power Data for Throttling of Straight Return Valve in Fluid Test System

Turns Throttled	Pump Power (W)
0	785.5
7	778.9
7.5	773.5
8	769.3
8.55	755.5
9	698.5

The table indicates a trend consistent with data collected from the SENECA. There is clearly a decrease in power required to run the pump as more flow is sent through the "aircooler" branch.

5.4.2 Prediction of Inlet Strainer Clogging

Simulated Clogging in ASW System

In addition to a change in head loss at the outlet of the ASW pumps being reflected in pump power, it was expected that a change in head loss at the inlet of the ASW pumps would also be seen in pump power. This change could be used as an indicator for a blocked suction screen or clogged inlet strainer.

To simulate clogs in the inlet strainers of the ASW pumps onboard the SENECA, the strainer isolation valves were throttled to the 3/4 shut position with the pumps off. The pumps were each started in this condition and the power data collected. In each case, there was a marked decrease in the power level drawn by each of the pumps. An example of a pump start with the inlet throttled (and a normal start) is shown in Figure 5.10.

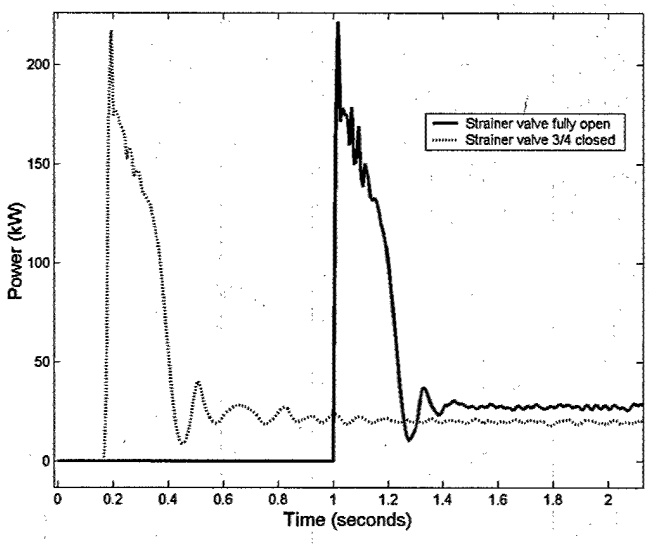

Figure 5.10: Throttled Inlet Starts for ASW System

It is noted from Figure 5.10 that the transients themselves are very similar, it is only the steady state power level which is significantly different. For the pump start on pump one with the strainer isolation valve throttled to 3/4 closed, the average of 1000 points of steady state power data is 19.96 kW. Referring back to Table 5.2 shows that this is nearly 7 kW lower than the lowest normal steady state power level for that pump. This shows that it is possible to distinguish a fault condition like a clogged inlet strainer from the normal range of steady state power levels.

Simulated Clogging in Fluid Test System

As with the ASW system onboard the SENECA, the fluid test system in the laboratory was also started with the pump inlet valve throttled. The pump was started with the pump inlet valve opened only 0.5 turns and the power data collected. An example of a pump start with the inlet throttled is shown in Figure 5.11

As with the pump starts from the ASW system, the transients are similar while the steady state power level is different. For the pump start with the pump inlet valve throttled to 0.5 turns open, the average of 2500 points of steady state power data is 611.3 W. Referring to table 5.3 shows that this is over 80 W lower than the lowest normal steady state power level for the pump. This corroborates the idea that a clogged inlet strainer or other obstruction in the inlet line is distinguishable from the normal range of steady state power levels.

Head Loss at the Inlet of a Pump vs. the Outlet

The natural question now is: "Why should a change to the system at the inlet side of the pump have a more pronounced effect than a change at the outlet side?" After all, both are changes to the amount of flow resistance in the system. Although as stated in [18] the total amount of head loss in a fluid system is the sum of the head loss upstream of the pump and the head loss downstream of the pump, the pump must have a minimum pressure at its inlet to function properly.

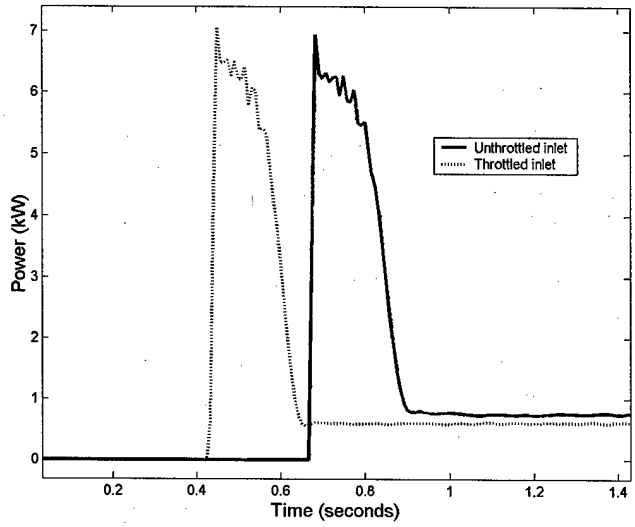

Figure 5.11: Throttled Inlet Starts for Fluid Test System

On the suction side of a pump, low pressures are created. If pressure falls below the vapor pressure of the fluid, bubbles of water vapor are formed in a process called cavitation. For centrifugal pumps, the minimum pressure required at the pump inlet to avoid cavitation is termed the net positive suction head required (NPSHR). If a large pressure drop occurs somewhere upstream of the pump (like that caused by a clogged inlet strainer), the available net positive suction head (NPSHA) may fall below the NPSHR and cavitation occurs. If cavitation occurs in the pump inlet, the hydrodynamic resistance may fall sharply since the average density of the fluid is greatly reduced by the presence of vapor bubbles. This will lead to a sharp decrease in the amount of power required to run the pump.

5.4.3 Prediction of Pump Uncoupling

ASW Pump Uncoupling

The ASW pumps onboard the SENECA do not have a rigid connection between the pump motor and pump impeller. Instead, a flexible coupling is provided between the two. Couplings of this kind are usually used to reduce the vibration transmitted down a shaft or to prevent an over-torque condition. The coupling is a thick rubber ring with teeth on the inside and outside edges. These teeth sit in grooves in cast-iron flanges that are connected to the pump motor and pump impeller shafts. An example of the coupling used to connect the pump motor and pump impeller is shown in Figure 5.12.

Since the coupling is actually composed of two halves, a metal ring is used to hold the two halves together. This ring can slip off during operation, causing the pump motor and impeller to become uncoupled. According to a ship's crewmember "...when it breaks it is not a clean break so when two high spots meet it grabs until they slip by." [19] During the performance of tests onboard the SENECA, a pump start in which the motor and impeller came uncoupled was captured and is presented in Figure 5.13. The second trace appears to be the coupling still making some contact with the flange after the initial uncoupling, exactly as described by the crewmember.

Figure 5.12: ASW Pump Motor-to-Impeller Coupling

Figure 5.13 also includes a start immediately after the uncoupling occurred in which the motor is completely uncoupled from the pump impeller. According to the same crewmember, this is also a possibility if the set screw holding the metal flange to the motor shaft comes loose: "I have not had any problems with the set screws but they have in the past and the shaft will just spin in the coupling." [19]

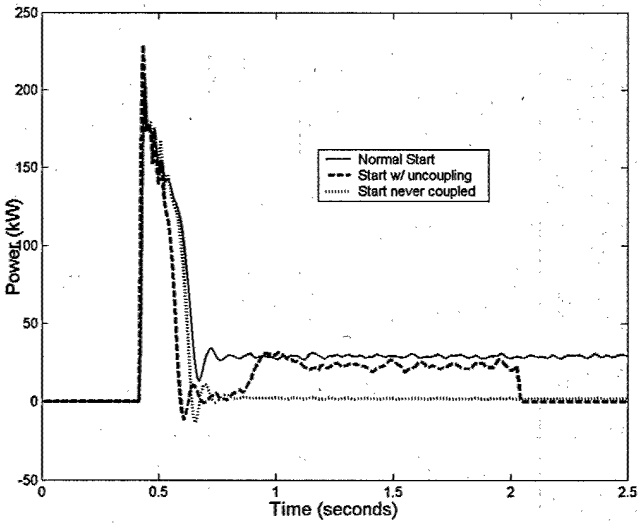

Figure 5.13: ASW Pump Starts for Various Levels of Coupling

Simulated Pump Uncoupling

This uncoupling event was reproduced by the pump start simulation developed earlier. To reproduce the pump uncoupling, the hydrodynamic counter-torque and moment of inertia were both removed at 0.8 seconds into the simulation. At 0.75 seconds into the simulation, they were partially re-inserted. This means that a random number between 1 and 0.9 was used as a multiplier of the moment of inertia and the hydrodynamic counter-torque. A set of simulated starts similar to Figure 5.13 is shown in Figure 5.14.

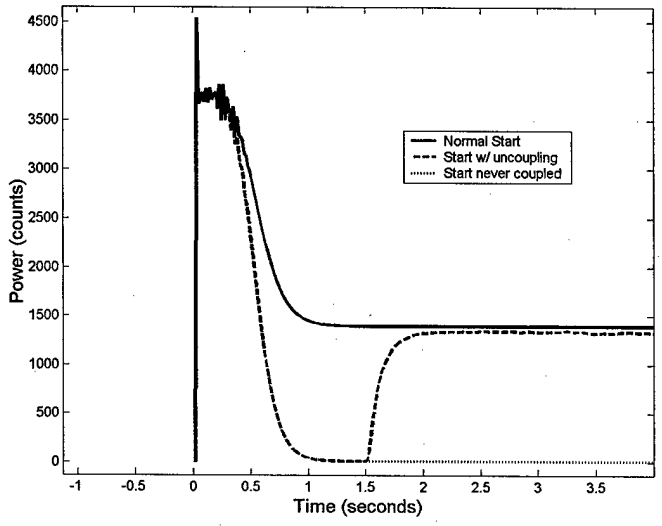

Figure 5.14: Simulated Pump Starts for Various Levels of Coupling

The simulated pump starts produced in Figure 5.14 exhibit the same behavior as the ASW pumps shown earlier in Figure 5.13. It is to note the large decrease in pump power when an uncoupling occurs. This decrease is even larger than would occur for a clogged inlet strainer at the inlet side of the pump, indicating that an automatic data collection system should be able to distinguish between a clogged inlet strainer and the pump impeller becoming uncoupled.

5.5 Power Spectrums as an Indicator of Fluid System Blockage

Although the previous section showed that steady-state power level can be used as a way to determine the status of the fluid system, they were all based on large changes to the head loss in the system. Small changes to an individual component in the fluid system however, can represent much more subtle differences.

After the success of the NILM to detect changes in the fluid system at the inlet or outlet of the pumps, it was decided to see if the NILM could detect changes at the heat loads of the system. To this end, one of the air conditioning (HVAC) units along with two ship service diesel generators (SSDGs) were aligned to the system. The amount of ASW flow to the heat loads was

then throttled in various combinations and the steady-state power level recorded. The results are summarized in Table 5.4. The data is for two minutes of steady-state operation.

Table 5.4: Steady-State Power Data for Throttling to Heat Loads

Condition	Mean Power (kW)	Standard Deviation of Power (kW)
No Throttling	24.43	0.75
SSDGs Throttled	24.37	0.96
HVAC Throttled	24.71	0.86
SSDGs & HVAC Throttled	24.28	0.75

As Table 5.4 indicates, there is a difference in the amount of steady state power level drawn for throttled flow to the various heat loads, but it is not significant compared the standard deviation in the power data. The interpretation of this table is that it is not necessarily possible to see a change in the steady-state power level outside of that power level's noise for a change in the flow level to a heat load.

5.5.1 Fan Data

The first indication that the frequency content of a power signature could contain vital information was from a fluid system that pumped air and not one that pumped water (considering both air and water as fluids; one compressible, the other not). A NILM setup was installed at a large fan that is part of the SENECA's ventilation system. Although the NILM was originally installed to determine if clogged inlet filters could be detected, the shape of the fan's startup transients indicated that there were some oscillations in the power drawn by the fan. An illustration of the fan is shown in Figure 5.15.

One LA 205-S current transducer is monitoring the current to the fan. The resistors used for the voltage measurement, current measurement, and references are 130 Ω, 66.5 Ω, and 56.2 Ω, respectively. Upon initial system installation, the system was calibrated by collecting balanced three-phase power data with a Fluke 39 Powermeter and comparing it to the power counts obtained with the NILM. The resultant scaling factor between real power (1.99 kW) and counts (3099.5) was 0.642 $\frac{Watts}{count}$.

The fan was run with no filters installed, four filters installed, and with two of the filters covered with cardboard (to simulate blockage). The frequency spectrum of power data for the steady-state operation and start transients were then created using a discrete fourier transformation (see [20] for a description of the discrete fourier transformation). These power spectrums are shown in Figures 5.16 and 5.17, respectively.

For the steady state fan runs, the most important difference is between the four filter and blocked filter case. They both show large peaks at 17.5 Hz, but the case in which filters are blocked shows a peak approximately 25% higher than the unblocked case. For the fan starts, there is an oscillation band in the power spectrum which decreases in frequency as more blockage is placed at the inlet of the fan. The band can be seen between 11 and 17 Hz for the no filter case, between 7 and 10 Hz for the four filter case and between 3 and 6 Hz for the case with two

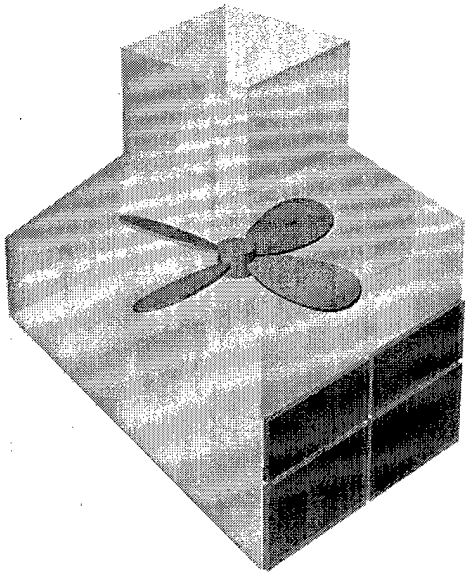

Figure 5.15: SENECA HVAC Fan

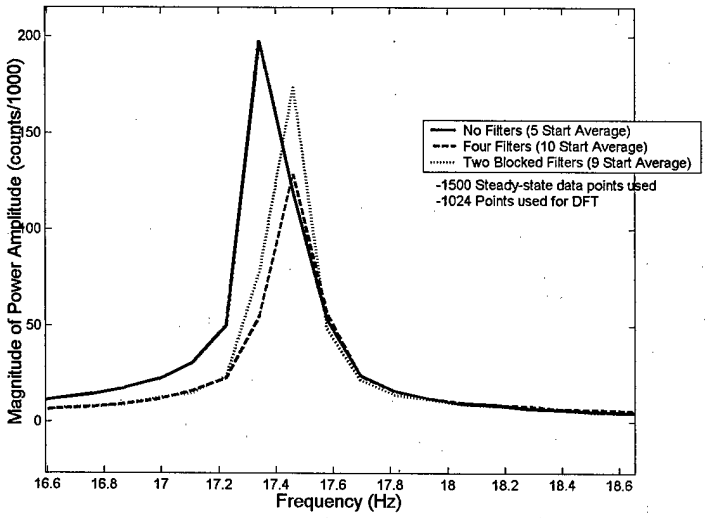

Figure 5.16: Steady State Power Spectrum for Various Filter Conditions

filters blocked. These data were the first indication that blockage in a fluid system could be seen in a power spectrum.

5.5.2 SENECA Testing

Since is was now known that blockage could affect the power spectrum, data from the SENECA was taken and analyzed to determine if blockage could be seen in the power spectrums of the

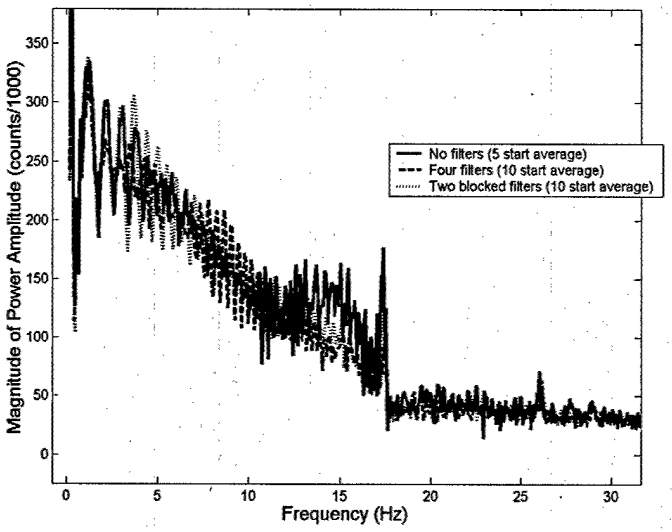

Figure 5.17: Transient Power Spectrum for Various Filter Conditions

ASW pumps. Blockage in heat exchangers is an actual problem that is known to occur in the ASW system so was deemed a high priority. Many crewmembers reported that mussels would grow in the endbells of heat exchangers while the ship was in cold water, then detach themselves in warmer waters, causing a reduction of flow through the heat exchangers.

The first step was to determine the difference between the ASW system's power spectrum with and without mussels present. Underway data was found for number one SSDG with mussels present in the endbell of the lube oil cooler. A power spectrum was developed for this data and compared to a power spectrum for the time period two hours later (after the mussels had been removed). These two power spectrums are shown in Figure 5.18.

There are two key observations made from Figure 5.18:

1. There is 10 Hz peak in power that appears to be characteristic of the ASW system. This peak may be due to resonant effects anywhere in the system, including close to the pump itself.

2. This peak changes dramatically for blockage in the number one SSDG lube oil cooler. The difference in the two peaks is nearly a factor of three. The ship's logs only state that temperature was rising in number one SSDG and that it was subsequently shut down at 0828. There is no indication of rising temperatures anywhere else in the ASW system, so it assumed that the change is due only to blockage in the number one SSDG lube oil cooler.

In order to verify the validity of the power spectrum with blockage present, tests were run with flow into number one SSDG lube oil cooler throttled. The throttled and unthrottled results are shown in Figure 5.19.

It should be noted that the peak at exactly 10 Hz shows the same reduction in amplitude as in the blocked case. However, there are peaks to the sides of 10 Hz that show a much higher amplitude for the throttled case than for the unthrottled case. This phenomenon was not seen when the lube oil cooler was actually clogged with mussels. Clearly, throttling an inlet valve to

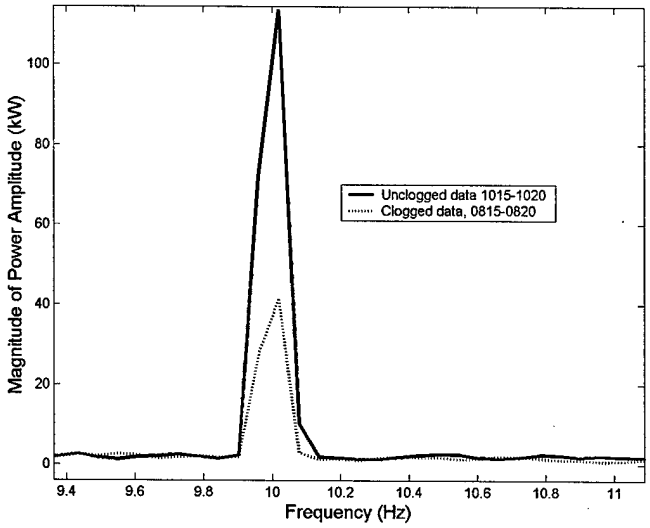

Figure 5.18: Power Spectrum for Blocked SSDG Lube Oil Cooler

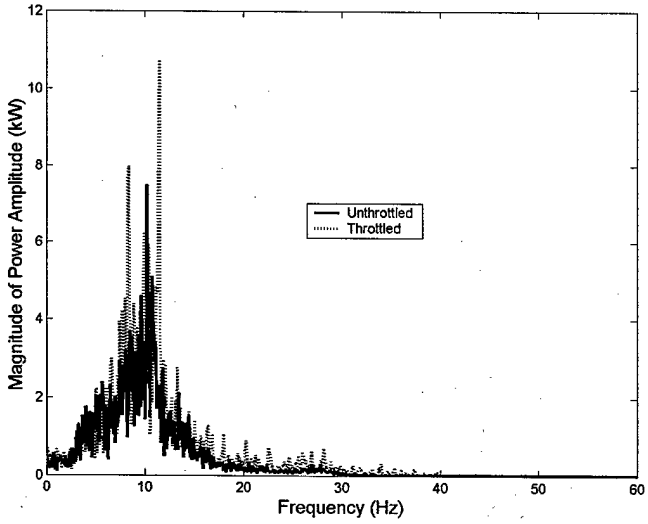

Figure 5.19: Power Spectrum for Throttled SSDG Lube Oil Cooler

a heat exchanger is not the same as blocking some of the individual heat exchanger tubes. The difference is that in the former case, there is lessened flow to all tubes while in the latter case, the blocked tubes have reduction in flow while the unblocked tubes have an *increase* in flow (to maintain the same volumetric flow rate).

Ideally, testing would occur with obstructions inserted into the lube oil heat exchanger. Since testing of this nature is not feasible on an operational Coast Guard Cutter, the fluid test system was again utilized for more in-depth experimentation.

5.5.3 Power Spectrum and Vibration Experiments using the Fluid Test System

Unlike tests conducted onboard the SENECA, tests conducted on the fluid test system also involved the collection of vibration data. It was felt that the oscillations in the pump power might be caused by pressure waves being transmitted back to the pump impeller. If these pressure waves transmitted even some of their energy into the piping, then it should be detected externally.

To this end, vibration transducers were connected at the inlet side of the fluid test system HX. Each vibration transducer consists of a magnet which is able to vibrate inside a loop of wire, causing a voltage to be ouput. The vibration transducers were able to detect vibration along two perpendicular axes by being attached to the inlet piping of the HX as shown in Figure 5.20. The convention used was that of cylindrical coordinates in which the "Z" direction is along the axis of the cylinder while the "R" direction is outward from the axis of the cylinder.

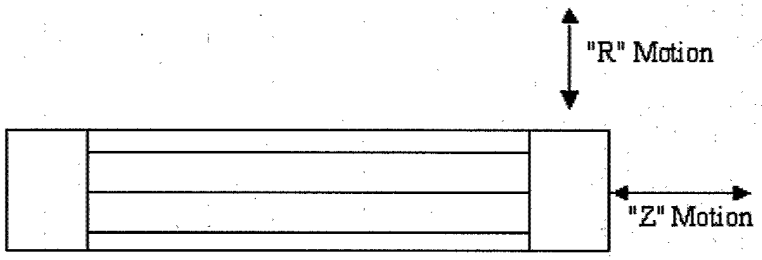

Figure 5.20: Heat Exchanger Vibrometer Degrees of Freedom

Throttling Data

The first experiment conducted on the fluid test system was with the inlet valve to the HX throttled to only one turn open. This data was taken to validate the throttling data taken onboard the SENECA. The spectrums for power, R direction vibration and Z direction vibration are shown in Figures 5.21, 5.22, and 5.23, respectively.

Just as on the SENECA, the power spectrum for throttled flow into the fluid test system HX shows higher amplitudes for the throttled condition. The vibration shows lower amplitudes in both the R and Z directions, due to the decrease in total flow through the heat exchanger.

Clogging Data

Unlike throttling the total flow through the HX with the use of a single valve, there are many different ways that blocking of tubes can occur. Along with the unblocked condition, data were taken for three different types of the blocked-tube condition. These different modes of blocking are illustrated in Figure 5.24.

For each type of clog, one minute of steady state power and vibration data were taken along with a measurement of the pump's impeller speed. The pump impeller speed was measured by painting a small white dot on the rotor of the pump and then using a laser tachometer to measure rpm. This process was repeated five times for each of the clogged conditions, the Frequency spectrum for that run of data was created (for both power and vibration), and the spectrums for each of the five runs were averaged. The average impeller speed was 3520 rpm with the variation

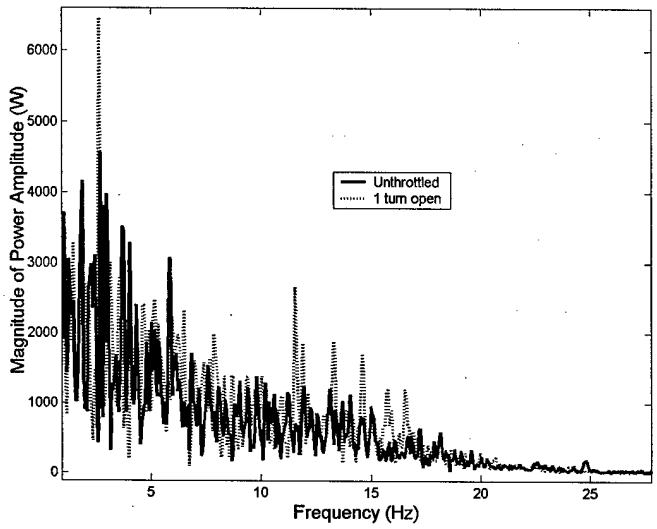

Figure 5.21: Power Spectrum for Throttled Flow to Fluid Test System Heat Exchanger

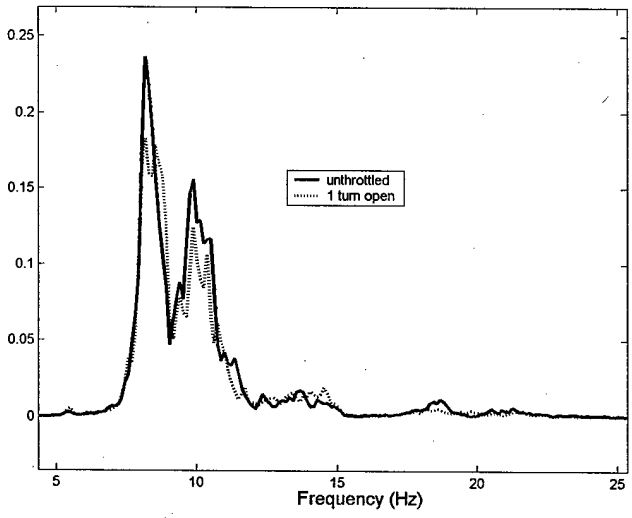

Figure 5.22: R-Motion Spectrum for Throttled Flow to Fluid Test System Heat Exchanger

in impeller speed within the error of the tachometer ($\pm$ 1 rpm). The frequency spectrum for pump power is shown in Figure 5.25.

Although not necessarily obvious from Figure 5.25, the important frequency for the power spectrum is at 2.5 Hz. It is important because every test case has a large spike at that frequency. The frequency spectrum for vibration in the R direction is shown in Figure 5.26.

Figure 5.26 shows two large peaks in frequency, one at 58.73 Hz and the other in the vicinity of 8.5 Hz. Since the pump rotational speed of 3520 rpm corresponds to a frequency of 58.67

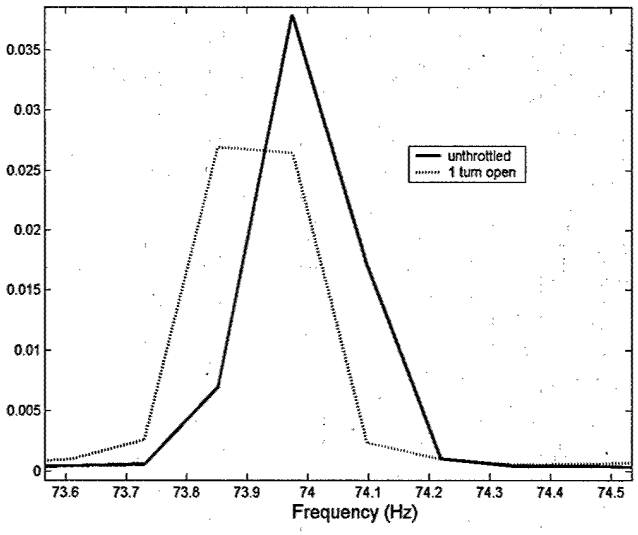

Figure 5.23: Z-Motion Spectrum for Throttled Flow to Fluid Test System Heat Exchanger

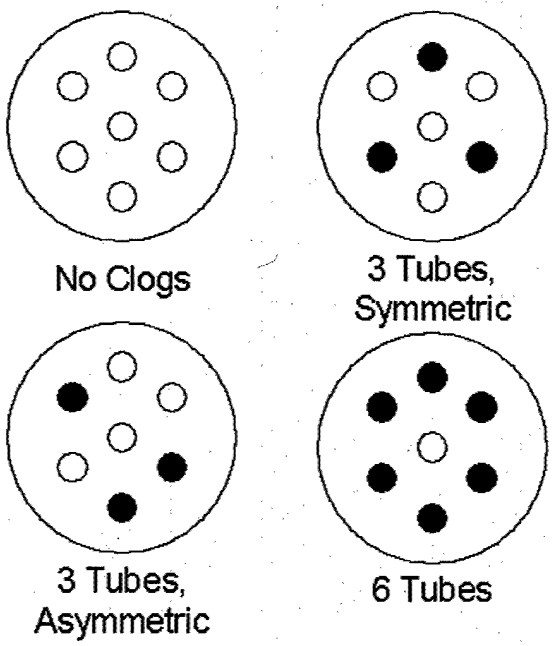

Figure 5.24: Fluid Test System HX Clog Types

Hz, the peak at 58.73 Hz is just mechanical vibration transmitted through the piping due to the rotation of the pump impeller and not due to fluid moving through the pipe. The peaks at 58.73 Hz and 8.5 Hz are shown in Figures 5.27 and 5.28, respectively.

There are two interesting phenomena to note in Figure 5.28. First, for the cases where there

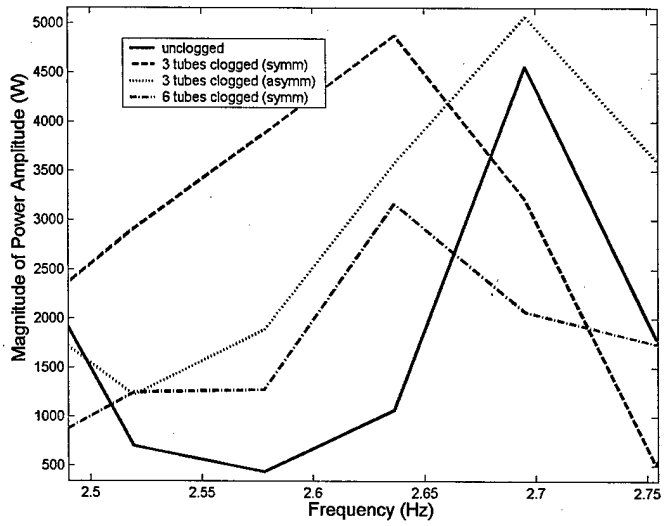

Figure 5.25: Power Spectrum for Clogged Flow to Fluid Test System Heat Exchanger

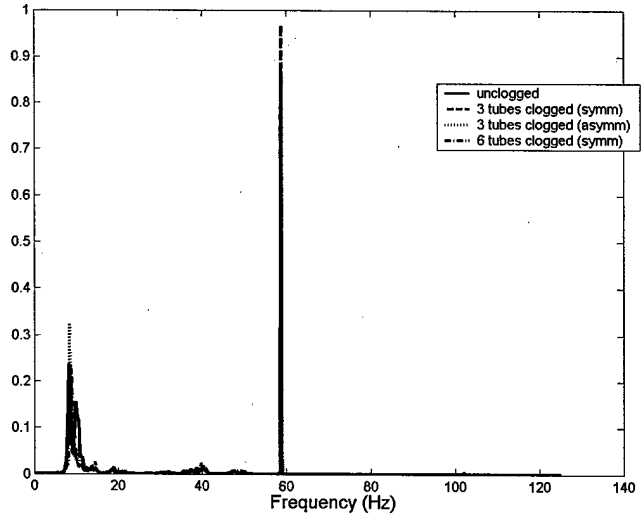

Figure 5.26: R-Motion Spectrum for Clogged Flow to Fluid Test System Heat Exchanger

is symmetric flow through the HX, frequency peaks do not get larger, but they do shift upwards in frequency as the amount of clogging increases. Secondly, the only frequency peak which is larger than the others is for the case where three tubes are clogged asymmetrically. Compare these observations with Figure 5.25. Note that in Figure 5.25, the frequency peak in the vicinity of 2.5 Hz for the unclogged case and the case with three tubes clogged asymmetrically are at the same frequency. As with vibration in the R direction, the frequency peak is higher when there is asymmetric blockage. Looking farther back to Figure 5.16, note that when two filters are blocked,

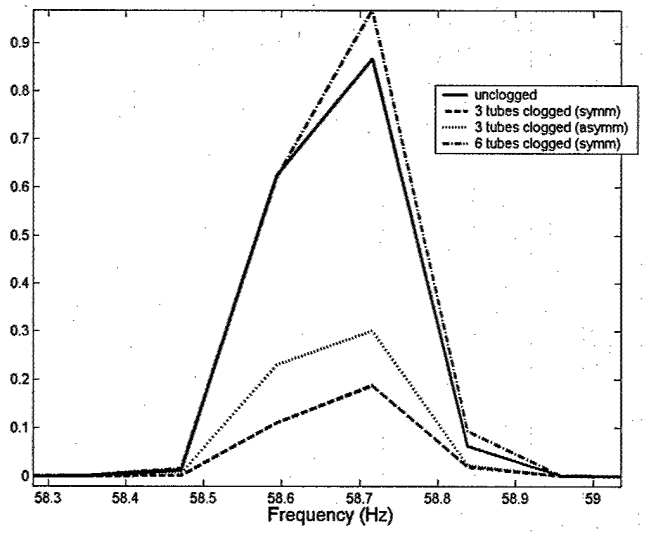

Figure 5.27: 58.73 Hz Peaks in R-Direction for Clogged Flow to Fluid Test System Heat Exchanger

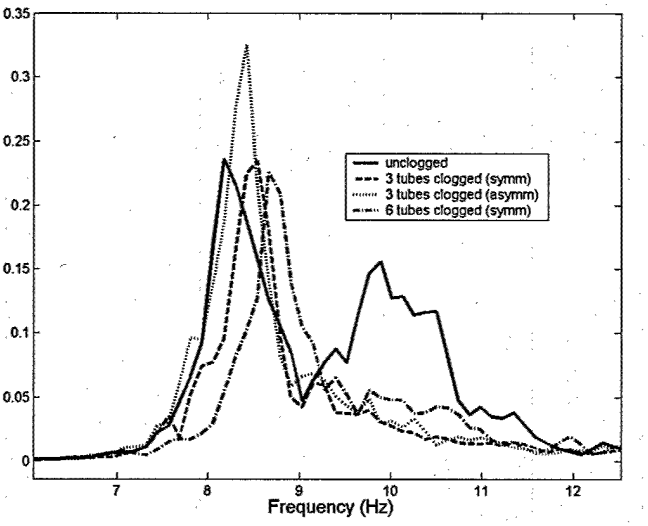

Figure 5.28: 8.5 Hz Peaks in R-Direction for Clogged Flow to Fluid Test System Heat Exchanger

there is a higher frequency peak (at the same frequency) than when the fan filters are unblocked. The blocked filters in the SENECA HVAC fan case also represent asymmetric blockage because the top two filters were blocked while the bottom two filters were left unblocked.

For vibration of the fluid test system in the Z direction, Figures 5.29 and 5.30 show the frequency spectrum for various blockage conditions. The largest frequency peak is at approximateley

74 Hz with two side bands. The peaks to either side of 74 Hz are identified as sidebands because they are spaced evenly around 74 Hz.

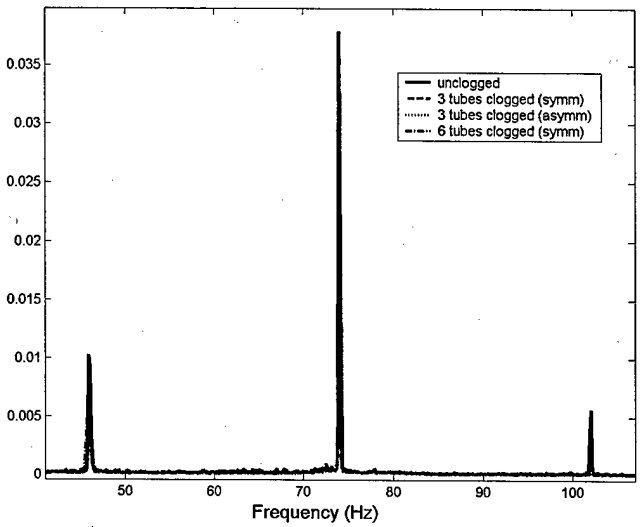

Figure 5.29: Z-Motion Spectrum for Clogged Flow to Fluid Test System Heat Exchanger

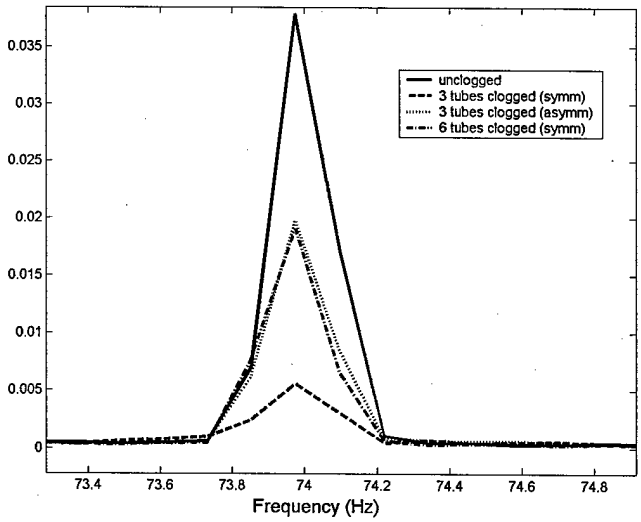

Figure 5.30: 73.88 Hz Peaks in Z-Direction for Clogged Flow to Fluid Test System Heat Exchanger

All three of the peaks in Figure 5.29 show the same trend, so the peak presented in Figure 5.30 at 73.88 Hz is discussed. The Z direction vibration does not follow the same trends as the R direction vibration or the power oscillations. The Z direction vibration shows the highest peak for the unclogged condition, which is not true for the other two spectrums. Vibration in the Z direction should probably not be used as a predictor of the power spectrums because it was noted during testing that the thrust of water against the side of the water reservoir in the fluid test system was causing vibration in the Z direction of the HX.

To summarize the trends in the the various frequeny spectrums, Table 5.5 provides rankings of the frequency peaks for the power, R direction vibration, and Z direction vibration spectrums. The highest peak is given a rank of one while the lowest peak is given a rank of four. Shifts in frequency are also indicated where applicable.

Table 5.5: Frequency Peak Rankings for Various Fluid Test System HX Clogs

Clog	**Power**	**R**	**R (58.73 Hz)**	**Z (73.88 Hz)**
None	3 (2.7 Hz)	2 (8.1 Hz)	2	1
3 (symm)	2 (2.63 Hz)	2 (8.5 Hz)	4	3
3 (asymm)	1 (2.7 Hz)	1 (8.3 Hz)	3	2 (tie)
6	4 (2.63 Hz)	2 (8.7 Hz)	1	2 (tie)

It is noted from Table 5.5 that there is no clear trend in the spectrum of frequencies that corresponds to the clog severity. It is noted however, that the situation which is most severe shows a large decrease in the frequency peak in the vicinity of 2.5 Hz. If 2.5 Hz is the frequency that is an indicator of HX clogging, a decrease in the peak at that frequency for a highly clogged HX is consistent with the results from the SENECA. It is also noted from Table 5.5 that the upward *shift* in frequency for vibration in the R direction (in the vicinity of 8.5 Hz) may be the best indicator of clogging.

5.6 Chapter Summary

Large changes in head loss in a fluid system are readily apparent in the steady state power levels of the pumps which provide flow through the system. It is possible to distinguish between large head losses at the pump inlet and the pump outlet.

Subtle changes in the fluid system at individual components are much harder to detect. It is possible that each component in the fluid system has a unique signature in the spectrum of frequencies over which power is transmitted. It remains to be seen how changes to individual fluid system components affect these frequency signatures. Specifically, a more detailed understanding of the fluid mechanics of clogged heat exchangers must be developed.

Chapter 6

Hydraulic System Results

6.1 Introduction

Like seawater cooling systems, hydraulic systems are common across a wide range of ship types and sizes. One of the most important type of hydraulic system found onboard ships is the steering system. Since the steering system (in conjunction with the main engines) provides the ship its maneuverability, the status of its functionality must be known at all times. Monitoring the steering systems onboard the USCGC SENECA and the ONR YP provided on opportunity to determine if the NILM could detect any degradation of the system's performance. Additionally, it was hoped that the NILM could provide a backup indication of system parameters (e.g. rudder angle) with the hope of developing a NILM-based autopilot in the future.

6.2 SENECA Steering System

The steering system onboard the SENECA consists of two 30 hp pumps drawing hydraulic fluid from a common reservoir to pressure a common header. Rudder actuation is accomplished through two 4 in. hydraulic rams (one for each rudder stock). Additionally, parallel rudder motion is accomplished through the use of a large tie rod which connects the two rudder stocks. Figure 6.1 shows a schematic representation of the SENECA's steering system while Figure 6.2 shows one of the rudder hydraulic rams and the connecting tie rod.

Different system configurations are achieved by repositioning valves. The valve positions requird for these different configurations is shown in Figure 6.3. The diagram is a copy of the actual plate on the side of the steering system itself.

The NILM installation for the SENECA system uses one voltage transducer and two current transducers to monitor the two hydraulic pumps that pressurize the system. Since there is no one panel that supplies both of the pumps (for reliability), one LA-205 current transducer had to be placed in each pump controller and the output combined at the NILM box. The resistors used for the voltage measurement, current measurement, and references are 130 Ω, 15 Ω, and 56.2 Ω, respectively. Upon initial system installation, the system was calibrated by collecting balanced three-phase power data for pump one with a Fluke 39 Powermeter and comparing it to the power counts obtained with the NILM. The resultant scaling factor between real power (3.6 kW) and counts (570.11) was 6.31 $\frac{Watts}{count}$.

It should be noted that the steering system onboard the SENECA is the only NILM installation discussed in this thesis that did not have its own dedicated computer. Test data were taken with

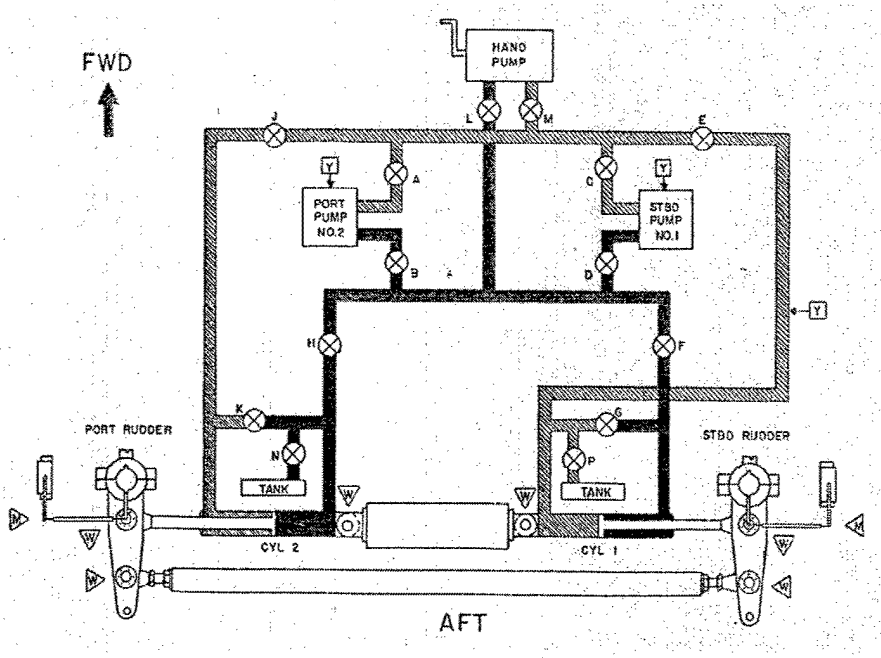

Figure 6.1: SENECA Steering System Schematic

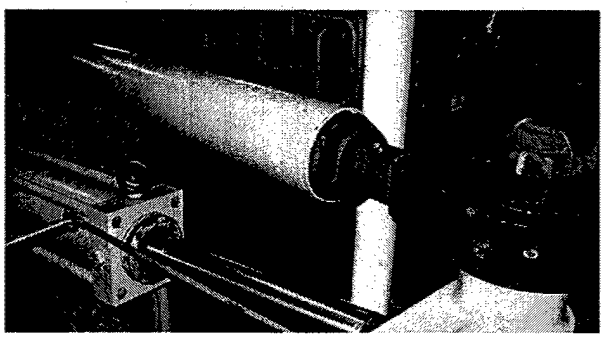

Figure 6.2: SENECA Steering System Rudder Ram and Tie Rod

a computer that was connected to the NILM box only at the time of testing. Two different test sessions used two different computers. It was discovered that the number of counts produced by the second computer for the same pump power was different than for the first computer. The resultant scaling factor between real power (3.6 kW) and counts (1033.3) was 3.48 $\frac{Watts}{count}$ for the second computer.

The first scaling factor was used for data taken in October, 2003 while the second scaling factor was used for data taken in 2004.

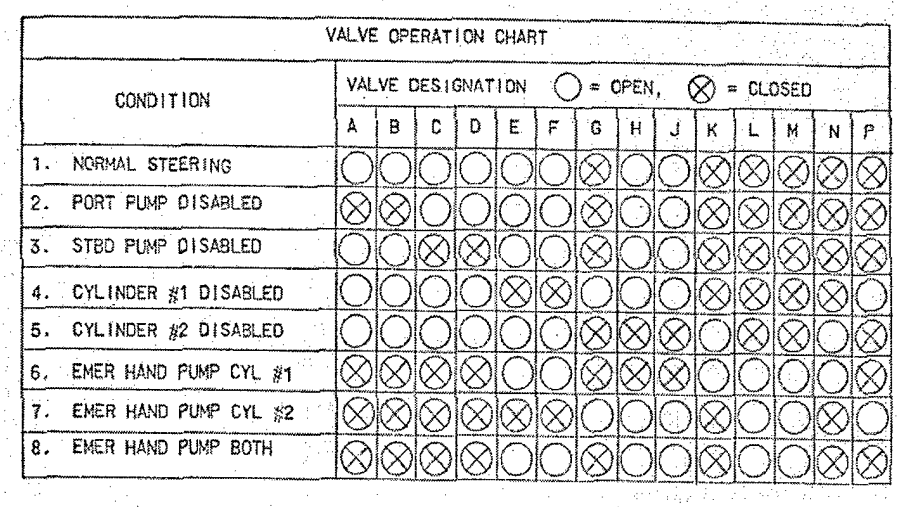

Figure 6.3: SENECA Steering System Valve Lineups

6.2.1 In-Port Rudder Transients Before and After a Repaired Cylinder

The rudder transients that were conducted consisted of "fishtailing" the rudder back and forth through various angles. The rudder was first moved from 0 degrees to left 5 degrees. After a brief pause, the rudder was moved back to 0 degrees. After another brief pause, the rudder was moved to right 5 degrees. The rudder was then moved back to 0 degrees following another brief pause. This process was continued for 10 degrees, 15 degrees, etc. up to 25 degrees of rudder deflection. The power data for these transients are shown in Figure 6.4. Notice that the transients are longer as the rudder is deflected to higher angles.

The data contained in Figure 6.4 was one of the first sets of data taken for the steering system. After collecting this data, it was desired to disable one of the rudder ramss to determine how the transients would look for rudder motion in which only one of the rams was providing power. Due to an incorrect valve lineup, the return path for the hydraulic ram that had been disabled (number one) was closed, so the cylinder began leaking hydraulic fluid. It was later discovered that an O-ring had become dislogded from the excessive pressure in the cylinder. The cylinder and ram were removed for repair and no further testing was accomplished before the ship went out to sea.

The power data in Figure 6.4 show a variation in the amount of power drawn when the rudders are moving left or right. This is due to a difference in the two cylinders. When these data were collected, it was noted that cylinder number one would shake when the ram was retracting into its cylinder, which corresponds to a left turn. The transients that correspond to the rudders deflecting left show a lower power value than the transients that correspond to the rudders deflecting right.

Following the SENECA's return to port, a new round of testing was begun with cylinder number one repaired and reinstalled in the system. The first test was the same "fishtailing" of the rudders that had been done before. The power data for these transients with the repaired cylinder are shown in Figure 6.4

The power data in Figure 6.5 do not show a variation in the amount of power drawn when the rudders are moving left or right. There was clearly a fault present in number one cylinder even before the overpressure condition caused the O-ring to become dislodged. Whatever fault

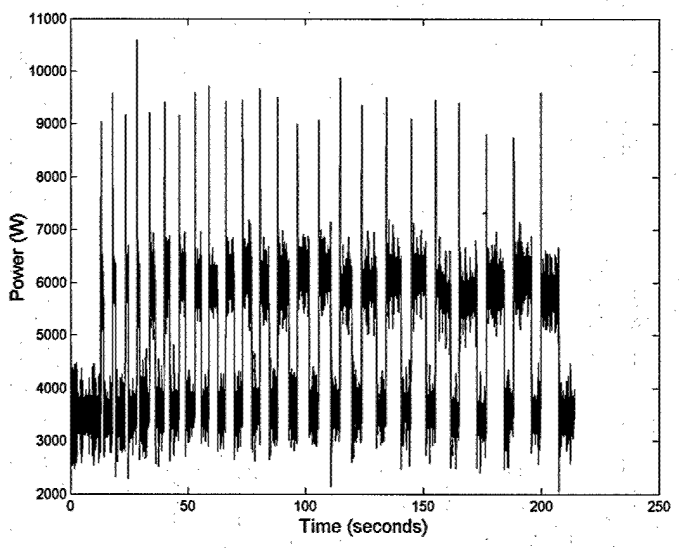

Figure 6.4: SENECA Rudder Transients, Both Rams, Pump 1 Running

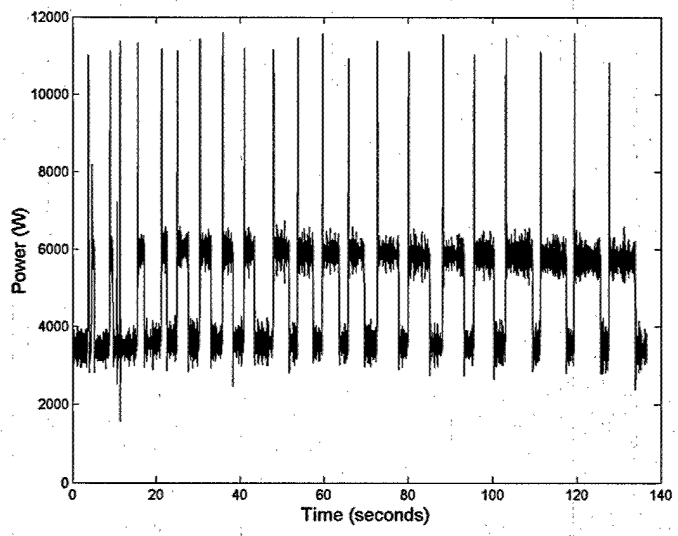

Figure 6.5: SENECA Rudder Transients, Both Rams, Pump 1 Running, After Repairs

was present in the cyinder might have actually been the cause of the dislodged O-ring. This is corroborated by the failure of the system's relief valve (which several people heard lift) to protect the cylinder.

6.2.2 Rudder Transients with Disabled Cylinders

The same rudder "fishtailing" that was conducted before was again conducted to determine if there was a difference in power transients when only one ram was functioning instead of both of them. The collected power data are shown in Figures 6.6 and 6.7.

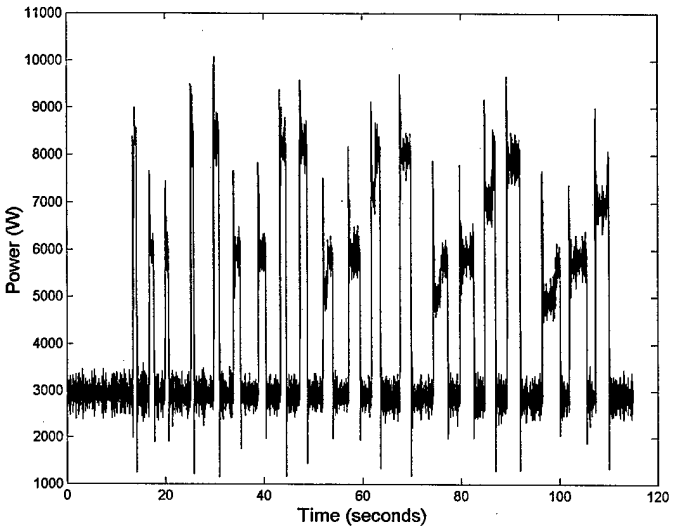

Figure 6.6: SENECA Rudder Transients, Ram 1 only

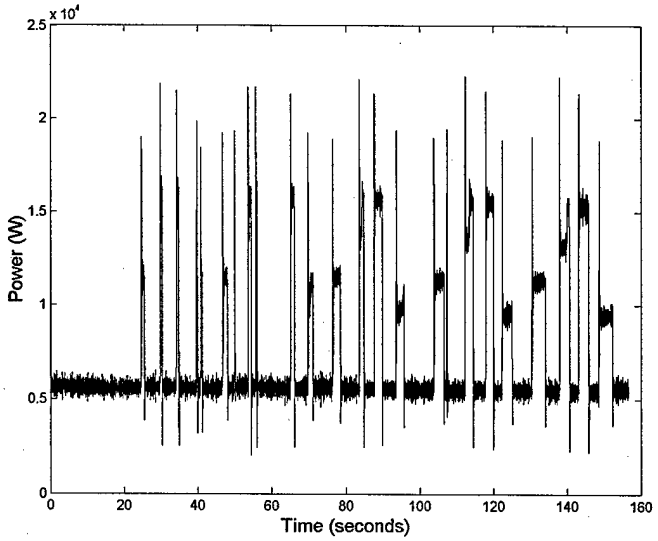

Figure 6.7: SENECA Rudder Transients, Ram 2 only

Figures 6.6 and 6.7 show that when there is only one powered ram, there is a difference between the power drawn by the hydraulic pumps for left rudder movement and right rudder movement.

If ram one is powered, more power is drawn for a left turn, whereas more power is drawn for a right turn if ram two is powered. This difference can be explained by the difference in head loss experienced at one side of the ram vs. the other.

According to [1], the amount of head loss experienced by a fluid moving at some velocity is given by equation 6.1 where h_L is the head loss, K_L is the head loss coefficient, V is the fluid velocity, and g is acceleration due to gravity. The head loss coefficient in this equation is usually only a function of the piping geometry under consideration.

$$h_L = K_L \frac{V^2}{2g} \tag{6.1}$$

For the purposes of this analysis, an expansion is defined as when a fluid moves from a pipe of small cross-sectional area to a pipe of larger cross-sectional area. Likewise, a contraction is when a fluid moves from a pipe of large cross-sectional area to a pipe of smaller cross-sectional area. For a cross-sectional area ratio of $\frac{A_2}{A_1}$ where A_1 is the cross-sectional area of the large pipe and A_2 is the cross-sectional area of the small pipe, the head loss coefficients for the cases of contraction and expansion are given in Figure 6.8.

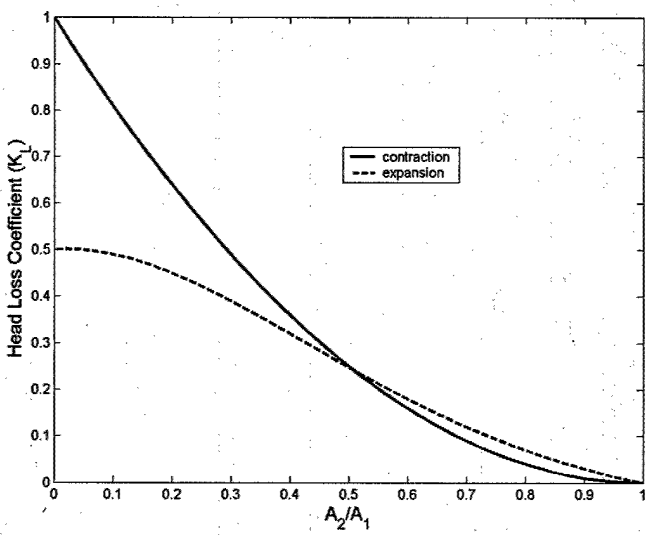

Figure 6.8: Head Loss Coefficients for Expansion and Contraction

The steering system on the SENECA is composed of 4 in. cylinders and 1 in. hydraulic lines. Therefore, operation of the steering system consists of fluid expansions and contractions to and from the hydraulic cylinders. When both of the rams are powered, the head losses due to expansion and contraction are equal for left or right rudder deflection. If only one ram is powered, however, the head losses are different for left and right rudder deflections.

It is clear that the side of the hydraulic cylinder which does not contain the ram (e.g. the left side of cylinder one in Figure 6.1) has a larger cross-sectional area through which fluid can move. For the steering system onboard the SENECA, the $\frac{A_2}{A_1}$ ratio for the side of the cylinder which does not contain the ram and the hydraulic piping is 0.25. The estimated $\frac{A_2}{A_1}$ ratio for the side of the cylinder which contains the ram and the hydraulic piping is 0.5. Using these area ratios, it is possible to generate a table for the head loss coefficients in the two hydraulic cylinders

for left and right rudder deflection for only one powered cylinder. Table 6.1 gives the head loss coefficients from Figure 6.8 for left and right rudder deflection with only cylinder one powered. Only the portion of each cylinder that acts as a load on the system is considered.

Table 6.1: Hydraulic Head Loss Coefficients for Left and Right Rudder Motion w/ Ram 1 Powered

	Left Deflection	**Right Deflection**
Cyl. 1 Contraction	0.425	0.375
Cyl. 2 Expansion	0.5625	0.25
Cyl. 2 Contraction	0.375	0.425
Total	1.3625	1.05

Table 6.1 indicates that the total head loss coefficient for left rudder deflection is higher than for right rudder deflection when only cylinder one is powered. This means that there is a larger pressure drop for left rudder deflections, so the hydraulic pumps must consume more power to maintain pressure in the system, exactly as is shown in Figure 6.6.

For the situation in which cylinder two is powered, the entries in Table 6.1 are reversed, and right rudder deflection requires a higher amount of hydraulic pump power. This is the situation shown in Figure 6.7.

6.3 ONR YP Steering System

In addition to the extensive testing that was performed on the USCGC SENECA, tests were also performed on a yard patrol craft operated by the Office of Naval Research (referred to as the "ONR YP"). The steering system onboard the ONR YP consists of two 3 hp pumps drawing hydraulic fluid from a common reservoir to pressure a common header. Unlike the steering system on the SENECA, rudder actuation is accomplished through only one hydraulic ram. The single hydraulic ram moves in two different directions to accomplish left and right rudder deflections. The hydraulic ram moves the starboard rudder directly. Parallel motion of the port rudder is achieved through the use of a tie rod which connects the port an starboard rudder stocks. Figures 6.9 shows a schematic of the system while Figures 6.10 and 6.11 shows one of the hydraulic pumps that pressurizes the system and the system tie rod, respectively.

The NILM installation for the ONR YP steering system uses one voltage transducer and two current transducers to monitor the two hydraulic pumps that pressurize the system. Since there is no one panel that supplies both of the pumps (for reliability), one LA-55 current transducer had to be placed in each pump controller and the output combined at the NILM box. The resistors used for the voltage measurement, current measurement, and references are 47 Ω, 95 Ω, and 47 Ω, respectively. Upon initial system installation, the system was calibrated by collecting balanced three-phase power data with a Fluke 39 Powermeter and comparing it to the power counts obtained with the NILM. The resultant scaling factor between real power (1.19 kW) and counts (3938.7) was 0.3021 $\frac{Watts}{count}$.

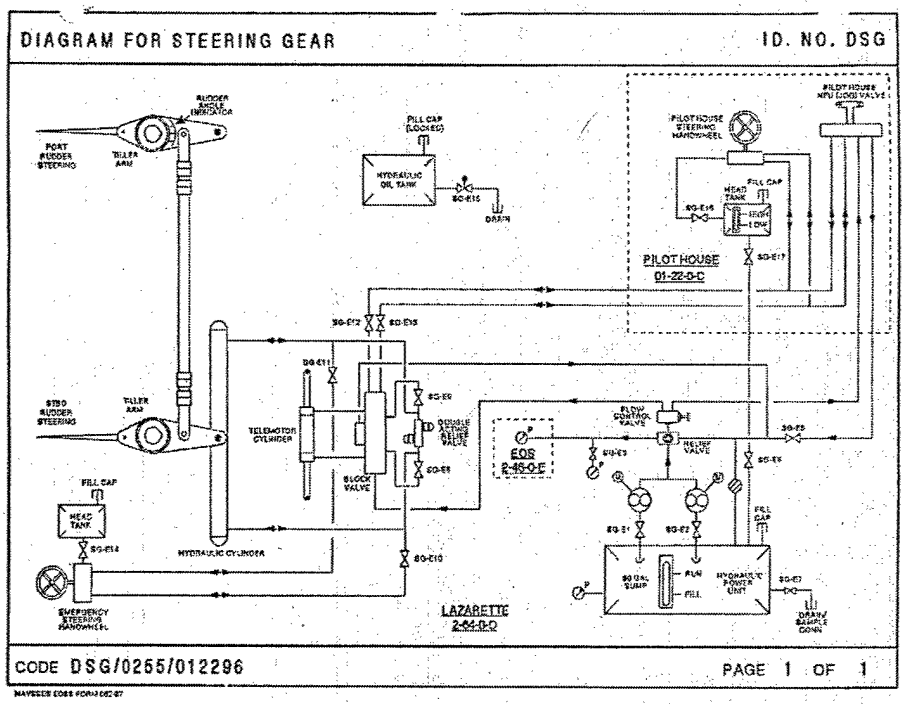

Figure 6.9: ONR YP Steering System Schematic

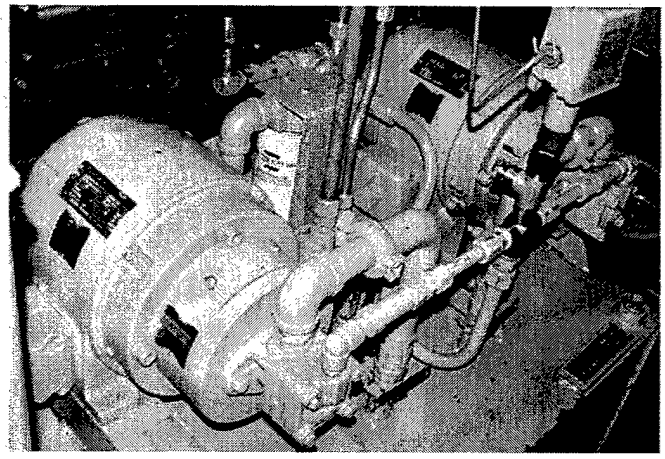

Figure 6.10: ONR YP Steering System Hydraulic Pumps

6.3.1 Normal In-Port Rudder Transients

The rudder transients that were conducted consisted of "fishtailing" the rudder back and forth through various angles, just as on the SENECA. The power data for these transients are shown in Figure 6.12.

It is important to note in Figure 6.12 that the power data is not nearly as clear as for the rudder transients collected onboard the SENECA. Not only is there a larger variation in the steady state power level between power levels, but the rudder transients themselves do not show

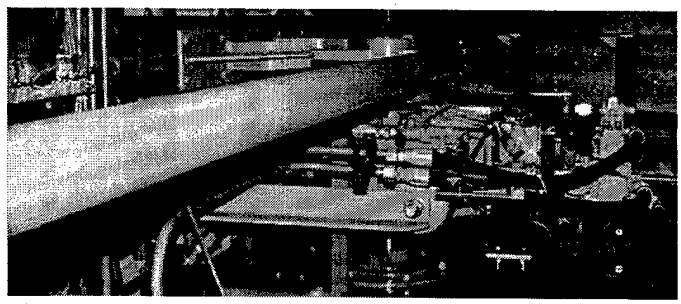

Figure 6.11: ONR YP Steering System Tie Rod

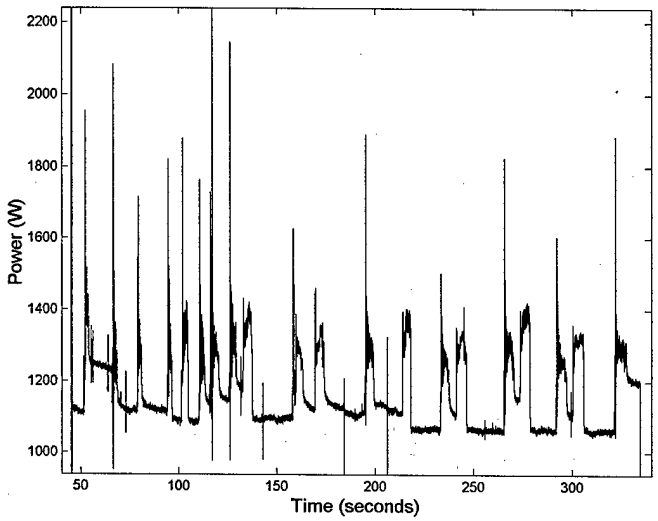

Figure 6.12: ONR YP Rudder Transients

the flat plateau that the rudder transients for the SENECA did. This is not necessarily bad news however, the differences in power transients can actually be used to determine the nature of rudder motion. Figure 6.13 shows the last three rudder transients from Figure 6.12.

In Figure 6.13, the rudder is moving from left 25 degrees to 0 degrees, from 0 degrees to right 25 degrees, and finally from right 25 degrees back to 0 degrees. Figure 6.13 clearly shows that the rudder transient for deflection *towards* 0 degrees has a much larger initial power peak than rudder motion *away from* 0 degrees. Ultimately this information could be used by an autopilot (along w/ recognition in the difference between left and right rudder deflection) to determine rudder position.

6.3.2 Faulted In-Port Rudder Transients

In addition to collecting rudder transients with both rudders being moved by the single hydraulic ram, transients were also collected with the tie rod disconnected so that the hydraulic ram was moving only the starboard rudder. The same "fishtailing" transients were collected as for when

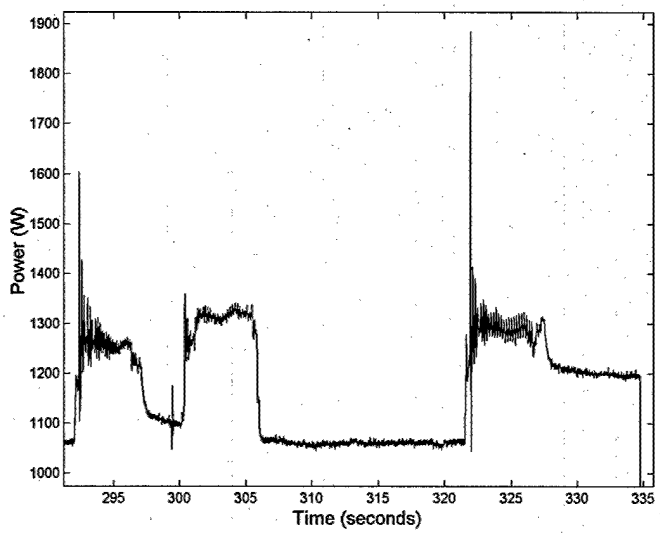

Figure 6.13: Larger View of ONR YP Rudder Transients

the tie rod was connected. The power data for these transients are shown in Figure 6.14.

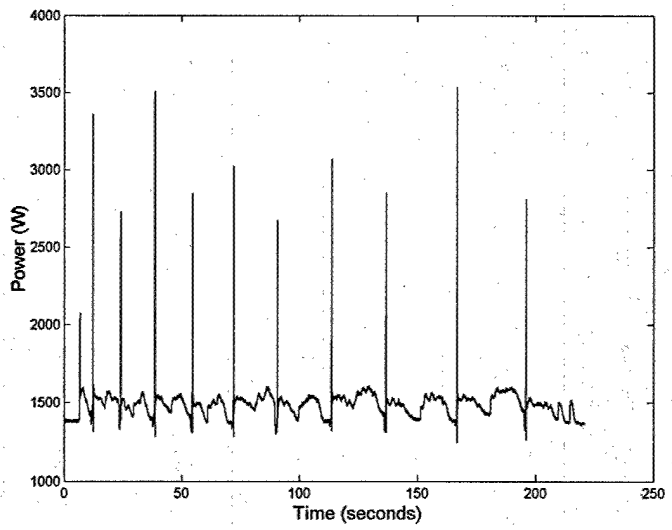

Figure 6.14: ONR YP Rudder Transients, Starboard Rudder Only

It should noted from a comparison of Figures 6.12 and 6.14 that the power levels for the tie rod disconnected are higher than for the tie rod connected. It might at first seem that this higher power level might be a good indicator of the tie rod being disconnected. The discrepancy is that the power drawn by the pump when there is no rudder transient present is also higher. Since disconnecting the tie rod between rudder stocks does not in any way alter the lineup of the hydraulic piping, there is no reason it should be drawing more power. It is better, therefore to

look at the difference between the power drawn during a rudder transient and the power drawn with no rudder transient. Figure 6.15 shows the last three rudder transients from Figure 6.14.

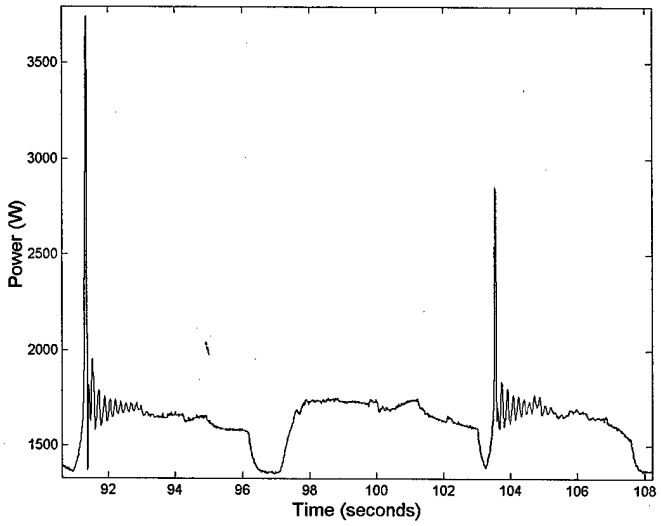

Figure 6.15: ONR YP Rudder Transients, Starboard Rudder Only

As for the transients with the tie rod connected, Figure 6.15 shows the rudder moving from left 25 degrees to 0 degrees, from 0 degrees to right 25 degrees, and finally from right 25 degrees back to 0 degrees. The characteristic difference between transients for deflection towards 0 degrees and transients for deflection away from 0 degrees are still present. The power level drawn for transients is also about 200 W higher than the baseline power level, just as for the case with the tie rod connected.

The only difference in transients with the tie rod disconnected is the shape of the power drawn during the transients. In Figure 6.13 the power transients with the tie rod connected show more oscillations during the rudder deflections. The power transients in Figure 6.15 however, show much smaller oscillations in power.

6.4 Chapter Summary

Based on the results presented previously, it is possible to detect faults associated with hydraulic cylinders in steering sytems onboard ships. For the two-cylinder system onboard the SENECA, a disabled cylinder is indicated by a difference in the steady state power level drawn for left and right rudder deflection. For the single-cylinder system onboard the ONR YP, the difference between one-rudder deflection and two-rudder deflection is indicated by the shape of power transient.

For the purposes of providing an indication of rudder angle, the two-cylinder system onboard the SENECA does not currently show an obvious difference in left and right rudder deflection. The single-cylinder system onboard the ONR YP only shows a difference in deflection away from zero versus deflection towards zero. If a method is developed to distinguish between left and right rudder deflections, rudder angle can be easily determined from the duration of the rudder deflection transient.

THIS PAGE INTENTIONALLY BLANK

Chapter 7

Future Work

7.1 Current Systems

7.1.1 NILM Hardware

The NILM Hardware used in the installations discussed in this thesis was able to collect data for analysis satisfactorily, but there is room for improvement.

Although the analog-to-digital conversion card used in the PCs performed well, they are extremely expensive. A universal serial bus (USB) interface developed at MIT by fellow LEES students will be used in the next generation of NILM installations. In addition to being more cost-effective, the USB NILM promises a much higher data collection rate than the current SCSI system.

A more advanced interface between the voltage and current transducers and the PC should also be investigated. If wiring terminal board resistors are sized to prevent an over-voltage condition in the analog-to-digital card for a load start, fidelity is lost in the steady state signal. An interface needs to be developed that adjusts the sensitivity of the signal to the computer based on the amount of current being drawn by the load. This hardware would ideally prevent damage during a large current peak but provide a high amount of fidelity for steady state signals.

In some instances (especially where power level and not frequency content is important) high or low pass filters should also be considered at the the interface between the transducers and the PC. This might allow recognition of much smaller changes in steady state power level.

7.1.2 NILM Software

The current state of the art in NILM software consists of the preprocesser that converts the voltage and current signals into a power envelope, the automatic data collection discussed in this thesis, and "demonstrator" software not discussed in this thesis that has been developed to track loads turning on and off. With the demonstrator software in "train" mode, load on and off transients are shown to the system. When the software is switched to "run", it is able to recognize on and off transients for any load that it has been trained to see.

The next step in NILM software should combine automatic data acquisition and storage, load on/off recognition, and recognition of large changes in steady state power level. Although not expected to have the advanced capabilities of the ideal system listed in Chapter 1, it should be able to trend equipment performance over time, recognize faults and create the corresponding error message, and store data for later analysis.

7.1.3 Cycling Systems

Although the "leak indicator" developed earlier is a good start for detecting a constant drain on a cycling system, it needs to be refined through further testing and simulation .

Improvements to the Sewage System Simulation

First, the simulation is based on pressure, and not leak flow rate. Leaks in a vacuum systems do not actually develop as a constant loss of vacuum, but rather as an intake of air into the system due to a loss of system integrity (e.g. loose fittings or holes in piping). This air intake is not constant over time for a loss of system integrity, but actually varies with the amount of vacuum in the system.

Second, the probably density function for flushes used was probably not very realistic. It is probably more realistic to use a probability density function whose cumulative distribution function *approaches* one as time goes to infinity. The binomial or Poisson distributions are good candidates (see [13]), they were not originally used because of the need to generate large amounts of data quickly.

Cross-System Validation

Another way that the leak indicator can be improved upon is through cross-system validation. Experiments should be run on other types of cycling systems to see if they are affected in the same way as the sewage system onboard the SENECA. The HVAC system onboard the ONR YP is a good candidate for such a system because it already contains a NILM installation.

The NILM installation for the ONR YP is using one voltage transducer and one LA 205-S current transducer to monitor two compressors, two heater banks, one seawater pump, and one chillwater pump. A schematic of the system is shown in Figure 7.1.

Chillwater is pumped through various thermostatically-controlled spot coolers around the ship. Chillwater flow through these spot coolers is constant while airflow through them cycles on and off to maintain temperature in each zone. The compressors for the HVAC system in turn cycle on and off to maintain chillwater temperature. An example of compressor cycling is shown in Figure 7.2.

The ONR YP HVAC system would be an excellent system to trend because it is affected by many variables. Not only are there many different combinations of thermostat settings which could be tried, but trends could also be analyzed for changes in air and seawater temperature.

7.1.4 Fluid Systems

Although large changes to the head loss of a fluid system (like those is section 5.4) are easy to see in the steady state power level of a pump, it has already been shown that small changes in a fluid system are not as easily detectable.

The equipment used thusfar to detect pressure waves which may be influencing the frequency spectrum of pump power measures vibration in piping, not fluid pressures. There are too many things which affect the vibration of the piping other than fluid flow, primarily mechanical vibration of the pump itself.

In the future, pressure transducers should be installed in the fluid test system to directly measure any pressure waves that are formed in the piping. This would better allow the frequency of interest in the power spectrum to be pinpointed to predict clogging failures.

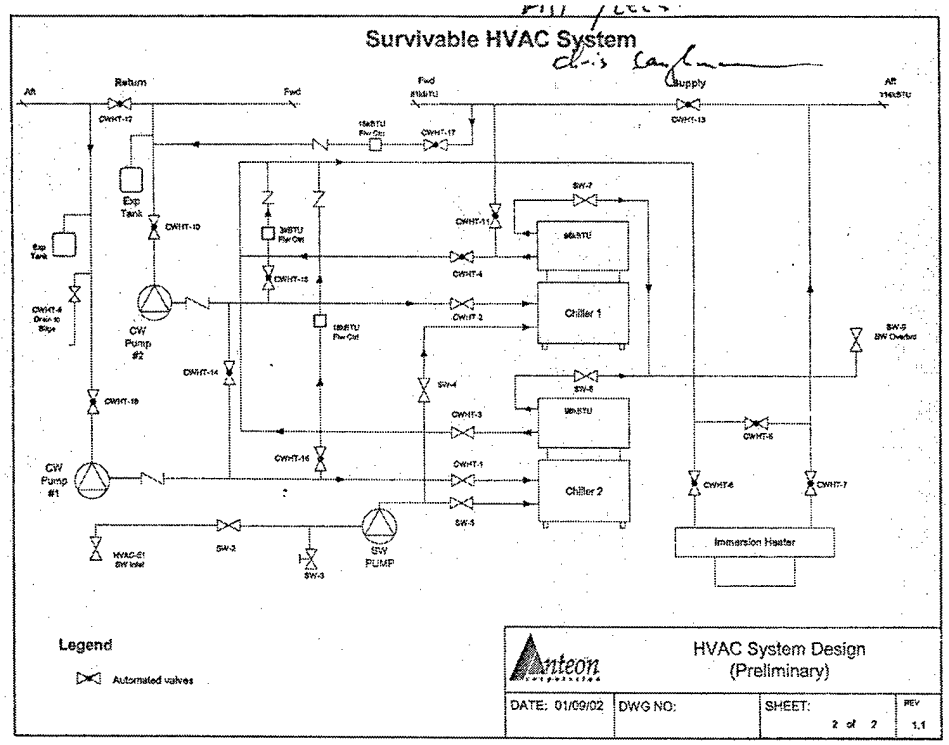

Figure 7.1: YP HVAC System

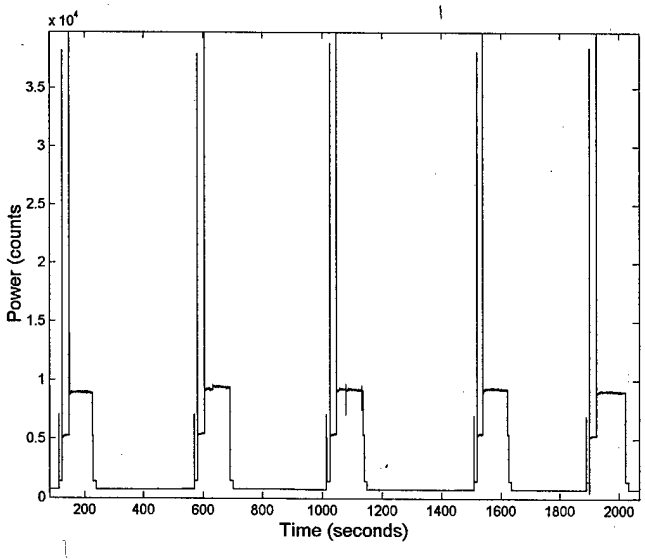

Figure 7.2: Compressor Cycling in ONR YP HVAC System

A good candidate is the K-series pressure transducer manufactured by Ashcroft. Available from Grainger Tools, this pressure transducer comes in a wide variety of pressure ranges, and has a stainless steel membrane to ensure longevity.

7.1.5 Hydraulic Systems

The results for the steering systems onboard the SENECA and ONR YP are all for inport data. There are two drawbacks to collecting data for a steering system while moored. First, there are no hydrodynamic forces on the rudders as a result of the ship's motion through the water. Second, the system is powered by shore power instead of the ship's onboard generating equipment. To predict performance while underway, tests must be conducted underway.

Some data was collected with the ONR YP underway. Turns were made at different speeds with different rudder angles, but there was a constant need to avoid traffic in the Chesapeake Bay. A plot of the track taken for underway testing on the ONR YP is shown in Figure 7.3. Unfortunately, the constant maneuvering that was required makes the data nearly impossible to interpret.

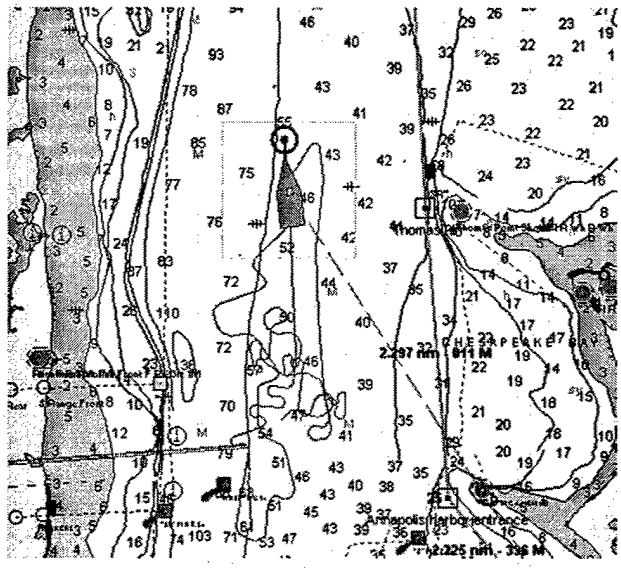

Figure 7.3: Track of YP Motion for Underway Testing

Because the steering system NILM installation on the SENECA does not have a dedicated computer, no underway data has been taken for that system. If data were to be collected automatically, it would have to be accompanied by a log of corresponding rudder motion. Although this log should be maintained anyway by the ship's quartermasters, it might be difficult to reconcile it with power data from the NILM if the two clocks used are out of agreement. Therefore, the best way to collect data on the SENECA is to put someone on the ship for controlled underway testing whose only duties are to collect NILM data while recording rudder motions.

7.2 Future Systems

Although there is more research that can be done on the systems featured in this thesis, data has been collected for other systems which has yet to be analyzed. There are also some promising systems for which very little data has been taken.

7.2.1 Anchor Windlass

The anchor windlass consists of a 20 hp variable speed drive connected through a reduction gear to a capstan and "wildcat". A wildcat is a geared drum which is used to pull up the anchor while a capstan is a taller, smooth drum that is located on the same axis as the wildcat and is used in conjunction with lines to moor the ship. There is a clutch on the wildcat to disengage it from the capstan so that the two can move independently.

It was reported by the Engineer Officer of the SENECA that the brake for the starboard anchor windlass would sometimes rub during operation. The anchor windlass was therefore tested for various combinations of capstan and wildcat engagement. A Tektronix 3054 oscilloscope was used to measure current to the variable speed drive. A plot of currents for fast speed operation is shown in Figure 7.4. For the case when the anchor has come off the bottom and is being pulled up by the wildcat, there is noticeable increase in current drawn by the motor.

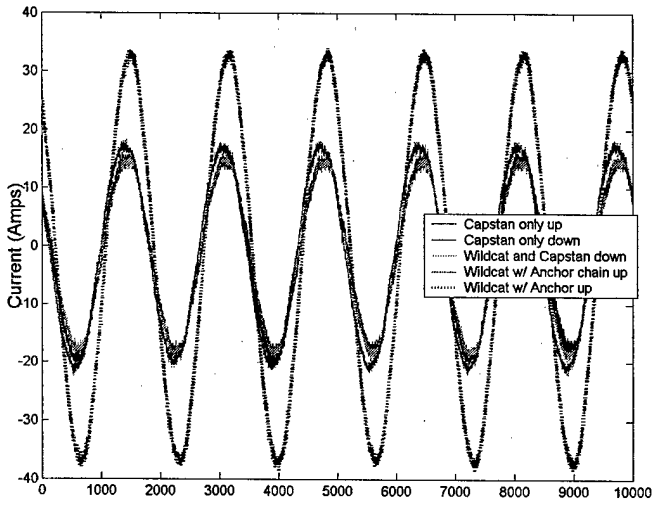

Figure 7.4: Anchor Windlass Currents for Different Loading Conditions

Installing a NILM on the anchor windlass could provide valuable information about the power signatures of motors tasked with moving large weights.

7.2.2 Roll Stabilization Fin

The SENECA has fins at the forward end of the hull on the port and starboard sides that are tasked with minimizing the effects of sea state on the roll motion of the ship. Actuation of the fins is hydraulic with 30 hp motors powering pumps that maintain pressure in the system. With the fins in automatic, pressure transducers that sense wave motion are used as the control input to position the fins. Actuation speed of the fins is variable and fin motion can be controlled manually.

It is possible that the power consumed by the hydraulic pumps that maintain pressure could be used as an indicator of fin position. It might even be possible to use this power data as an indication of sea state. An example of power transients for fast and slow speed motion with deflections of 10 degrees is shown in Figure 7.5.

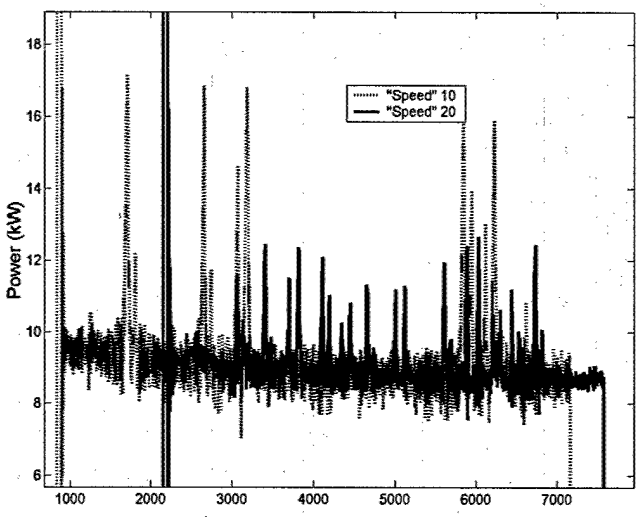

Figure 7.5: Roll Stabilizing Fin Power Transients for Two Speeds

7.2.3 Propeller Pitch Control

Yet another hydraulic system on the SENECA is the system that maintains pressure for the propeller pitch control. The angle of attack of the propeller blades is adjusted by this system so that the main engines can be operated at more efficient rpm.

There is a NILM installation that has collected underway data for the pumps that maintain system pressure. It is hoped that future analysis of this data (along with controlled testing) may provide indicators of shaft speed based on loading. The NILM data might also be useful as a backup indication of propeller pitch angle

7.3 Conclusions

There are too many shipboard systems which can be monitored by the NILM to list them all in this thesis. The results presented previously are all for systems that are ultimately mechanical in nature. The application of the NILM to more "purely" electrical systems (e.g. radar or communications) has yet to be explored.

The results presented in previous chapters show the suitability of the NILM for monitoring electrical loads on ships. It has been shown that it is capable of providing backup indications of system performance, trending equipment performance, and recognizing different fault conditions.

Further development of hardware and software along with continued research into the behavior of shipboard systems will make a highly capable NILM-based automated monitoring system a reality in the near future.

References

[1] Bruce R. Munson, Donald F. Young, and Theodore H. Okishi, *Fundamentals of Fluid Mechanics, Second Edition*, pp. 807-808, John Wiley and Sons, Inc., 1994.

[2] B. S. Payne, S. M. Husband, and A. D. Ball, "Development of Condition Monitoring Techniques for a Transverse Flux Motor", *International Conference on Power Electronics, Machines, and Drives*, pp. 139-144, June, 2002.

[3] H. Bruce Land III, "Sensing Shipboard Arc Faults", *IEEE Power Engineering Review*, Vol. 22, Issue 4, pp. 18-20, 27, April, 2002.

[4] Naval Sea Systems Command Website, *ICAS FAQ*, https://icas.navsses.navy.mil/, 2004.

[5] Christopher Laughman, Kwangduk Lee, Robert Cox, Steven Shaw, Steven Leeb, Les Norford, and Pete Armstrong, "Power Signature Analysis", *IEEE Power & Energy Magazine*, Vol. 1, Issue 2, pp. 56-63, March-April, 2003.

[6] Karen L. Butler, N. D. R. Sarma, Cliff Whitcomb, Hyder Do Carmo, and Haibo Zhang, "Shipboard Systems Deploy Automated Protection", *IEEE Computer Applications in Power*, Vol. 11, Issue 2, pp. 31-36, April, 1998.

[7] C. T. Marwood, "Integrated Control and Monitoring Systems - A Growing Requirement", *IEEE Colloquium on Control in the Marine Industry*, January, 1988.

[8] S. Fryze,"Active, reactive, and apparent powers in nonsinusoidal systems" *Przeglad Elektrot*, no. 7, pp. 193-203, 1931 (in Polish).

[9] Kwangduk Douglas Lee, *Electric Load Information System based on Non-Intrusive Power Monitoring*, pp. 23-27, Massachusetts Institute of Technology, June, 2003.

[10] Robert E. Simpson, *Introductory Electronics for Scientists and Engineers, Second Edition*, p. 457, Allyn and Bacon, inc., Newton, MA, 1987.

[11] A. E. Fitzgerald, Charles Kingsley Jr., and Stephen D. Umans, *Electric Machinery, Fifth Edition*, p. 540, McGraw-Hill, Inc., 1990.

[12] Fluke Corporation, *Fluke 39/41B Power Harmonics Tester Users Manual, Rev. 3*, p. 11, 1995.

[13] Robert V. Hogg and Johannes Ledolter, *Engineering Statistics*, p. 124, Macmillan Publishing Company, 1987.

[14] Gilbert Strang, *Introduction to Linear Algebra, Second Edition*,p. 353, Wellesley-Cambridge Press, 1998.

[15] Steven B. Leeb, MATLAB Scripts `indparam.m` , `ind.m`, `convind.m`, *6.11s: Design of Motors, Generators and Drive Systems*, Massachusetts Institute of Technology, 2003.

[16] Worthington Group, McGraw-Edison Company, *Aux. Salt Water Cooling Pump Outline and Certification Data*, Technical Data Sheet dtd March 31, 1982.

[17] E. Benjamin Wylie and Victor L. Streeter, *Fluid Transients in Systems*, p. 148, Prentice-Hall, Inc., 1993.

[18] Michael R. Lindeburg, *Mechanical Engineering Reference Manual for the PE Exam, Tenth Edition*, Professional Publications, inc., 1998.

[19] MK1 Thomas Kiley, USCG, email correspondence dated April 19, 2004.

[20] Robert D. Strum and Donald E. Kirk, *Contemporary Linear Systems Using MATLAB*, pp. 544-545, PWS Publishing Company, 1994.

Appendix A

Transducer Specifications

The information provided on the following pages provides technical specifications for the voltage and current transducers typically used for shipboard NILM installations.

THIS PAGE INTENTIONALLY BLANK

Voltage Transducer LV 25-P

I_{PN} = 10 mA

V_{PN} = 10 .. 500 V

For the electronic measurement of voltages : DC, AC, pulsed..., with a galvanic isolation between the primary circuit (high voltage) and the secondary circuit (electronic circuit).

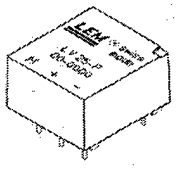

Electrical data

I_{PN}	Primary nominal r.m.s. current		10		mA
I_P	Primary current, measuring range		0 .. ± 14		mA
R_M	Measuring resistance		$R_{M\,min}$	$R_{M\,max}$	
	with ± 12 V	@ ± 10 mA $_{max}$	30	190	Ω
		@ ± 14 mA $_{max}$	30	100	Ω
	with ± 15 V	@ ± 10 mA $_{max}$	100	350	Ω
		@ ± 14 mA $_{max}$	100	190	Ω
I_{SN}	Secondary nominal r.m.s. current		25		mA
K_N	Conversion ratio		2500 : 1000		
V_C	Supply voltage (± 5 %)		± 12 .. 15		V
I_C	Current consumption		10 (@ ± 15 V) + I_S		mA
V_d	R.m.s. voltage for AC isolation test [1], 50 Hz, 1 mn		2.5		kV

Accuracy - Dynamic performance data

X_G	Overall Accuracy @ I_{PN}, T_A = 25°C	@ ± 12 .. 15 V	± 0.9		%
		@ ± 15 V (± 5 %)	± 0.8		%
ε_L	Linearity		< 0.2		%
			Typ	Max	
I_O	Offset current @ I_P = 0, T_A = 25°C			± 0.15	mA
I_{OT}	Thermal drift of I_O	0°C .. + 25°C	± 0.06	± 0.25	mA
		+ 25°C .. + 70°C	± 0.10	± 0.35	mA
t_r	Response time [2] @ 90 % of $V_{P\,max}$		40		µs

General data

T_A	Ambient operating temperature	0 .. + 70	°C
T_S	Ambient storage temperature	- 25 .. + 85	°C
R_P	Primary coil resistance @ T_A = 70°C	250	Ω
R_S	Secondary coil resistance @ T_A = 70°C	110	Ω
m	Mass	22	g
	Standards [3]	EN 50178	

Notes : [1] Between primary and secondary

[2] R_t = 25 kΩ (L/R constant, produced by the resistance and inductance of the primary circuit)

[3] A list of corresponding tests is available

Features

- Closed loop (compensated) voltage transducer using the Hall effect
- Insulated plastic case recognized according to UL 94-V0.

Principle of use

- For voltage measurements, a current proportional to the measured voltage must be passed through an external resistor R_1 which is selected by the user and installed in series with the primary circuit of the transducer.

Advantages

- Excellent accuracy
- Very good linearity
- Low thermal drift
- Low response time
- High bandwidth
- High immunity to external interference
- Low disturbance in common mode.

Applications

- AC variable speed drives and servo motor drives
- Static converters for DC motor drives
- Battery supplied applications
- Uninterruptible Power Supplies (UPS)
- Power supplies for welding applications.

981125/14

Dimensions LV 25-P (in mm. 1 mm = 0.0394 inch)

Bottom view

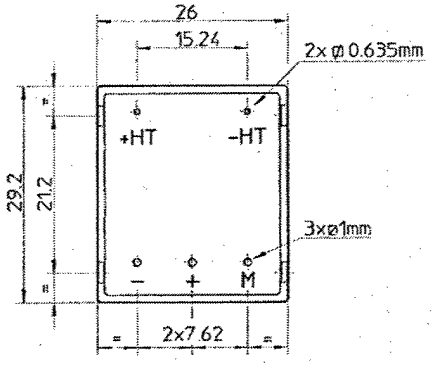

Right view

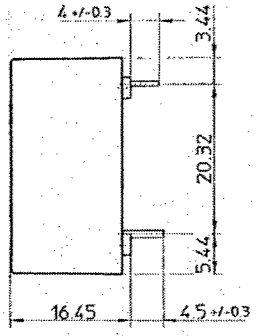

Top view

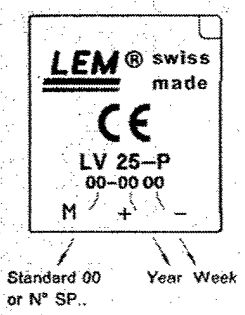

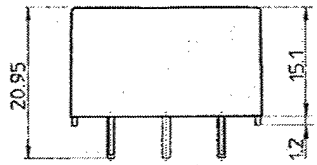

Back view

Secondary terminals

Terminal + : supply voltage + 12 .. 15 V
Terminal M : measure
Terminal - : supply voltage - 12 .. 15 V

Connection

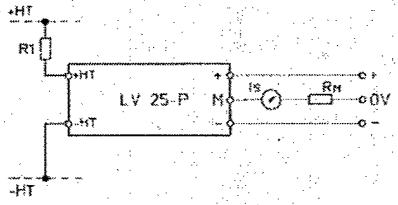

Mechanical characteristics

• General tolerance	± 0.2 mm
• Fastening & connection of primary	2 pins 0.635 x 0.635 mm
• Fastening & connection of secondary	3 pins Ø 1 mm
• Recommended PCB hole	1.2 mm

Remarks

- I_S is positive when V_P is applied on terminal +HT.
- This is a standard model. For different versions (supply voltages, turns ratios, unidirectional measurements...), please contact us.

Instructions for use of the voltage transducer model LV 25-P

Primary resistor R_1 : the transducer's optimum accuracy is obtained at the nominal primary current. As far as possible, R_1 should be calculated so that the nominal voltage to be measured corresponds to a primary current of 10 mA.

Example: Voltage to be measured V_{PN} = 250 V
a) R_1 = 25 kΩ / 2.5 W, I_P = 10 mA Accuracy = ± 0.8 % of V_{PN} (@ T_A = +25°C)
b) R_1 = 50 kΩ / 1.25 W, I_P = 5 mA Accuracy = ± 1.6 % of V_{PN} (@ T_A = +25°C)

Operating range (recommended) : taking into account the resistance of the primary windings (which must remain low compared to R_1, in order to keep thermal deviation as low as possible) and the isolation, this transducer is suitable for measuring nominal voltages from 10 to 500 V.

Current Transducer LA 55-P

I_{PN} = 50 A

For the electronic measurement of currents : DC, AC, pulsed..., with a galvanic isolation between the primary circuit (high power) and the secondary circuit (electronic circuit).

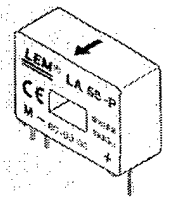

Electrical data

I_{PN}	Primary nominal r.m.s. current				50			A
I_P	Primary current, measuring range				0 .. ± 70			A
R_M	Measuring resistance @		T_A = 70°C		T_A = 85°C			
			$R_{M\,min}$	$R_{M\,max}$	$R_{M\,min}$	$R_{M\,max}$		
	with ± 12 V	@ ± 50 A_{max}	10	100	60	95		Ω
		@ ± 70 A_{max}	10	50	60[1]	60[1]		Ω
	with ± 15 V	@ ± 50 A_{max}	50	160	135	155		Ω
		@ ± 70 A_{max}	50	90	135[2]	135[2]		Ω
I_{SN}	Secondary nominal r.m.s. current				50			mA
K_N	Conversion ratio				1 : 1000			
V_C	Supply voltage (± 5 %)				± 12 .. 15			V
I_C	Current consumption				10 (@ ±15 V) + I_S			mA
V_d	R.m.s. voltage for AC isolation test, 50 Hz, 1 mn				2.5			kV

Accuracy - Dynamic performance data

X	Accuracy @ I_{PN}, T_A = 25°C	@ ± 15 V (± 5 %)	± 0.65		%
		@ ± 12 .. 15 V (± 5 %)	± 0.90		%
ε_L	Linearity		< 0.15		%
			Typ	Max	
I_O	Offset current @ I_P = 0, T_A = 25°C			± 0.2	mA
I_{OM}	Residual current[3] @ I_P = 0, after an overload of 3 x I_{PN}			± 0.3	mA
I_{OT}	Thermal drift of I_O	0°C .. + 70°C	± 0.1	± 0.5	mA
		- 25°C .. + 85°C	± 0.1	± 0.6	mA
t_{ra}	Reaction time @ 10 % of $I_{P\,max}$		< 500		ns
t_r	Response time @ 90 % of $I_{P\,max}$		< 1		µs
di/dt	di/dt accurately followed		> 200		A/µs
f	Frequency bandwidth (- 1 dB)		DC .. 200		kHz

General data

T_A	Ambient operating temperature		- 25 .. + 85	°C
T_S	Ambient storage temperature		- 40 .. + 90	°C
R_S	Secondary coil resistance @	T_A = 70°C	80	Ω
		T_A = 85°C	85	Ω
m	Mass		18	g
	Standards[4]		EN 50178	

Notes : [1] Measuring range limited to ± 60 A_{max}
[2] Measuring range limited to ± 55 A_{max}
[3] Result of the coercive field of the magnetic circuit
[4] A list of corresponding tests is available

Features

- Closed loop (compensated) current transducer using the Hall effect
- Printed circuit board mounting
- Insulated plastic case recognized according to UL 94-V0.

Advantages

- Excellent accuracy
- Very good linearity
- Low temperature drift
- Optimized response time
- Wide frequency bandwidth
- No insertion losses
- High immunity to external interference
- Current overload capability.

Applications

- AC variable speed drives and servo motor drives
- Static converters for DC motor drives
- Battery supplied applications
- Uninterruptible Power Supplies (UPS)
- Switched Mode Power Supplies (SMPS)
- Power supplies for welding applications.

980706/8

Dimensions LA 55-P (in mm. 1 mm = 0.0394 inch)

Bottom view

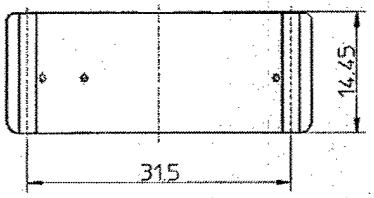

Left view

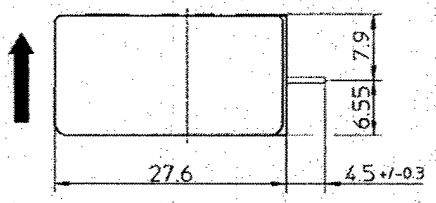

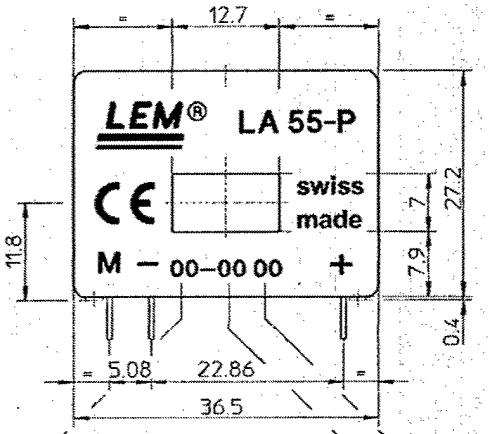

Front view

Secondary terminals

Terminal + : supply voltage + 12 .. 15 V
Terminal - : supply voltage - 12 .. 15 V
Terminal M : measure

Connection

Mechanical characteristics

• General tolerance	± 0.2 mm
• Primary through-hole	12.7 x 7 mm
• Fastening & connection of secondary	3 pins 0.63 x 0.56mm
Recommended PCB hole	0.9 mm

Remarks

- I_s is positive when I_p flows in the direction of the arrow.
- Temperature of the primary conductor should not exceed 90°C.
- Dynamic performances (di/dt and response time) are best with a single bar completely filling the primary hole.
- In order to achieve the best magnetic coupling, the primary windings have to be wound over the top edge of the device.
- This is a standard model. For different versions (supply voltages, turns ratios, unidirectional measurements...), please contact us.

Current Transducer LA 205-S

I_{PN} = 200 A

For the electronic measurement of currents : DC, AC, pulsed..., with a galvanic isolation between the primary circuit (high power) and the secondary circuit (electronic circuit).

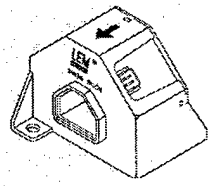

Electrical data

I_{PN}	Primary nominal r.m.s. current			200			A
I_P	Primary current, measuring range			0 .. ± 300			A
$I_{P\,max}$	Measuring overload [1]			600			A
R_M	Measuring resistance @		T_A = 70°C		T_A = 85°C		
			$R_{M\,min}$	$R_{M\,max}$	$R_{M\,min}$	$R_{M\,max}$	
	with ± 12 V	@ ± 200 A_{max}	0	68	0	66	Ω
		@ ± 300 A_{max}	0	33	0	30	Ω
	with ± 15 V	@ ± 200 A_{max}	5	95	5	93	Ω
		@ ± 300 A_{max}	5	50	5	49	Ω
I_{SN}	Secondary nominal r.m.s. current			100			mA
K_N	Conversion ratio			1 : 2000			
V_C	Supply voltage (± 5 %)			± 12 .. 15			V
I_C	Current consumption			20 (@ ± 15V) + I_S			mA
V_b	R.m.s rated voltage [2], safe separation			1625			V
	basic isolation			3250			V

Accuracy - Dynamic performance data

X_G	Overall accuracy @ I_{PN}, T_A = 25°C		± 0.8		%
ε_L	Linearity		< 0.1		%
			Typ	Max	
I_O	Offset current @ I_P = 0, T_A = 25°C			± 0.15	mA
I_{OM}	Residual current [3] @ I_P = 0, after an overload of 3 x I_{PN}			± 0.50	mA
I_{OT}	Thermal drift of I_O	- 10°C .. + 85°C	± 0.15	± 0.30	mA
t_{ra}	Reaction time @ 10 % of $I_{P\,max}$		< 500		ns
t_r	Response time [4] @ 90 % of $I_{P\,max}$		< 1		µs
di/dt	di/dt accurately followed		> 100		A/µs
f	Frequency bandwidth (- 3 dB)		DC .. 100		kHz

General data

T_A	Ambient operating temperature		- 10 .. + 85	°C
T_S	Ambient storage temperature		- 40 .. + 90	°C
R_S	Secondary coil resistance @	T_A = 70°C	35	Ω
		T_A = 85°C	37	Ω
m	Mass		110	g
	Standards [5]		EN 50178	

Notes : [1] 3 mn/hour @ V_C = ± 15 V, R_M = 5 Ω
[2] Pollution class nr 2. With a non insulated primary bar which fills the through-hole
[3] The result of the coercive field of the magnetic circuit
[4] With a di/dt of 100 A/µs
[5] A list of corresponding tests is available

Features

- Closed loop (compensated) current transducer using the Hall effect
- Insulated plastic case recognized according to UL 94-V0
- Patent pending.

Advantages

- Excellent accuracy
- Very good linearity
- Low temperature drift
- Optimized response time
- Wide frequency bandwidth
- No insertion losses
- High immunity to external interference
- Current overload capability.

Applications

- AC variable speed drives and servo motor drives
- Static converters for DC motor drives
- Battery supplied applications
- Uninterruptible Power Supplies (UPS)
- Switched Mode Power Supplies (SMPS)
- Power supplies for welding applications.

980716/5

Dimensions LA 205-S (in mm. 1 mm = 0.0394 inch)

Front view

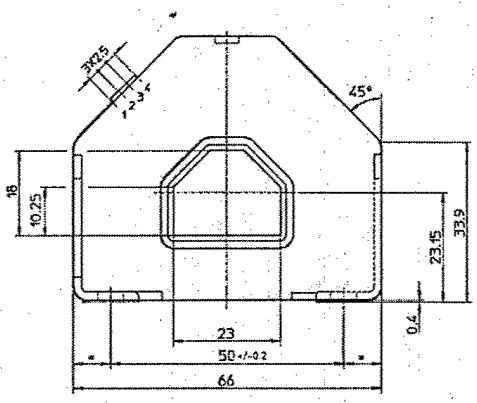

Left view

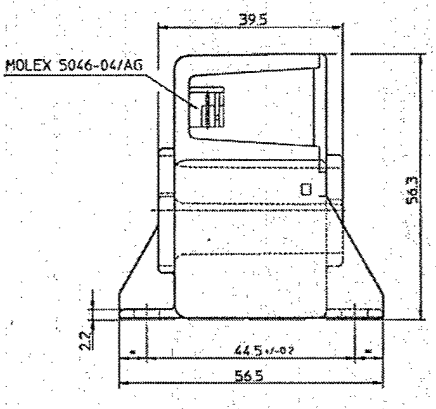

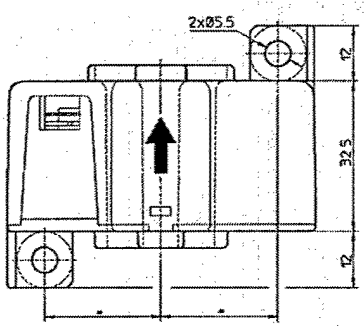

Top view

Secondary terminals

Pin 1 : supply voltage + 12 .. 15 V
Pin 2 : measure
Pin 3 : supply voltage - 12 .. 15 V
Pin 4 : NC

Connection

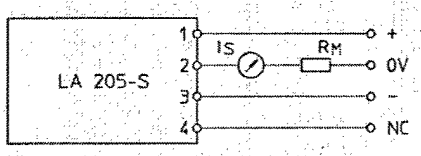

Mechanical characteristics

• General tolerance	± 0.5 mm
• Fastening	2 holes Ø 5.5 mm
• Primary through-hole	23 x 18 mm
• Connection of secondary	Molex 5046-04/AG

Remarks

- I_s is positive when I_p flows in the direction of the arrow.
- Temperature of the primary conductor should not exceed 100°C.
- Dynamic performances (di/dt and response time) are best with a single bar completely filling the primary hole.
- This is a standard model. For different versions (supply voltages, turns ratios, unidirectional measurements...), please contact us.

Current Transducer LA 305-S

I_{PN} = 300 A

For the electronic measurement of currents : DC, AC, pulsed..., with a galvanic isolation between the primary circuit (high power) and the secondary circuit (electronic circuit).

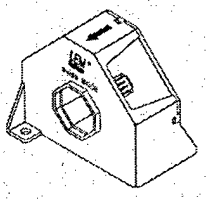

Electrical data

I_{PN}	Primary nominal r.m.s. current				300			A
I_P	Primary current, measuring range				0 .. ± 500			A
R_M	Measuring resistance @		T_A = 70°C		T_A = 85°C			
			$R_{M\,min}$	$R_{M\,max}$	$R_{M\,min}$	$R_{M\,max}$		
	with ± 12 V	@ ± 300 A_{max}	0	52	0	50		Ω
		@ ± 500 A_{max}	0	17	0	15		Ω
	with ± 15 V	@ ± 300 A_{max}	0	75	5	73		Ω
		@ ± 500 A_{max}	0	31	5	29		Ω
I_{SN}	Secondary nominal r.m.s. current				120			mA
K_N	Conversion ratio				1 : 2500			
V_C	Supply voltage (± 5 %)				± 12 .. 15			V
I_C	Current consumption				20 (@ ± 15 V) + I_S			mA
V_b	R.m.s. rated voltage [1], safe separation				1750			V
	basic isolation				3500			V

Accuracy - Dynamic performance data

X_G	Overall accuracy @ I_{PN}, T_A = 25°C		± 0.8		%
ε_L	Linearity		< 0.1		%
			Typ	Max	
I_O	Offset current @ I_P = 0, T_A = 25°C			± 0.20	mA
I_{OM}	Residual current [2] @ I_P = 0, after an overload of 3 x I_{PN}			± 0.40	mA
I_{OT}	Thermal drift of I_O	- 10°C .. + 85°C	± 0.12	± 0.30	mA
t_{ra}	Reaction time @ 10 % of $I_{P\,max}$		< 500		ns
t_r	Response time [3] @ 90 % of $I_{P\,max}$		< 1		µs
di/dt	di/dt accurately followed		> 100		A/µs
f	Frequency bandwidth (- 3 dB)		DC .. 100		kHz

General data

T_A	Ambient operating temperature		- 10 .. + 85	°C
T_S	Ambient storage temperature		- 40 .. + 90	°C
R_S	Secondary coil resistance @	T_A = 70°C	35	Ω
		T_A = 85°C	37	Ω
m	Mass		200	g
	Standards [4]		EN 50178	

Notes : [1] Pollution class 2. With a non insulated primary bar which fills the through-hole
[2] The result of the coercive field of the magnetic circuit
[3] With a di/dt of 100 A/µs
[4] A list of corresponding tests is available

Features

- Closed loop (compensated) current transducer using the Hall effect
- Insulated plastic case recognized according to UL 94-V0
- Copyright protected.

Advantages

- Excellent accuracy
- Very good linearity
- Low temperature drift
- Optimized response time
- Wide frequency bandwidth
- No insertion losses
- High immunity to external interference
- Current overload capability.

Applications

- AC variable speed drives and servo motor drives
- Static converters for DC motor drives
- Battery supplied applications
- Uninterruptible Power Supplies (UPS)
- Switched Mode Power Supplies (SMPS)
- Power supplies for welding applications.

980707/6

Dimensions LA 305-S (in mm. 1 mm = 0.0394 inch)

Front view

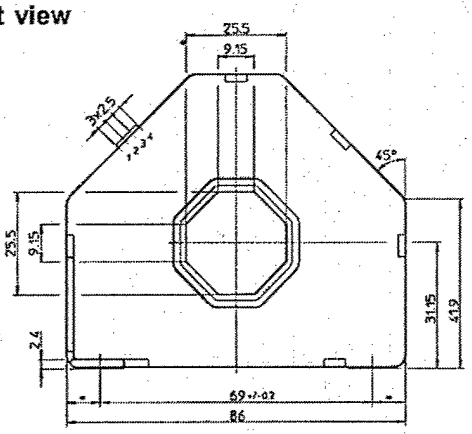

Left view

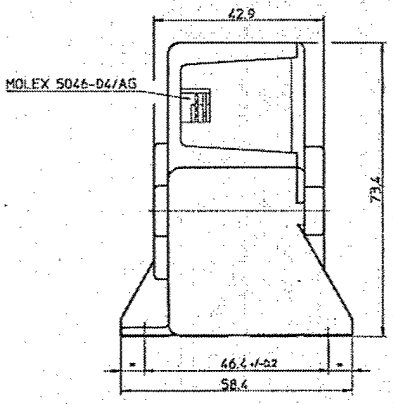

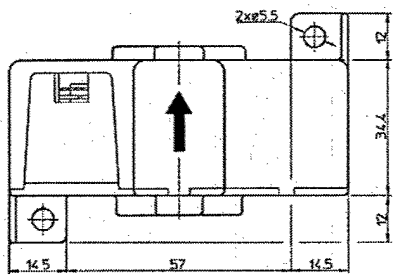

Top view

Secondary terminals

Pin 1 : supply voltage + 12 .. 15 V
Pin 2 : measure
Pin 3 : supply voltage - 12 .. 15 V
Pin 4 : NC

Connection

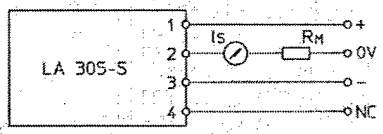

Mechanical characteristics

• General tolerance	± 0.5 mm
• Fastening	2 holes Ø 5.5 mm
• Primary through-hole	25.5 x 25.5 mm
• Connection of secondary	Molex 5046-04/AG

Remarks

- I_s is positive when I_p flows in the direction of the arrow.
- Temperature of the primary conductor should not exceed 100°C.
- Dynamic performances (di/dt and response time) are best with a single bar completely filling the primary hole.
- This is a standard model. For different versions (supply voltages, turns ratios, unidirectional measurements...), please contact us.

Appendix B

NILM Hardware Listing

The purpose of this appendix is to provide construction information for individuals performing future work with the NILM.

Table B.1: Electrical Components Required for Voltage Sensing Board

Part	Value	Qty.	Supplier	Part No.
Capacitor	$0.1\mu F$ ceramic	2	Various	N/A
	$1\mu F$ ceramic	2		
	$10\mu F$ electrolytic	2		
Resistor	$100k\Omega$	9	Digikey	BC100KW-3JCT
	$470k\Omega$	9	Digikey	BC470KW-3JCT
Transducer	N/A	3	LEM	LV 25-P
Fuseholder	N/A	1	Littlefuse	L60060M-3PQ
Fuse	100 mA/600 V	3	Littlefuse	KLKR1/10
Wire and Crimp Lug	12 AWG	3	Various	N/A
Straight Term. Block	2-pin	1	Digikey	ED2354-ND
Diag. Term. Block	2-pin	4	Digikey	281-1421-ND

Table B.2: Additional Electrical Components Required for NILM Setup

Part	Value	Qty.	Supplier	Part No.
Power Supply	$\pm 12V$	1	Jameco	148689
Wiring Terminal	68-pin SCSI-II	1	Advantech	ADAM-3968
A/D Converter	PCI	1	Advantech	PCI-1710
SCSI-II Cable	68-pin	1	Various	N/A
Power Cable	120V	1	Various	N/A

Table B.3: Hardware Required for NILM Box

Part	Value	Qty.	Purpose
NEMA Box	12"x10"x5"	1	House voltage board, terminal board, and power supply
Backplane	12"x10"x5"	1	Mounting surface for voltage board
Phillips Machine Screw	10x32, 0.75" length	6	Mount voltge board and junction strip to backplane
Phillips Machine Screw	10x32, 0.5" length	2	Mount DIN rail to box
Spacer	10x32, smooth interior, 0.25" length, aluminum	4	Between voltage board and backplane
Lock Washer and Nut	10x32	4	For voltage board and junction strip
Spacer	6x32, threaded, 0.5" length, aluminum	4	Mount power supply to side of NEMA box
Lock Washer and Nut	6x32	4	Secure spacers to NEMA box
Phillips Machine Screw	6x32, 0.375" length	4	Attaching power supply to spacers
Junction Strip	3-terminal	1	Provide power to current transducer
Molex Connector	3-pin	1	Power cord connection to power supply
Molex Connector	4-pin	1	Power supply connection to voltage board and junction strip
Wire Clamps	0.375" "Halex"	3	Strain relief for voltage input, current input, and power cord
DIN Rail	10" length	1	Mounting for SCSI-II wiring terminal board

Appendix C

Sewage System MATLAB Scripts

The following script was written to trend vacuum pump cycling in the sewage system of the USCGC SENECA. The input vector A is power data sampled at 120 Hz for the sewage system. The output is the number of times that one or both of the pumps was running along with the average time of each pump run.

```
j=0;
z=ones(size(y));
for i=1:length(y);
    if y(i)>500
        z(i)=1;
    else z(i)=0;
    end
end
z;
if z(1)==1
    j=j+1;
end
for i=2:length(z);
    if z(i)==1
        if z(i-1)==0
            j=j+1;
        end
    end
end
runs=j
average_run_time=sum(z)/(j*120)
```

The following script simulates operation of the sewage system vacuum pumps onboard the USCGC SENECA. The average time between system usages is and amount of vacuum leak is input with number pump runs and average run time per run output.

```
function [runs,runtime]=flushsim(time_flush,Pdot_leak)
n=60;                   % simulation time (min);
k=200;                  % number of points per minute in simulation
P_flush=1;              % pressure decrease caused by toilet flush (in Hg)
Pdot_pump1=19;          % vacuum rate gained by pump1 (in Hg/min)
Pdot_pump2=17;          % vacuum rate gained by pump2 (in Hg/min)
Plower_setpt=7.5;       % vacuum at which two pumps come on (in Hg)
Plow_setpt=10;          % vacuum at which pump comes on (in Hg)
Phigh_setpt=15;         % vacuum at which pump shuts off (in Hg)
P(1)=15;
Pump_status=0;
Twopump_status=0;
flush_count=0;
j=0;
for i=2:n*k;
    if P(i-1) < Plow_setpt
        Pump_status=1;
    elseif P(i-1) > Phigh_setpt
        Pump_status=0;
        Twopump_status=0;
    end
    if P(i-1) < Plower_setpt
        Twopump_status=1;
    end
    if Twopump_status==1
        Pump_status=0;
    end
Pump_Counter(i)=Pump_status + Twopump_status;
    if Pump_Counter(i)==1
        if Pump_Counter(i-1)==0
            j=j+1;
        end
    end
    if flush_count/k < time_flush
    flushprob=(flush_count/k)^2/(2*time_flush^2);
    else
    flushprob=1-((2*time_flush-(flush_count/k))^2/(2*time_flush^2));
    end
flushchance=rand;
    if flushchance < flushprob
        dP_flush=P_flush;
        flush_count=0;
    else
        flush_count=flush_count+1;
```

```
        dP_flush=0;
    end
    if rem(j,2)==0
        Pdot_pump=Pdot_pump2;
    else
        Pdot_pump=Pdot_pump1;
    end
    P(i)=P(i-1)-dP_flush-(Pdot_leak)*(1/k) + Pump_status*Pdot_pump*(1/k)
         + Twopump_status*(Pdot_pump1 + Pdot_pump2)*(1/k);
end
runs=j;
runtime=sum(Pump_Counter)*60/(j*k);
```

THIS PAGE INTENTIONALLY BLANK

Appendix D

Sewage System Leak Data

The following data was taken onboard the USCGC SENECA between February 20 and March 6, 2004:

Leak Data for Leak Rate of 0 SCFH

Hour	Runs	Time per run (seconds)	Total runtime (seconds)
1800-1900	15	23.78	356.7
1900-2000	10	26.14	261.4
2000-2100	10	19.56	195.6
2100-2200	6	17.05	102.3
2200-2300	7	18.47	129.29
2300-0000	8	21.62	172.96
0000-0100	15	23.99	359.85
0100-0200	7	18.78	131.46
0200-0300	6	16.49	98.94
0300-0400	7	17.12	119.84
0400-0500	8	19.16	153.28
0500-0600	6	17.24	103.44
0600-0700	7	17.11	119.77
0700-0800	13	21.39	278.07
0800-0900	10	19.57	195.7
0900-1000	8	19.63	157.04
1000-1100	10	18.62	186.2
1100-1200	10	22.28	222.8
1200-1300	11	18.41	202.51
1300-1400	9	21.79	196.11
1400-1500	10	17.47	174.7
1500-1600	8	17.18	137.44

Leak Data for Leak Rate of 42 SCFH

Hour	Runs	Time per run (seconds)	Total runtime (seconds)
1800-1900	12	17.01	204.12
1900-2000	12	22.32	267.84
2000-2100	9	19.89	179.01
2100-2200	9	19.88	178.92
2200-2300	8	21.28	170.24
2300-0000	8	24.88	199.04
0000-0100	7	15.9	111.3
0100-0200	7	13.18	92.26
0200-0300	7	15.41	107.87
0300-0400	10	15.71	157.1
0400-0500	7	15.45	108.15
0500-0600	11	18.85	207.35
0600-0700	17	20.33	345.61
0700-0800	24	20.46	491.04
0800-0900	15	20.56	308.4
0900-1000	24	21.94	526.56
1000-1100	14	24.7	345.8
1100-1200	17	27.1	460.7
1200-1300	19	24.75	470.25
1300-1400	14	27.13	379.82
1400-1500	12	23.02	276.24
1500-1600	10	18.98	189.8

Leak Data for Leak Rate of 51 SCFH

Hour	Runs	Time per run (seconds)	Total runtime (seconds)
1700-1800	15	26.59	398.85
1800-1900	16	25.5	408
1900-2000	10	22.05	220.5
2000-2100	11	21.15	232.65
2100-2200	9	15.55	139.95
2200-2300	9	16.82	151.38
2300-0000	10	20.86	208.6
0000-0100	8	17.05	136.4
0100-0200	8	15.27	122.16
0200-0300	8	17.7	141.6
0300-0400	9	18.14	163.26
0400-0500	9	15.78	142.02
0500-0600	12	20.51	246.12
0600-0700	22	21.66	476.52
0700-0800	21	21.33	447.93
0800-0900	18	26.62	479.16
0900-1000	25	24.62	615.5
1000-1100	21	30.51	640.71
1100-1200	16	22.27	356.32
1200-1300	23	22.15	509.45
1300-1400	23	23.65	543.95
1400-1500	11	25.23	277.53
1500-1600	13	20.11	261.43

Leak Data for Leak Rate of 62.5 SCFH

Hour	Runs	Time per run (seconds)	Total runtime (seconds)
1700-1800	13	24.93	324.09
1800-1900	16	20.77	332.32
1900-2000	12	20.46	245.52
2000-2100	10	17.76	177.6
2100-2200	13	17.85	232.05
2200-2300	14	19.79	277.06
2300-0000	10	18.41	184.1
0000-0100	10	16.96	169.6
0100-0200	9	15.29	137.61
0200-0300	10	15.4	154
0300-0400	11	15.61	171.71
0400-0500	9	18.49	166.41
0500-0600	14	18.51	259.14
0600-0700	23	20.82	478.86
0700-0800	13	20.63	268.19
0800-0900	13	30.5	396.5
0900-1000	20	22.39	447.8
1000-1100	22	22.94	504.68
1100-1200	19	26.99	512.81
1200-1300	22	22.95	504.9
1300-1400	18	28.09	505.62
1400-1500	18	20.74	373.32
1500-1600	15	19.11	286.65

Leak Data for Leak Rate of 102.5 SCFH

Hour	Runs	Time per run (seconds)	Total runtime (seconds)
1700-1800	16	22.11	353.76
1800-1900	11	19.34	212.74
1900-2000	12	22.6	271.2
2000-2100	11	17.35	190.85
2100-2200	10	21.1	211
2200-2300	11	18.48	203.28
2300-0000	11	18.28	201.08
0000-0100	10	15.39	153.9
0100-0200	9	18.13	163.17
0200-0300	9	16.88	151.92
0300-0400	11	26.55	292.05
0400-0500	9	16.56	149.04
0500-0600	9	17.65	158.85
0600-0700	9	17.3	155.7
0700-0800	14	20.3	284.2
0800-0900	14	19.71	275.94
0900-1000	12	22.32	267.84
1000-1100	11	20.17	221.87
1100-1200	15	20.03	300.45
1200-1300	16	17.56	280.96
1300-1400	10	23.13	231.3
1400-1500	10	20.27	202.7
1500-1600	11	21.61	237.71

Leak Data for Leak Rate of 132.5 SCFH

Hour	Runs	Time per run (seconds)	Total runtime (seconds)
1700-1800	19	25.32	481.08
1800-1900	16	22.43	358.88
1900-2000	17	22.4	380.8
2000-2100	16	18.26	292.16
2100-2200	15	18.38	275.7
2200-2300	19	16.78	318.82
2300-0000	23	16.12	370.76
0000-0100	21	16.76	351.96
0100-0200	22	15.8	347.6
0200-0300	25	18.5	462.5
0300-0400	24	25.79	618.96
0400-0500	26	15.37	399.62
0500-0600	28	16.7	467.6
0600-0700	31	20.14	624.34

The following data was produced by the MATLAB simulation script `flushsim`:

Simulated Weekday Data for Leak Rate of 0 in./minute

Mean Time Between Flushes	**Runs**	**Time per run (seconds)**	**Total runtime (seconds)**
5	12	20.625	247.5
5	11	19.96363636	219.6
5	12	20.075	240.9
5	12	20.075	240.9
2	21	20.95714286	440.1
1	29	23.4	678.6
5	12	20.075	240.9
2	22	21.40909091	471
5	12	20.075	240.9
1	32	22.33125	714.6
2	21	20.92857143	439.5
5	12	20.075	240.9
5	11	19.96363636	219.6
5	12	20.075	240.9
7	9	19.96666667	179.7
7	10	20.07	200.7
7	10	18.3	183
5	12	20.075	240.9
5	11	19.96363636	219.6
7	10	20.07	200.7
5	12	20.075	240.9
5	11	20.26363636	222.9
2	20	22.245	444.9
5	11	19.96363636	219.6

Simulated Weekday Data for Leak Rate of 0.5 in./minute

Mean Time Between Flushes	**Runs**	**Time per run (seconds)**	**Total runtime (seconds)**
5	18	18.28333333	329.1
5	19	18.53684211	352.2
5	19	18.37894737	349.2
5	16	19.40625	310.5
2	26	20.63076923	536.4
1	36	22.23333333	800.4
5	19	18.93157895	359.7
2	26	21.20769231	551.4
5	18	18.75	337.5
1	37	22.23243243	822.6
2	26	20.37692308	529.8
5	18	19.26666667	346.8
5	17	19.39411765	329.7
5	17	18.74117647	318.6
7	16	17.925	286.8
7	15	19.38	290.7
7	16	18.76875	300.3
5	18	19.06666667	343.2
5	18	17.78333333	320.1
7	15	19.5	292.5
5	17	19.05882353	324
5	18	18.76666667	337.8
2	26	20.81538462	541.2
5	17	18.9	321.3

Simulated Weekday Data for Leak Rate of 1.0 in./minute

Mean Time Between Flushes	**Runs**	**Time per run (seconds)**	**Total runtime (seconds)**
5	22	19.15909091	421.5
5	23	19.46086957	447.6
5	21	19.95714286	419.1
5	23	18.61304348	428.1
2	32	20.371875	651.9
1	42	21.95	921.9
5	22	19.2	422.4
2	29	20.87586207	605.4
5	23	18.88695652	434.4
1	42	22.00714286	924.3
2	32	20.08125	642.6
5	22	19.54090909	429.9
5	23	19.16086957	440.7
5	23	19.6173913	451.2
7	20	18.765	375.3
7	20	18.735	374.7
7	19	20.1	381.9
5	24	18.9875	455.7
5	22	19.77272727	435
7	20	19.59	391.8
5	22	19.30909091	424.8
5	22	19.59545455	431.1
2	32	19.903125	636.9
5	22	19.62272727	431.7

Simulated Weekday Data for Leak Rate of 1.5 in./minute

Mean Time Between Flushes	Runs	Time per run (seconds)	Total runtime (seconds)
5	26	20.27307692	527.1
5	27	20.1	542.7
5	27	19.67777778	531.3
5	26	20.50384615	533.1
2	35	20.76857143	726.9
1	45	23.27333333	1047.3
5	26	20.66538462	537.3
2	34	20.69117647	703.5
5	26	20.49230769	532.8
1	45	22.42666667	1009.2
2	36	21.2	763.2
5	27	20.48888889	553.2
5	26	20.86153846	542.4
5	26	19.91538462	517.8
7	25	19.62	490.5
7	25	19.188	479.7
7	25	19.644	491.1
5	26	20.43461538	531.3
5	26	20.43461538	531.3
7	25	19.728	493.2
5	25	20.772	519.3
5	26	20.79230769	540.6
2	35	20.72571429	725.4
5	27	20.61111111	556.5

Simulated Weekday Data for Leak Rate of 2.0 in./minute

Mean Time Between Flushes	Runs	Time per run (seconds)	Total runtime (seconds)
5	31	20.58387097	638.1
5	31	20.24516129	627.6
5	31	20.43870968	633.6
5	33	20.00909091	660.3
2	38	21.77368421	827.4
1	45	24.87333333	1119.3
5	31	20.53548387	636.6
2	39	22.12307692	862.8
5	31	20.55483871	637.2
1	46	24.28695652	1117.2
2	41	21.15365854	867.3
5	31	20.64193548	639.9
5	32	20.4375	654
5	31	20.48709677	635.1
7	29	20.37931034	591
7	29	20.07931034	582.3
7	30	19.87	596.1
5	32	20.596875	659.1
5	31	19.88709677	616.5
7	29	20.35862069	590.4
5	32	20.990625	671.7
5	31	19.82903226	614.7
2	38	22.29473684	847.2
5	31	20.79677419	644.7

Simulated Weekday Data for Leak Rate of 2.5 in./minute

Mean Time Between Flushes	**Runs**	**Time per run (seconds)**	**Total runtime (seconds)**
5	35	21.20571429	742.2
5	35	21.23142857	743.1
5	35	21.06	737.1
5	34	21.21176471	721.2
2	41	22.70487805	930.9
1	49	24.97346939	1223.7
5	33	21.61818182	713.4
2	42	22.60714286	949.5
5	35	21.30857143	745.8
1	47	25.85744681	1215.3
2	41	23.2902439	954.9
5	35	20.82	728.7
5	35	21.58285714	755.4
5	35	21.36	747.6
7	32	21.95625	702.6
7	32	21.35625	683.4
7	33	20.9	689.7
5	35	21.24	743.4
5	35	21.07714286	737.7
7	33	20.98181818	692.4
5	34	21.46764706	729.9
5	34	21.75882353	739.8
2	41	22.91707317	939.6
5	34	21.60882353	734.7

Simulated Weekend Data for Leak Rate of 0 in./minute

Mean Time Between Flushes	**Runs**	**Time per run (seconds)**	**Total runtime (seconds)**
10	8	20.0625	160.5
10	7	19.92857143	139.5
10	7	19.92857143	139.5
10	8	20.0625	160.5
10	7	19.92857143	139.5
10	8	20.0625	160.5
10	7	19.92857143	139.5
10	8	19.8375	158.7
10	7	19.92857143	139.5
11	6	20.1	120.6
11	7	19.92857143	139.5
11	7	19.92857143	139.5
13	6	20.1	120.6
13	6	20.1	120.6
13	5	19.86	99.3
13	5	19.86	99.3
13	6	20.1	120.6
13	6	20.1	120.6
10	8	20.0625	160.5
10	7	19.92857143	139.5
10	8	20.0625	160.5
10	7	19.92857143	139.5
10	6	20.1	120.6
10	7	19.92857143	139.5

Simulated Weekend Data for Leak Rate of 0.5 in./minute

Mean Time Between Flushes	**Runs**	**Time per run (seconds)**	**Total runtime (seconds)**
10	13	18.27692308	237.6
10	13	18.55384615	241.2
10	14	18.34285714	256.8
10	13	18.99230769	246.9
10	13	19.08461538	248.1
10	14	18.38571429	257.4
10	14	18.75	262.5
10	12	18.975	227.7
10	14	18.34285714	256.8
11	13	18.9	245.7
11	12	19	228
11	13	18.64615385	242.4
13	12	18.35	220.2
13	12	18.9	226.8
13	12	18.375	220.5
13	13	18.41538462	239.4
13	12	18.1	217.2
13	12	18.375	220.5
10	13	19.26923077	250.5
10	13	18.39230769	239.1
10	13	18.46153846	240
10	13	18.73846154	243.6
10	12	18.575	222.9
10	14	18.55714286	259.8

Simulated Weekend Data for Leak Rate of 1.0 in./minute

Mean Time Between Flushes	**Runs**	**Time per run (seconds)**	**Total runtime (seconds)**
10	19	18.61578947	353.7
10	18	18.65	335.7
10	18	18.93333333	340.8
10	18	19.65	353.7
10	18	18.68333333	336.3
10	18	19.31666667	347.7
10	18	18.9	340.2
10	18	18.93333333	340.8
10	18	18.95	341.1
11	17	19.27058824	327.6
11	17	18.77647059	319.2
11	18	18.98333333	341.7
13	18	18.71666667	336.9
13	17	18.98823529	322.8
13	16	19.33125	309.3
13	18	18.46666667	332.4
13	17	18.88235294	321
13	18	19.25	346.5
10	18	18.93333333	340.8
10	18	18.85	339.3
10	19	18.41052632	349.8
10	18	19.11666667	344.1
10	18	18.9	340.2
10	18	18.76666667	337.8

Simulated Weekend Data for Leak Rate of 1.5 in./minute

Mean Time Between Flushes	**Runs**	**Time per run (seconds)**	**Total runtime (seconds)**
10	23	19.33043478	444.6
10	23	19.27826087	443.4
10	22	20.1	442.2
10	23	19.77391304	454.8
10	23	19.56521739	450
10	23	19.06956522	438.6
10	23	19.39565217	446.1
10	23	19.04347826	438
10	22	19.99090909	439.8
11	23	19.21304348	441.9
11	23	19.09565217	439.2
11	23	19.27826087	443.4
13	22	19.62272727	431.7
13	21	19.2	403.2
13	21	19.74285714	414.6
13	21	19.34285714	406.2
13	22	18.83181818	414.3
13	22	19.2	422.4
10	22	20.07272727	441.6
10	23	19.72173913	453.6
10	23	19.47391304	447.9
10	22	19.74545455	434.4
10	24	18.6625	447.9
10	23	19.56521739	450

Simulated Weekend Data for Leak Rate of 2.0 in./minute

Mean Time Between Flushes	**Runs**	**Time per run (seconds)**	**Total runtime (seconds)**
10	27	20.15555556	544.2
10	27	19.8	534.6
10	27	19.97777778	539.4
10	27	20.02222222	540.6
10	28	19.85357143	555.9
10	28	19.71428571	552
10	28	19.97142857	559.2
10	26	20.97692308	545.4
10	26	20.08846154	522.3
11	26	20.58461538	535.2
11	27	19.96666667	539.1
11	27	20.11111111	543
13	26	20.66538462	537.3
13	26	19.95	518.7
13	26	19.83461538	515.7
13	27	20	540
13	26	19.76538462	513.9
13	27	18.96666667	512.1
10	27	19.88888889	537
10	27	20.54444444	554.7
10	27	20.14444444	543.9
10	27	20.1	542.7
10	26	20.22692308	525.9
10	27	20.4	550.8

Simulated Weekend Data for Leak Rate of 2.5 in./minute

Mean Time Between Flushes	**Runs**	**Time per run (seconds)**	**Total runtime (seconds)**
10	31	20.66129032	640.5
10	31	21.09677419	654
10	31	20.83548387	645.9
10	31	21	651
10	31	21.07741935	653.4
10	31	20.81612903	645.3
10	31	21.0483871	652.5
10	32	20.71875	663
10	31	20.39032258	632.1
11	31	20.50645161	635.7
11	31	20.24516129	627.6
11	31	20.49677419	635.4
13	31	20.27419355	628.5
13	30	20.98	629.4
13	30	20.61	618.3
13	31	20.63225806	639.6
13	30	20.81	624.3
13	30	20.52	615.6
10	31	20.79677419	644.7
10	32	20.04375	641.4
10	31	20.81612903	645.3
10	31	20.87419355	647.1
10	31	20.7	641.7
10	31	20.92258065	648.6

THIS PAGE INTENTIONALLY BLANK

Appendix E

Fluid System MATLAB Scripts

This appendix contains scripts used to simulate operation of a centrifugal pump. The first three scripts are used to calculate the currents, voltages and torque used by the motor. The next three scripts perform a MATLAB version of the "prep" software used for real current and voltage data to develop a power envelope for the simulated data. The final script puts all of the scripts together to run the simulation and plot the real power used by the electric motor vs. time. The scripts `indparam.m`, `ind.m`, and `convind.m` were written by Steven B. Leeb as part of [15]. The scripts `prep_fft.m`, `prep_rotate.m`, and `matlabprep.m` were written by Robert Cox, a fellow student at MIT's Laboratory for Electromagnetic and Electronic Systems (LEES). The script `indsim.m` was written by the author.

E.1 Indparam

```
%  This script loads the machine parameters for a 3hp, 180 V (L-N, peak) AC
%  induction machine into the global environment.
%  Run this code to load sample machine parameters before simulating with
%  ind.
%
%  This software is distributed in the hope that it will be useful, but
%  WITHOUT ANY WARRANTY.  It is for educational use only.  Please do not
%  distribute or sell this software, or remove the copyright notice.
%
%  Copyright, 1995, 1997, 1998, 2000  Steven B. Leeb
global P rs rr Xm X1s X1r we J Bl vds vqs vqr vdr Tl
% These are the machine parameters for a 3 Hp, 180V (L-N, peak) AC
% induction machine.
P = 4;          % Number of poles (*not* pole pairs)
rs = 0.435;     % Stator resistance
rr = 0.816;     % Rotor resistance
Xm = 26.13;     % Magnetizing Impedance, in Ohms on a 60 Hz base
X1s = 0.754;    % Stator Side Leakage Impedance, in Ohms on a 60 Hz base
X1r = 0.754;    % Rotor Side Leakage Impedance, in Ohms on a 60 Hz base
we = 377.;      % Base electrical frequency, rads per second (60 Hz)
J = 0.089;      % Rotor Inertia
```

```
Bl = 0;        % Load Damping Coefficient
vds = 0.0;     % D axis stator voltage
vqs = 180.0;   % Q axis stator voltage
vqr = 0.0;     % D axis rotor voltage
vdr = 0.0;     % Q axis rotor voltage
Tl = 0.0;      % Load torque
```

E.2 Ind

```
function [slopes] = ind(t,statev)
%  [slopes] = ind(t,statev)
%
%  This script computes the state variable derivatives for a fifth
%  order model of a balanced, three phase AC induction machine.
%  The state variables are the D and Q stator and rotor fluxes, and
%  the rotor speed (wr).
%  Use this script with ODE45 to simulate the performance of the
%  induction machine.
%
%  Run indparam.m to load sample machine parameters before simulating.
%
%  This software is distributed in the hope that it will be useful, but
%  WITHOUT ANY WARRANTY.  It is for educational use only.  Please do not
%  distribute or sell this software, or remove the copyright notice.
%
%  Copyright, 1995, 1998, 2002  Steven B. Leeb
%  The variable w determines the reference frame in which the simulation
%  will be conducted.  With w = 377, the simulation variables will be in
%  a synchronously rotating reference frame.
global P rs rr Xm X1s X1r we J Bl vds vqs vqr vdr Tl
w = 377.;
Lm  = Xm/we;  % This is the magnetizing inductance
L1s = X1s/we; % Stator leakage
L1r = X1r/we; % Rotor leakage
Las = L1s + Lm;
Lar = L1r + Lm;

lamqs = statev(1);
lamds = statev(2);
lamqr = statev(3);
lamdr = statev(4);
wr    = statev(5);
%th    = statev(6);

D = Lm*Lm - Las*Lar;
idr   = (Lm*lamds - Las*lamdr)/D;
iqr   = (Lm*lamqs - Las*lamqr)/D;
```

```
iqs   = (Lm*lamqr - Lar*lamqs)/D;
ids   = (Lm*lamdr - Lar*lamds)/D;

s1 = (vqs - w*lamds - rs*iqs);
s2 = (vds + w*lamqs - rs*ids);
s3 = (vqr - (w - wr)*lamdr - rr*iqr);
s4 = (vdr + (w - wr)*lamqr - rr*idr);
% P is the number of poles, *not* pole pairs
T  = (3/2)*(P/2)*(lamqr*idr - lamdr*iqr);
s5 = (P/2)*(T-0.0002614*wr^2)/(J + 0.00401);
%s6 = 377;
slopes = [s1 s2 s3 s4 s5]';% s6]';
```

E.3 Convind

```
function [m,m2] = convind(t,y);
%  [m,m2] = convind(t,statev)
%
%  This script transforms the DQ stator and rotor fluxes computed using
%  ind.m and ode45 back into laboratory frame stator currents and voltages,
%  e.g., ias and vas for phase a.
%
%  The variable w determines the reference frame in which the simulation
%  will be conducted.  With w = 377, the simulation variables will be in
%  a synchronously rotating reference frame.
%
%  On return, the output matrices m and m2 contain:
%  m = [ids iqs idr iqr];
%  m2 = [T ias ibs ics vas vbs vcs];
%  This script also plots the simulated rotor torque versus speed on return.
%
%  This software is distributed in the hope that it will be useful, but
%  WITHOUT ANY WARRANTY.  It is for educational use only.  Please do not
%  distribute or sell this software, or remove the copyright notice.
%
%  Copyright, 1995, 1998, 2002  Steven B. Leeb
global P rs rr Xm X1s X1r we J Bl vds vqs vqr vdr Tl
% select reference frame (see ind.m)
 w = 377.;

 Lm  = Xm/we;  % This is the magnetizing inductance
 L1s = X1s/we; % Stator leakage
 L1r = X1r/we; % Rotor leakage
 Las = L1s + Lm;
 Lar = L1r + Lm;

 lamqs = y(:,1);
```

```
lamds = y(:,2);
lamqr = y(:,3);
lamdr = y(:,4);
wr    = y(:,5);
th    = w*t; %y(:,6);

D = Lm*Lm - Las*Lar;
idr   = (Lm*lamds - Las*lamdr)/D;
iqr   = (Lm*lamqs - Las*lamqr)/D;
iqs   = (Lm*lamqr - Lar*lamqs)/D;
ids   = (Lm*lamdr - Lar*lamds)/D;

T     = (3/2)*(P/2)*(lamqr.*idr - lamdr.*iqr);

ias = cos(th).*ids - sin(th).*iqs;
ibs = cos(th - 2.*pi/3.).*ids - sin(th - 2.*pi/3.).*iqs;
ics = cos(th + 2.*pi/3.).*ids - sin(th + 2.*pi/3.).*iqs;
vas = cos(th).*vds - sin(th).*vqs;
vbs = cos(th - 2.*pi/3.).*vds - sin(th - 2.*pi/3.).*vqs;
vcs = cos(th + 2.*pi/3.).*vds - sin(th + 2.*pi/3.).*vqs;


m = [ids iqs idr iqr];
m2 = [T ias ibs ics vas vbs vcs];
```

E.4 Prep_FFT

```
% This file will run an offline version of prep on data that has already been sampled
% to have 128 pts/period
% A is current data
% B is voltage data

function [vHarm, iHarm] = prep_fft(A, B, rows)

i = 1;
j = 1;
nBasis = 128;
shift = 64;
harm = [1 3 5 7]; % The harmonics we want to look at
nHarm = 4;
in = zeros(1,nBasis);
out = zeros(1,nBasis);
iHarm = zeros(1,rows*nHarm*2);
vHarm = zeros(1,rows*2);

for i=1:1:rows
   for j=1:1:nBasis
```

```
      in(j) = B(j + (i - 1) * shift); % load up the vector to be FFTd
   end

   out = fft(in, nBasis);
   vHarm(i*2-1) = real(out(2));
   vHarm(i*2) = imag(out(2));
   for j=1:1:nBasis
      in(j) = A(j+(i-1)*shift);
   end

   out = fft(in,nBasis);
   for j=1:1:nHarm
      iHarm((i-1)*2*nHarm+((j*2)-1)) = real(out(harm(j)+1));
      iHarm((i-1)*2*nHarm + 2*j) = imag(out(harm(j)+1));
   end
end
```

E.5 Prep_Rotate

```
function E =prep_rotate(vHarm,iHarm,rows)

pqbar = zeros(1,2);
pqtmp = zeros(1,2);

i=1;
j=1;
nrot=1;
nHarm = 4;
harm = [1 3 5 7];
E = zeros(rows,2*nHarm);

for i=1:1:rows;
   pqbar(1) = vHarm(i*2 - 1);
   pqbar(2) = vHarm(i*2);
   mag = sqrt(pqbar(1) * pqbar(1) + pqbar(2) * pqbar(2));

   if (mag ~= 0)
      pqbar(1) = pqbar(1)/mag;
      pqbar(2) = pqbar(2)/mag;
   end

   nrot = 1;
   pqtmp(1) = pqbar(1);
   pqtmp(2) = pqbar(2);


for j=1:1:nHarm
```

```
      a = iHarm((i-1)*2*nHarm+((j*2)-1));
      b = iHarm((i-1)*2*nHarm + 2*j);

      pqtmp = prep_multiply(pqtmp, pqbar, nrot, harm(j));

      E(i,(2*j)-1) = a*pqtmp(1) + b*pqtmp(2);
      E(i,2*j) = -(b*pqtmp(1) - a*pqtmp(2));
   end
end
```

E.6 Matlabprep

```
% E = matlabprep(A,B,rows)
%
% Given current and voltage sampled with 128 points per period, matlabprep will
% output arbitrarily scaled spectral envelopes.
%
% A is the vector of current values
% B is the vector of voltage values
% rows is the number of cycles of the 60Hz waveform
%
% This function, and all of the functions which it invokes, are
% based on routines found in softprep.c by Steve Shaw.
%
% Robert Cox, 2003

function E=matlabprep(A,B,rows)

[vHarm,iHarm]=prep_fft(A,B,rows);
E=prep_rotate(vHarm,iHarm,rows);
```

E.7 Indsim

```
indparam;
t=0:1/(128*60):8;
[t,y]=ode45(@ind,t,[0 0 0 0 0]);
wr=y(:,5);
[m,m2]=convind(t,y);
Ias=m2(:,2);
%Vas=m2(:,5);
Vcb=m2(:,7)-m2(:,6);
rows=480;
time=(1:481)/60;
E=ones(481,8);
E(1,:)=0;
E(2:481,:)=matlabprep(Ias,Vcb,rows);
```

```
P=E(:,2);
plot(time,P)
```